METAL OXIDE THIN FILMS BY CHEMICAL VAPOR DEPOSITION FOR PHOTOCATALYTIC WATER SPLITTING

by

ARCHANA SATHYASEELAN PANIKAR

ARUNAVA GUPTA, COMMITTEE CHAIR

SHANLIN PAN
GREGORY J. SZULCZEWSKI
MARTIN G. BAKKER
DAWEN LI

A DISSERTATION

Submitted in partial fulfillment of the requirements
for the degree of Doctor of Philosophy
in the Department of Chemistry
in the Graduate School of
The University of Alabama

TUSCALOOSA, ALABAMA

2016

ABSTRACT

Photoelectrochemical cells (PEC) are devices which convert solar energy into consumable chemical energy by splitting water into oxygen and hydrogen. Photocatalytic activity at a semiconductor oxide surface forms the backbone of the PEC and thus the quest for high activity oxide materials and improving the cells efficiency is a widely explored field of research. Metal oxide semiconductors with band gaps in the visible spectrum are actively sought as photocatalytic electrode materials. The major advantages are that oxides are nontoxic, stable, and inexpensive. However, their overall efficiency is usually limited by short carrier diffusion length due to structural defects, limited light absorptivity and sluggish kinetics at the interface. To overcome these limitations crystalline semiconductor oxides synthesized by high temperature techniques are desired. A direct liquid injection chemical vapor deposition technique has been employed to synthesize films of Fe_2O_3 (hematite) and $BiVO_4$ (bismuth vanadate) for use as photocatalysts. The high temperature synthesis technique is optimized to obtain good quality crystalline smooth films on fluorine doped tin oxide substrates and their photoelectrochemical characteristics have been studied. It is observed that the interlayer oxide material used for growth of the Fe_2O_3 and $BiVO_4$ has a significant role in their photoactivity.The interlayer oxide serves as an efficient electron transport layer and also influences the grain characteristics of the film. For hematite it is observed that a n-type metal oxide interlayer (e.g. Nb_2O_5 or TiO_2) helps improve the photoactivity as compared to a p-type oxide (NiO). $BiVO_4$ has a poor electron diffusion length, and a WO_3 interlayer improves the photocurrent in $BiVO_4$ films by improving the charge collection efficiency.

The low absorption coefficient of hematite requires a dense electrode for greater light absorption; however, the electrode thickness is limited by the poor hole diffusion length (~4 nm). Plasmonic metal nanostructures of gold (Au), silver (Ag), and copper (Cu), which are known to concentrate and scatter broad range wavelengths of incident light, are promising for enhancing the light absorption cross-section of a semiconducting material. Gold nanoparticles embedded in hematite films have been synthesized. About three times higher light absorption and photocurrent enhancement are obtained. A thickness-dependent study of photoactivity indicates a greater enhancement of gold-embedded hematite thin films compared to thicker films due to reduced charge transport distance and optimal local field enhancement effect. The embedded structure also has the advantage of consistent performance and protection of plasmonic nanostructures from electrochemical corrosion, resulting in long cycles of operation.

DEDICATION

Dedicated to my family, advisors, friends and the almighty God. Their love, guidance and support helped me get through the difficult times in graduate school.

LIST OF ABBREVIATIONS AND SYMBOLS

LUMO	Lowest unoccupied molecular orbital
HOMO	Highest occupied molecular orbital
PEC	Photoelectrochemical cell
WE	Working electrode
CE	Counter electrode
RE	Reference electrode
NHE	Normal hydrogen electrode
OER	Oxygen evolution reaction
HER	Hydrogen Evolution reaction
VB	Valence band
CB	Conduction band
DLI	Direct liquid injection
CVD	Chemical vapor deposition
SEM	Scanning electron microscopy
TEM	Transmission electron microscopy
XRD	X-ray diffraction
UV-Vis	Ultraviolet-Visible
APCVD	Atmospheric pressure CVD
LPCVD	Low pressure CVD

MOCVD	Metal-organic CVD
PECVD	Plasma enhanced CVD
PHCVD	Photo enhanced CVD
LCVD	Laser induced CVD
MFC	Mass flow controller
CV	Cyclic voltammetry
CL	Condenser lens
OL	Objective lens
IPCE	Incident photon conversion efficiency
AC	Alternating current
DFT	Density functional theory
RHE	Reversible hydrogen electrode
PVP	Polyvinylpyrrolidone
FTO	Florine doped tin oxide
ITO	Indium doped tin oxide
AM	Air mass
Co-Pi	Cobalt phosphate oxygen evolution catalyst
DMF	Dimethyl formamide
NP	Nanoparticle
SPR	Surface plasmon resonance
LSPR	Localized surface plasmon resonance
BVO	Bismuth vanadate
YSZ	Yttria stabilized zirconia

EDS	Energy dispersive spectroscopy
TW h	Terra Watt hour
m	Meters
kW	Kilo Watt
J	Joules
e^-	Electrons
h^+	Holes
μm	Micrometer
MJ	Mega Joules
g	Grams
kg	Kilograms
cc	Cubic centimeters
ΔG	Free energy
atm	Atmospheric pressure
kJ	Kilo Joules
F	Farads
ΔE^o	Standard water oxidation potential
nm	Nanometers
^oC	Degree Celcius
n	Number of electrons
C	Coulombs
V	Potential or Voltage
I	Current

mol	Number of moles
eV	Electron-volt
s	s-orbital
p	p-orbital
d	d-orbital
f	f-orbital
mM	Milli molar
M	Molar
kV	Kilo volt
nm	Nanometer
Pa	Pascal
d	Lattice spacing
n	Order of diffraction
θ	Incident angle
A	Absorption
ε	Absorption coefficient
c	Concentration
L	Path length
psi	Pounds per square inch
g/h	Grams per hour
mV	Millivolt
mV/s	Millivolt per second
mA	Milli ampere

mm	Millimeter
Å	Angstrom
λ	Wavelength
$J_{(\lambda)}$	Current density at a given wavelength
$P_{(\lambda)}$	Power of the incident light radiation
mW/cm^2	Milli Watt per square centimeter
Hz	Hertz
R_{CT}	Charge transfer resistance
R_S	Series resistance
R_T	Trap state resistance
C_{SC}	Charge capacitance
C_{trap}	Trap state capacitance
R_{CT}	Charge transfer resistance
η	Quantum efficiency
W	Depletion width
α	Absorption coefficient
L_K	Recombination distance
k	Recombination rate
k_ε	Faradaic rate constant
v_0	Degree of band bending
sccm	Standard cubic centimeters per minute
Z”	Imaginary component of impedance
f	Frequency

C	capacitance
q	Elementary charge
ε_0	Permittivity of free space
k	Boltzmann constant
ε	Dielectric constant
V_{fb}	Flat band potential
C_{SC}	Space charge capacitance
k_t	Rate constant for charge transfer
k_r	Rate constant for charge recombination
P_{inc}	Incident power
A	Area of the film
T	Temperature
at wt	Atomic weight
%	Percentage

ACKNOWLEDGEMENTS

Heartfelt gratitude to my advisor Prof. Arunava Gupta for believing in me and accepting me as a student under his supervision. His guidance helped me to think critically and work independently towards problems. Special thanks to Dr. Shanlin Pan for the discussions throughout my Ph.D. study and allowing me to use the facilities in his laboratory. I would also like to thank my dissertation committee members Dr. Gregory J. Szulczweski, Dr. Martin G. Bakker and Dr. Dawen Li for their time and important feedback on my research. I am grateful to my previous research advisors Prof. Jose Rajan (now at Universiti Malaysia, Pahang) and Prof. Seeram Ramakrishna at National University of Singapore for getting me started as a researcher and motivating me to pursue a Ph.D. in the U.S.A.

Next, I would like to acknowledge the funding sources throughout my study: Department of Chemistry for teaching assistantship (2011-2012, 2015) NSF for funding our research (2012-2015) and the Graduate school (2015-2016) for providing me with a Graduate Council Fellowship.

I am grateful to David Key and the other technicians from machine shop for the help with troubleshooting and customizing lab instruments. Their knowledge and eagerness have helped us improve our instruments over the years. Thanks to Billy and Danny from the electronics shop for all the help with the electrical components.

I would like to thank Johnny Goodwin, Rob Holler and Rich Martens from Central Analytical Facility for training me on SEM, XRD and TEM instruments.

It would not be possible to continue my study without the cheerful and conducive atmosphere at Shelby Hall and MINT Center created by my current and previous labmates Dr. Karthik Ramasamy, Dr. Ziyou Zhou, Nariman Nahibolashrafi, Dr. Gunwoo Kim, Mehmat Kenan and Dr. Matthias Althammer. Summer 2013 was fun, thanks to summer students Benjamin Tien and Krystal Flantroy. Special thanks to Dr. Neha Pachauri and Amit V. Singh who are not only labmates but my best friends for their support throughout. Thanks to all the current and former members from Dr. Pan's group: Daniel Clayton, Caleb Hill, Jue Wang, Zhichao Shan and Nelly Kaneza for all the fruitful collaborations.

Thanks to Sefadzi, Canisius, Juliette, Garima, Trupti and Vaishali for being good friends, attending practice sessions and countless other things. Thank you Binoy and Naveen for helping and cheering me up through bad times.

I would like to thank my parents and my brother for their immense support and prayers. I would like to acknowledge all who could not be mentioned here, but have always had a positive influence in my life. Finally, thank you God for everything.

CONTENTS

LIST OF TABLES

LIST OF FIGURES

CHAPTER 1

INTRODUCTION

1.1 Current Energy Scenario and the Role of Clean Energy

Energy is a basic necessity for the sustenance of mankind; and its demand multiplies with a growing population and urbanization. The increase in fossil fuel consumption has caused emission of greenhouse gases such as CO_2, SO_2, NO_2, thereby polluting the atmosphere and leading to rising temperatures. With depleting fossil energy sources and the need of a clean environment for future generations, the quest for clean energy alternatives has been intensified in recent times.

1.2 Renewable Energy

Renewable energy is defined as energy that is collected from resources which are naturally replenished. The main sources of renewable energy are sunlight, wind, rain, tides and waves and geothermal heat. Figure 1.1 shows the sources of global power 22,668 TW h consumed in the year 2012, the contribution of renewable energy sources is only 5%.[1]

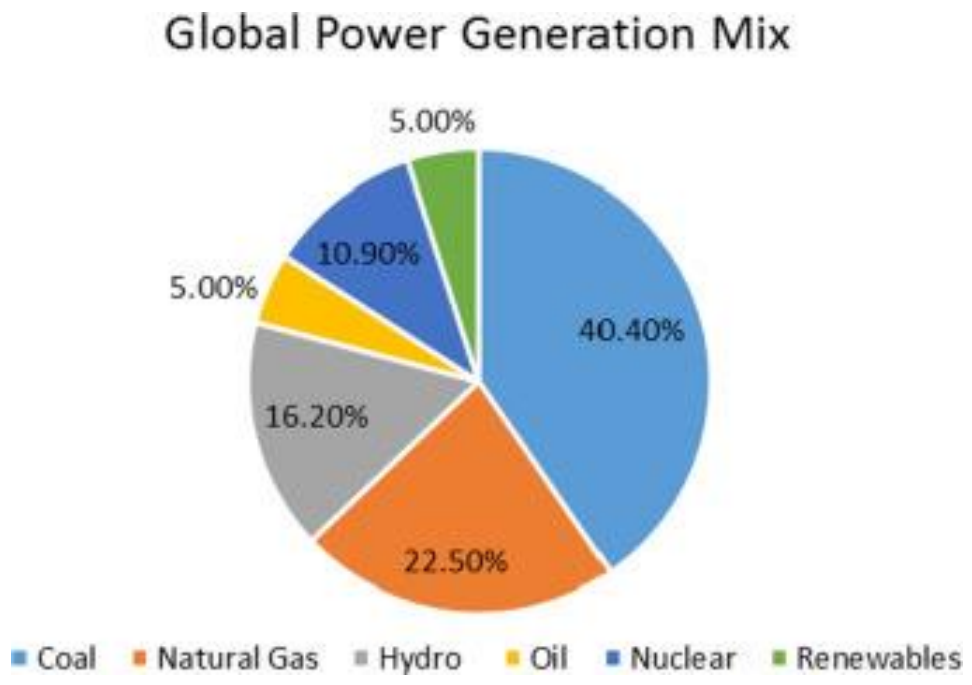

Figure 1.1: Distribution of global power consumed in year 2012. (Pie graph adopted from Ref 1. Copyright 2015 Elsevier Ltd.)

The hurdles in attaining an energy system based completely on renewable sources are plenty. The first hurdle being the present availability of fossil fuel resources. World reserves of natural gas are about 1.4×10^{14} m^3 and the gross production of gas is about 2.4×10^{12} m^3 per year.[2] Thus fossil fuels will remain a dominant energy source for near future. Such an abundance of fossil fuel resources and the lowering of prices over the past few years put a hold on the urgency of development of clean energy sources.

Next challenge in the large scale utilization of renewable energy technology is the storage and transport issues involved. For example, the energy of light emitted from the Sun depends on the time of day and weather conditions. Efficient storage systems must be developed to store the energy harvested for later usage. Unfortunately there is no battery technology available today that has the energy density of gasoline, and battery recharging is far slower than filling a gasoline tank.[2]

Moreover, the lifetime of batteries needs to be improved, and much lighter and non-toxic battery materials must be found. The biggest challenge so far is the low conversion efficiencies and high cost of technologies such as photovoltaics and photoelectrochemical cells. Highest solar cell efficiency obtained on the laboratory scale are as high as 46.0% [3] but when made into solar panels and grids for practical applications, the efficiency obtained is just 10-15%.[3] The cost of current silicon (Si)-based solar electricity modules is \$300 m^{-2} resulting in a cost of \$3 per Watt, which is equivalent to an electricity price of \$0.35 per kW h.[4] In comparison, fossil-derived electricity costs approximately \$0.02 - 0.05 per kW h, including storage and distribution costs.[4] To reach a cost point comparable to that of fossil-derived energy will thus require improvements in efficiency and a large decrease in cost into a range below \$100 m^{-2}.[4] Thus materials with low cost but high efficiency are to be developed in order to attain the goal of realizing a future with major contribution from clean energy.

1.3 Overview of Solar Energy Technologies

The amount of solar energy (4.3×10^{20} J) striking the Earth's surface per hour is approximately equal to the total energy consumed (4.1×10^{20} J) on the planet in a year.[5] Covering 0.1% of the Earth's surface with 10-15% efficiency solar panels would be able to meet the energy demands.[6] Developing moderately efficient but cheap methods of harvesting this tremendous source of energy would be able to solve the clean energy crisis problems. Keeping this in mind, different types of solar cell devices are being developed. On the basis of working principle, they can be classified as follows:

(i) p-n junction solar cells

Silicon solar cells are an important example of p-n junction solar cells. When p and n doped silicon crystals are brought in close contact, the diffusion of ions occurs across the boundary form

a p-n junction. Incident light creates free electrons and holes which are accelerated towards the collection electrodes by a built in potential at the p-n junction. This electric field created by the built in potential, drives the carrier separation.[7] Single crystal silicon solar cells have achieved close to ~24% conversion efficiency without concentrators and have long term stability.[8] However it requires expensive and energy intensive high temperature and high vacuum processes.

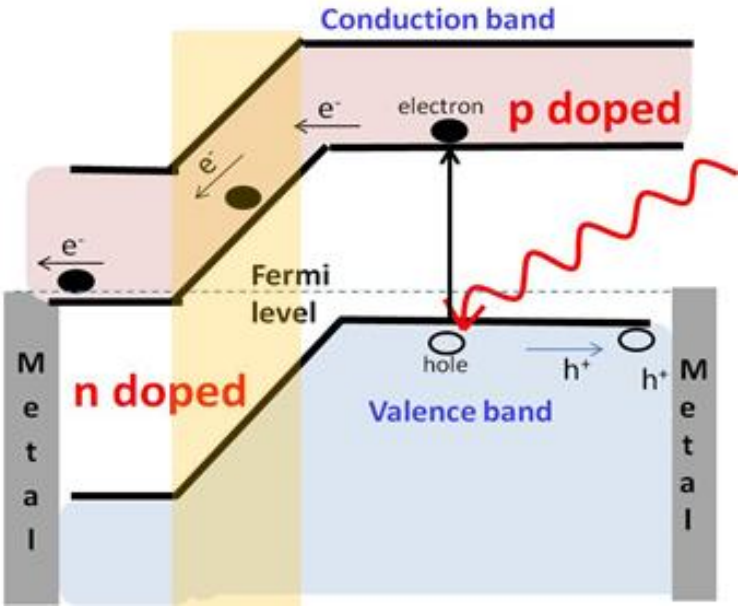

Figure 1.2: Working principle of a p-n junction solar cell

(ii) Excitonic solar cells:

In an excitonic solar cell, light absorption creates a transiently generated localized excited state known as an exciton. The separation of the exciton into mobile carriers occurs when the absorber is coupled with a material whose conduction band or Lowest Unoccupied Molecular Orbital (LUMO) is at lower energy. Figure 1.3 shows a general schematic of an excitonic solar cell. It consists of a donor- acceptor pair of species. The donor molecules absorbs light to generate e^- -h^+ pairs (excitons) that diffuse to the interface and separate to form free electrons holes. The electrons are then transported through the acceptor via drift diffusion and holes transported through

the acceptor molecules.[9] Depending on the type of the donor and acceptors, there are several types of excitonic solar cells and each one varies accordingly in the device structure. In a dye/quantum sensitized solar cell, dye/ quantum dots adsorbed on a thin layer of TiO_2 acts as donor, TiO_2 acts as an electron transporting medium and a liquid I_3/I^- electrolyte acts as the hole transporting medium. In an organic solar cell, a blend of p and n type polymers act as donor acceptors. Excitonic solar cells are lower in efficiency and less stable as compared to the silicon solar cells. However they are made from materials highly abundant in nature and at a lower cost.

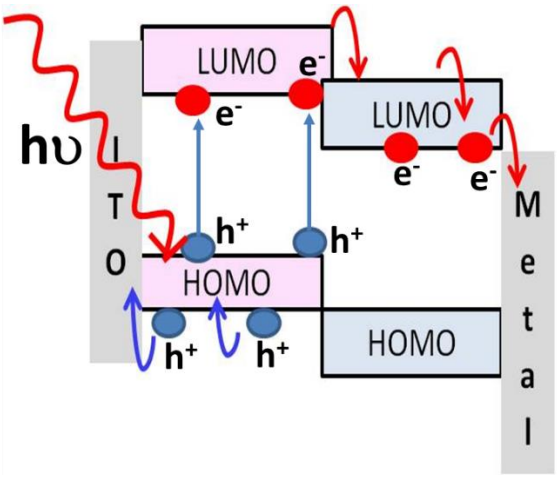

Figure 1.3: Schematic of an excitonic solar cell

A new class of solar cells based on organometallic halides ($CH_3NH_3PbX_3$, where X= Cl, Br, I) known as perovskites solar cells has attracted attention in recent years after Snaith et.al reported devices with efficiency of 10.9%.[10] It consists of a TiO_2 layer coated by a thin layer of perovskite and an organic p type polymer as an acceptor. Perovskites are known to have electron and hole diffusion lengths of the order of ~1 μm because of loosely bound excitons and also known to have high charge accumulation.[11] Due to these properties perovskites have been used as excitonic sensitizers as well as in p-n junction configuration. Perovskite solar cells with an efficiency of 21%[3] on lab scale and 10.4% on a PV module of 10 cm^2 have been reported.[12]

1.4 Hydrogen economy

An alternate method to harvest solar energy is via photolysis of water to generate oxygen and hydrogen which could be used as fuel. Such a sustainable energy system based on solar energy and water is known as hydrogen economy.[13] If successfully realized, it is the most sustainable and clean method of energy generation as the fuel generated is by means of sunlight and water. The combustion of hydrogen generates water as the only by product which does not have any environmental harmful effects. Hydrogen is the third most abundant element on our planet and has a specific energy (energy stored per kilogram of reactants) of 120 MJ/kg compared to gasoline which is 45 MJ/ kg and that of a Li ion battery which is 0.3-0.8 MJ/ kg. Hydrogen releases 142 MJ/kg on combustion and produces the least pollution when ignited in air. Automobiles currently running on natural gas can be readily run on hydrogen.[14] Some of the disadvantages are the low density of liquid hydrogen (0.07g/cc) compared to that of gasoline (0.75g/cc), which makes the handling and storage large and bulky. Liquid hydrogen has a temperature of 20 K necessitating the use of super insulated storage vessels.[14]

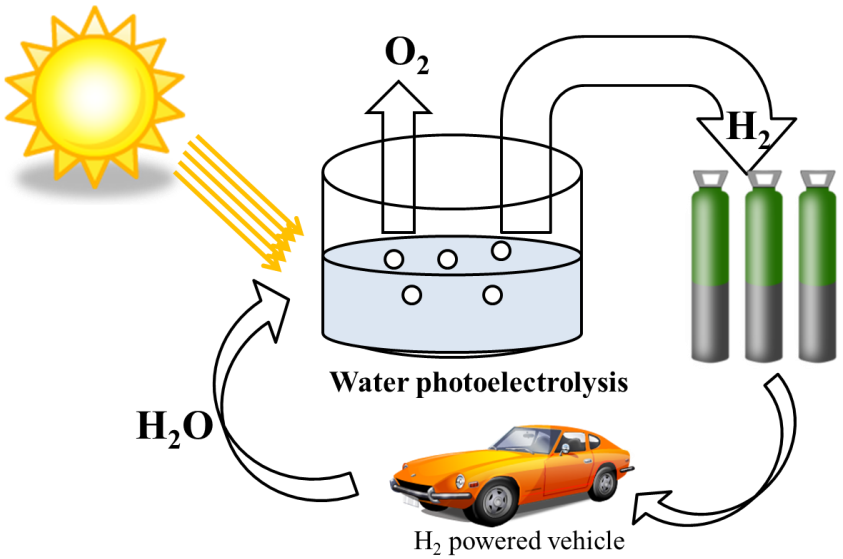

Figure 1.4: Hydrogen economy: A proposed sustainable energy system based on hydrogen

Photolysis of water is a process similar to photosynthesis, which is nature's way to synthesize carbohydrate ($C_6H_{12}O_6$) from CO_2 and H_2O. The overall reaction is carried out through a series of redox reactions with the aid of appropriate rate accelerating electrolcatalysts in the presence of sunlight. A photoelectrolysis cell can be considered to be an artificial photosynthetic device used to split water to form hydrogen and oxygen via robust, simple and earth abundant materials. The photoelectrolysis cell forms the heart of hydrogen economy system.

1.5 Photoelectrochemical cells

A photoelectrochemical cell (PEC) is defined as a device which can convert light energy into consumable energy through light induced electrochemical processes.[14] In a PEC current and voltage are simultaneously produced upon absorption of solar light by one or more electrodes. The output is either electrical or chemical energy. Figure 1.5 shows the schematic representation of an ideal PEC to generate hydrogen by water photoelectrolysis. The PEC consists of three electrodes, a working electrode (WE), counter electrode (CE) and reference electrodes (RE). Commonly a n-type semiconductor forms the anode that on light illumination evolves oxygen. The cathode consists of a metal electrode where hydrogen is evolved. The incident light on the working electrode (photoanode) initiates water oxidation reaction to generate oxygen. The electrons are transferred to the cathode to carry out the water reduction reaction. The phenomenon of water splitting on semiconducting TiO_2 surface on irradiation of light was first observed by Fujishima and Honda in 1972[15] and forms the backbone of a photoelectrolysis cell. Since then considerable amount of research has been devoted to explore an efficient, stable and cheap semiconductor to support water splitting.

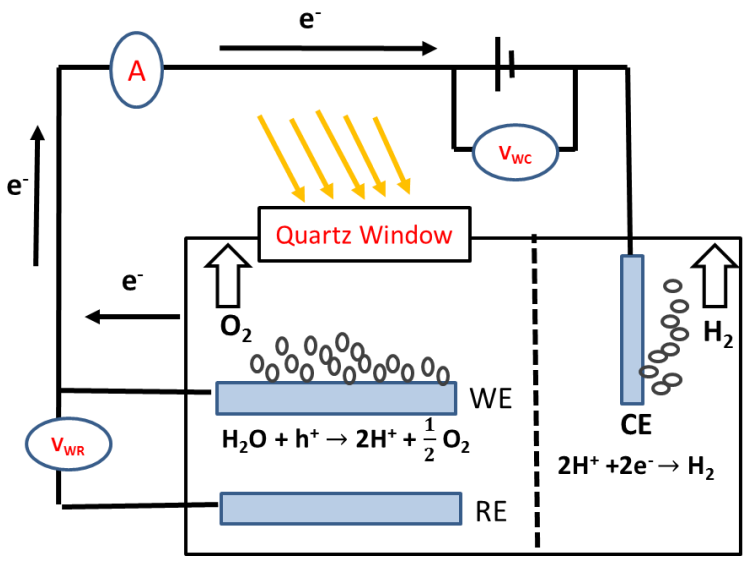

Figure 1.5: Schematic diagram of a photoelectrolysis cell.

1.6 Principle of water splitting on semiconductor

The free energy (ΔG) released when a water molecule is decomposed to its constituent atoms is 237.2 kJ/mol under standard conditions.[16] Converting this free energy to potential by the Nernst formula $\Delta G = nF\Delta E^o$ where n= number of electrons=2 and 1F=96500 C/V, ΔE^o (water oxidation potential at standard state of 25 ^oC, 1 atm =1.23 eV) (Equation 1)

$H_2O \rightarrow 2H^+ + \frac{1}{2}O_2$…….. ΔG= 237.2 kJ/mol or ΔE^o =1.23 eV. … (1)

This energy also corresponds to a photon with wavelength 1000 nm or lower. Thus the water splitting reaction can be easily performed in presence of sunlight which primarily consists of visible radiation (330- 760 nm) photons. A semiconductor with a band gap ≥ 1.23 eV can act as a light harvesting site for the water splitting reaction.

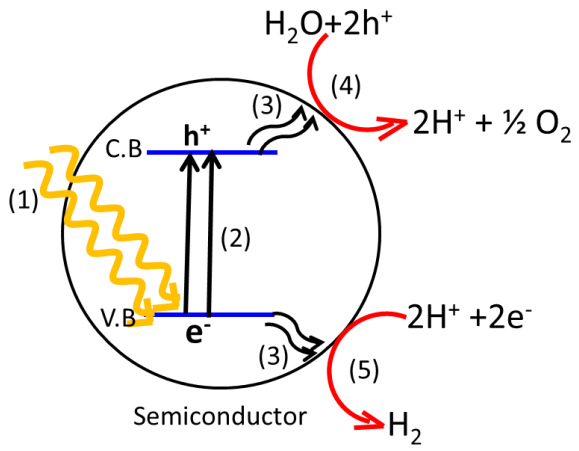

Figure 1.6: Schematic describing steps involved in semiconductor catalyzed water splitting reaction.

Consider a semiconductor with a band gap of 1.23 eV or higher. Following are the steps involved in the water splitting process.[17]

1. Light of suitable wavelength is absorbed at the semiconductor surface.
2. Absorbed photons generate electron hole (e^--h^+) pairs.
3. The electron hole (e^--h^+) pairs diffuse to surface of the semiconductor and are separated to generate free carriers electrons and holes.
4. The electrons and holes react with electrolyte species to carry out water oxidation and reduction reactions, respectively.

The following half reactions take place at the semiconductor surface

$$2H_2O + 4h^+ \rightarrow 4H^+ + O_2 \quad \ldots 2.46 \text{ V vs. NHE... Oxygen Evolution Reaction (OER)} \ldots (2)$$

$$4H^+ + 4e^- \rightarrow 2H_2 \ldots 0.0 \text{ V vs. NHE} \ldots \text{Hydrogen Evolution Reaction (HER)} \ldots (3)$$

The water splitting process involves four electron or hole transfer across the semiconductor interface. The overall process is limited by several factors. Firstly, the absorption cross section and

absorptivity of the semiconductor determines the number of photons being absorbed by the material. A major portion of solar spectrum consists of visible light photons with maximum intensity centered in the green region (~550 nm), hence a semiconductor with visible light activity is preferred.[18] The valence band and conduction band of the semiconductor have to be suitably aligned in order for the surface reactions to be feasible. The valence band potential should be slightly positive as compared to the water oxidation potential of 1.23 V Vs. NHE and conduction band position should be slightly negative in comparison to the water reduction potential of 0.0 V Vs. NHE.[15] Valence and conduction band positions of popular semiconductors marked are shown in figure 1.7. Second, the light generated carriers should be transferred to surface before they are recombined. A material with minimal surface defects to promotes the charge transfer process. Third, the semiconductor should be stable and does not undergo corrosion on generation of charge carriers. Finally the charge transfer from the surface of semiconductor should be efficient to carry out OER and HER processes.

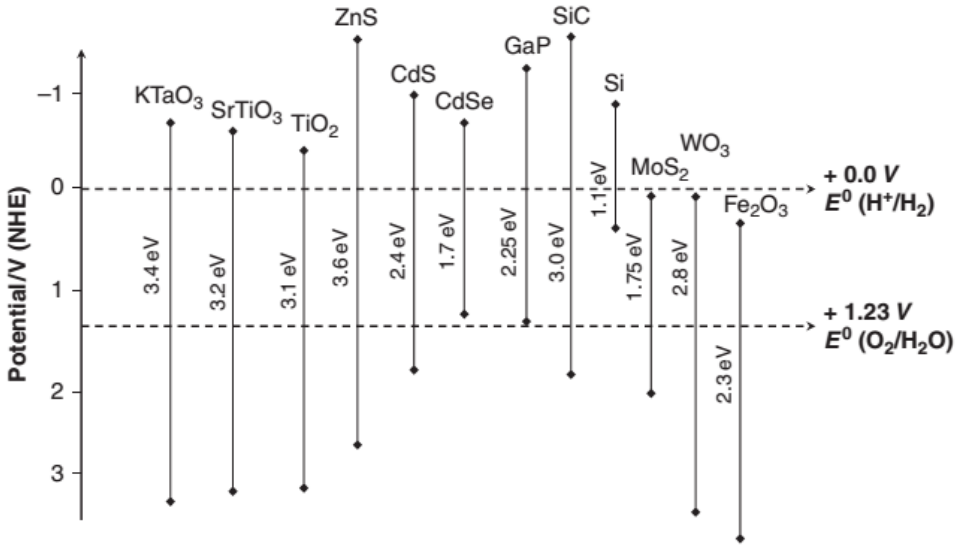

Figure 1.7: Band edge positions of some semiconductors marked w.r.t water oxidation and reduction potentials on a potential scale vs. Normal Hydrogen electrode (NHE). (Reproduced from Ref.16, copyright 2009 Elsevier)

Depending on the valence band (V.B) and conduction band (C.B) positions of the semiconductor, it is possible to favor either oxidation or reduction reactions. For example Fe_2O_3 has a band gap of 2.3 eV with a C.B position at 0.7 eV and V.B position at 3.0 eV. Since the V.B. position is highly positive compared to that of water oxidation potential of 1.23 eV, the OER is feasible on Fe_2O_3 surface. Such oxides act as photoanode in a photoelectrochemical cell. Similarly CdSe favors the water reduction reaction as its conduction band is much negative compared to water reduction potential and thus such materials form photocathode materials. Figure 1.7 shows the V.B and C.B positions of different materials with respect to water oxidation and reduction potentials.[19]

1.7 Materials for photocatalytic water splitting

A vast range of materials can support the water splitting half reactions. These can be broadly classified as oxides, sulfides, oxysulfides, nitrides or oxynitrides,

(i) Oxides

(a) Binary metal oxides

Oxides form the most abundant materials on earth. These are efficient and stable to support the photocatalysis. Some examples of well know n type oxides with their band gap values listed in parenthesis are listed TiO_2 (3.2 eV), Fe_2O_3 (2.2 eV), WO_3 (2.8 eV). Drawbacks of these metal oxide semiconductors include low absorptivity, poor charge carrier transport and high overpotential losses.[20]

(b) Ternary metal oxides

These include the derivatives of the binary oxides like TiO_2, Nb_2O_5 and Ta_2O_3 to form titanates, niobates and tantalates. Some examples of such mixed oxides are $SrTiO_3$ (3.2 eV),

$LaTi_2O_7$ (3.8 eV), $Sr_2Nb_2O_7$ (3.9 eV) and $KTaO_3$ (3.2 eV). These derived oxides have a layered perovskite structure that eases the migration and separation of the photogenerated carriers. The overall efficiency is however limited by the large band gaps which can absorb only in the U.V region of the solar spectrum. Some other transition ternary metal oxides with high efficiency include $BiVO_4$ (2.4 eV), $BiNbO_4$ (2.80 eV) and Ag_3VO_4 (2.38 eV).[20]

(c) Sulfides and Oxysulfides

Sulfides are an impressive class of compounds due to their low band gaps and visible light activity but are limited by their low stability in electrolytes due to higher tendency of oxidation of S^{2-} ions compared to that of water. However the use of S^{2-} sacrificial reagents help to combat the corrosion to some extent. Eg: CdS (2.4 eV), ZnS (3.6 eV), $AgInS_2$ (1.80 eV) and $Sm_2Ti_2S_2O_5$ (2 eV).[16]

(d) Nitrides and oxynitrides

Nitrides and oxynitrides represent a stable class of compounds for water splitting applications without sacrificial reagents. An example is the mixture of ZnO and GaN. Both ZnO and GaN have band gaps higher than 3.0 eV and therefore do not absorb in the visible region of solar spectrum. A solid solution of $(Ga_{1-x}Zn_x)(N_{1-x}O_x)$ has absorption edges in the visible region with band gaps of 2.4-2.8 eV.[21] Similar characteristics are observed in the solid solutions of $ZnGeN_2$ and ZnO. The composite $(Zn_{1+x}Ge)(N_2O_x)$ has a band gap of 2.7 eV.[17]

1.8 Strategies for improving photocatalytic activity of materials

Although the efficiency limiting processes of the water splitting phenomenon have been well identified, it is still a challenging task to find materials that satisfy all of the requirements. The major efficiency limiting barrier is the loss of the generated charge carriers by recombination, as a result the number of carriers that reach the surface for the redox reactions at the surface is

limited. A number of strategies have been reported so far to increase the overall conversion efficiency of the surface reactions, as listed below.

(i) Band gap engineering

As most of the Sun's radiation is in the visible range, an ideal photocatalyst would be one with an absorption in the visible region. Many of metal oxide semiconductors such as TiO_2, $SrTiO_3$, ZnO, etc. (figure 1.7) do not follow this condition and their band gap have to be tuned to obtain maximum activity. This can be done by engineering the band gap by (a) doping or (b) use of semiconductor alloys.

(ii) Doping of semiconductors

Doping is a commonly used method to modify the band edges of a semiconductor. The valence band edge of semiconductor oxides such as TiO_2, Fe_2O_3 etc. consists of O *2p* atomic orbitals. Anion doping by N, S or C species causes mixing of dopant p states with the O *2p* causing an upward shift in the valence band edge. As compared to cation doping, anion replacement usually results in fewer recombination centers hence more effective for enhancing photocatalytic activity. However, the number of oxygen defects in the anion doped materials due to the difference in oxidation state of dopant ions can act as recombination centers. Examples of anion doping include N, C doped TiO_2.[16]

Cation doping in semiconductors can be defined as the replacement of cations in semiconductor lattice by dopant cations. The replacement of cations may create impurity energy levels within the band gap of the photocatalyst that facilitates absorption of visible light. Additionally a cation dopant may also cause a shift in the conduction band edge of the semiconductors. A dopant ion in the semiconductor matrix can induce visible light activity with an absorption coefficient dependent on the density of dopant ions but the dopant center can also

be disadvantageous by acting as recombination sites for photogenerated electrons and holes. It can also introduce trap states in the band gap of the semiconductor which reduces the lifetime of the generated carriers. Thus there is a tradeoff between the dopant ion concentration for the visible light activity of semiconductors and them acting as recombination centers. Some examples of cation doping include Ni^{2+}, Cr^{3+}, W^{6+} etc. doped TiO_2. The doped semiconductors can be prepared by addition of a calculated amount of dopant ion precursor during synthesis of the semiconductor. Advanced ion-implantation techniques which use high energy ions accelerated by high voltage of 50-200 keV is another method for doping of cations in bulk semiconductors.[16]

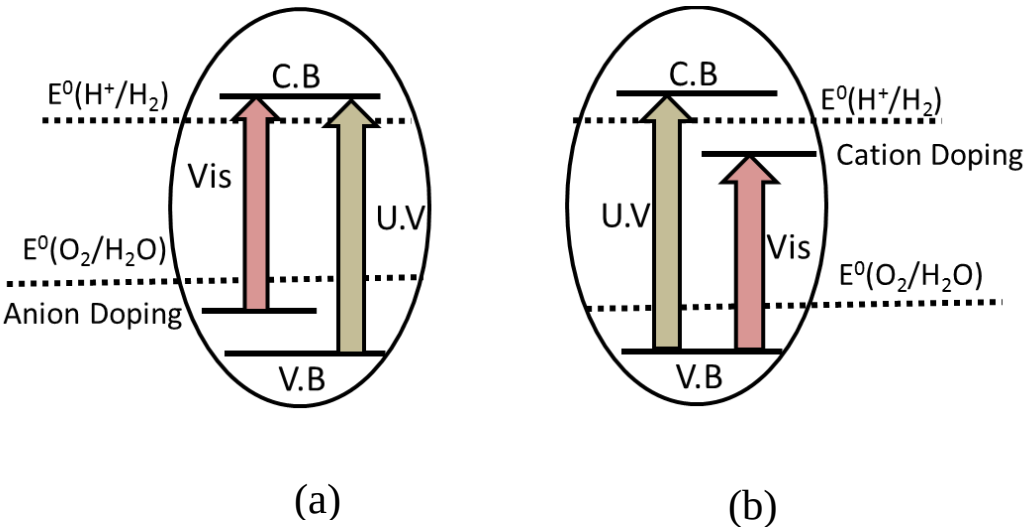

Figure 1.8: Band gap engineering by doping in semiconductors (a) Anion doping: generates an upward shift in the valance band edge. (b) Cation doping: creates lowering of conduction band.

(iii) Surface co-catalysts

The next step after the generation of carriers involves the transfer of generated carriers to ions in solution to carry out oxidation or reduction reaction. The kinetics for the charge transfer processes are sluggish and limits the overall efficiency of the catalyst. The rate of surface reactions

can be increased by employing co-catalysts such as Pt, NiO, Co-Pi, RuO_2 on the semiconductor surface. The co-catalyst improves the efficiency of semiconductor photocatalysts by (i) capturing the conduction band electrons or valence band holes from photocatalysts thereby reducing the possibility of electron-hole recombination and (ii) reducing the activation energy of water oxidation/reduction by transferring the electrons and holes to surface water molecule.[16]

(iv) Sensitization

One of the ways to populate the conduction band of wide gap semiconductors with electrons under visible light excitation is by sensitization using efficient light absorbers such as dyes, quantum dots, plasmonic nanoparticles etc. Sensitization of TiO_2 by ruthenium based dyes have been studied widely for application in dye sensitized solar cells, however the process is yet to be optimized for efficient use in water splitting cells. Sensitization by plasmonic nanoparticles on semiconductors is known to increase the photocatalytic activity of the semiconductors by a number of different mechanisms and will be discussed in subsequent chapters.

Coupling of a wide band gap semiconductor with a narrow band gap semiconductor to form composites is an effective way for sensitization. The strategy is based on utilizing suitably aligned band edges of the semiconductors in order to promote inter-particle charge injection and hence efficient charge separation. For successful coupling of the semiconductors, the following conditions are to be met (i) the conduction band and valence band of wide band gap semiconductor should be higher as compared to the low band gap semiconductor (ii) the valence band of wide band gap semiconductor should be more positive as compared to the water oxidation potential and (iii) the conduction band of narrow band semiconductor should be more negative compared to the water reduction potential. Such coupling ensures separation of water oxidation and reduction half reactions hence making charge separation more efficient (figure 1.9).

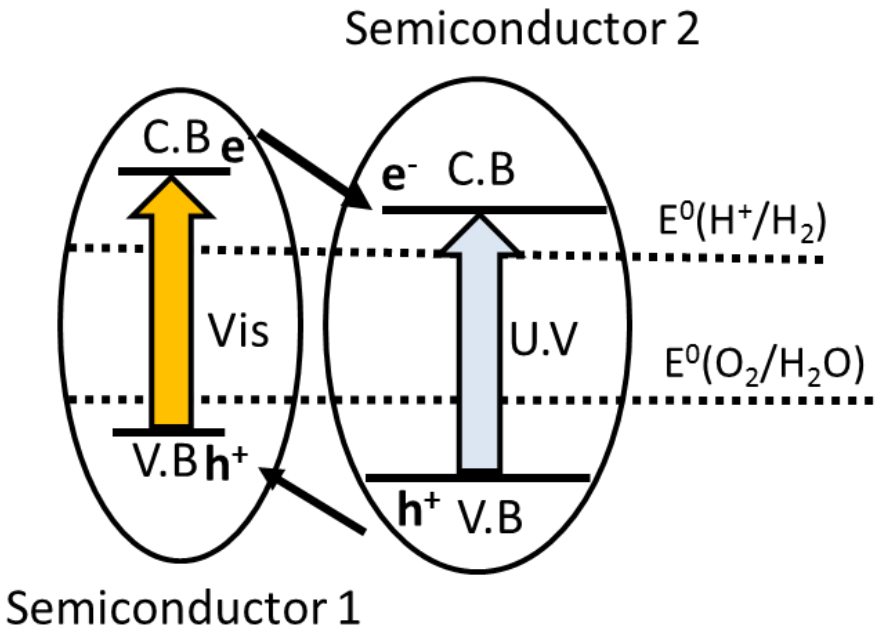

Figure 1.9: Inorganic semiconductor sensitization

(v) Morphology of the catalysts

As explained in the principle of water splitting on the semiconductor surface, the semiconductor generate holes and electrons have to travel to the surface to carry out the water oxidation and reduction steps. Thus following properties are to be considered (i) crystallinity of the material: the charge transport in the semiconductor should be efficient which is determined by the crystallite size, crystal structure and the nature of the crystal defects in the material. A high degree of crystallinity in materials means lower density of defects which ensures better charge transport of carriers. Structural defects may act as recombination centers by trapping the carriers. (ii) Surface area of the material: a higher surface area increases the number of reaction sites on the material. Taking into account the effect of surface area and crystallinity of material on the

photoactivity, high surface area crystalline nanomaterials with are preferred. Different synthesis methods such as hydrothermal, sonochemical, electrochemical anodization have been used to generate different morphology nanomaterials. Drawbacks associated with nanomaterials include agglomeration and lowering crystallinity and increasing surface defects as size decreases. To avoid this incorporation of photocatalysts on mesoporous and microporous substrates have been successful.[16]

1.9 Scope of Dissertation

Attempts to address the drawbacks in the existing metal oxide semiconductor electrodes are studied in detail in the current work. Two different metal oxide systems hematite (α-Fe_2O_3) and clinobisvanite ($BiVO_4$) have been synthesized by a direct liquid injection chemical vapor deposition technique. The high temperature synthesis technique is optimized to obtain good quality crystalline smooth films on fluorine doped tin oxide substrates. A compact thin film structure is chosen over a mesoporous structure as the former has fewer grain boundaries which provides an efficient pathway for electron transport through the material. Figure 1.10 shows the schematic of the electron transport in a mesoporous vs. compact oxide film.

Figure 1.10: Carrier transport in (a) mesoporous film and (b) Compact thin film.

The direct liquid injection chemical vapor deposition (DLI-CVD) technique yields high quality single phase metal oxide films with fewer grain boundaries. Unlike other synthesis techniques, the

photoactvity of the films is not compromised as the thickness of the films increased as the high temperature direct growth method yield crystalline films with long range order.

In order to improve the electron transport of the hematite film, different metal oxide interlayers are employed for charge collection and it is observed that the performance depends on the nature of the metal oxide interlayer used. An n type metal oxide interlayer (e.g. ZnO, TiO_2) serves as better electron transport layers as compared to p type oxide (e.g. NiO). Plasmonic metal nanostructures of Au, Ag, and Cu are known to concentrate and scatter broad range wavelengths of incident light and hold the promise on enhancing the light absorption cross-section of a semiconducting material. The photoelectrochemical characteristics of a smooth hematite photocatalytic layer embedded with Au nanoparticles are studied. Thickness dependent plasmonic activity studies indicate that a maximum enhancement in 110 nm hematite films as compared 630 nm hematite films where the plasmonic activity of Au NPs is least shielded.

A detailed account of the studies on DLI-CVD grown hematite and $BiVO_4$ is provided in the following chapters.

1.10 References

(1) Ahmed, S.; Mahmood, A.; Hasan, A.; Sidhu, G. A. S.; Butt, M. F. U. A Comparative Review of China, India and Pakistan Renewable Energy Sectors and Sharing Opportunities. *Renewable and Sustainable Energy Reviews* **2016**, *57*, 216-225.

(2) Dresselhaus, M. S.; Thomas, I. L. Alternative Energy Technologies. *Nature* **2001**, *414*, 332-337.

(3) National Renewable Energy Laboratory *http://www.nrel.gov/ncpv/images/efficiency_chart.jpg* (accessed 02/08, 2016).

(4) Lewis, S. N.; Nocera, D. G. Powering the Planet: Chemical Challenges in Solar Energy Utilization. *PNAS* **2007**, *104*, 15729-15735.

(5) Jose, R.; Thavasi, V.; Ramakrishna, S. Metal Oxides for Dye-Sensitized Solar Cells. *J Am Ceram Soc* **2009**, *92*, 289-301.

(6) Gratzel, M. Photovoltaic and Photoelectrochemical Conversion of Solar Energy. *Phil. Trans. R. Soc. A* **2007**, *365*, 993.

(7) Saga, T. Advances in Crystalline Silicon Solar Cell Technology for Industrial Mass Production. *NPG Asia Mater.* **2010**, *2*, 96-102.

(8) DeWolf, S.; Descoeudres, A.; Holman, Z. C.; Ballif, C. High-Efficiency Silicon Heterojunction Solar Cells: A Review. *Green* **2012**, *2*, 7-24.

(9) Gregg, B. A. Excitonic Solar Cells. *J Phys Chem B* **2003**, *107*, 4688-4698.

(10) Lee, M. M.; Teuscher, J.; Miyasaka, T.; Murakami, T. N.; Snaith, H. J. Efficient Hybrid Solar Cells Based on Meso-Superstructured Organometal Halide Perovskites. *Science* **2012**, *338*, 643-647.

(11) Park, N. Perovskite Solar Cells: An Emerging Photovoltaic Technology. *Materials Today* **2015**, *18*, 65-72.

(12) Razza, S.; Di Giacomo, F.; Matteocci, F.; Cinà, L.; Palma, A. L.; Casaluci, S.; Cameron, P.; D'Epifanio, A.; Licoccia, S.; Reale, A.; Brown, T. M.; Di Carlo, A. Perovskite Solar Cells and Large Area Modules (100 cm^2) Based on an Air Flow-Assisted PbI_2 Blade Coating Deposition Process. *J. Power Sources* **2015**, *277*, 286-291.

(13) Hou, H. J. M. In *Water Splitting with Sunlight Inspired by Photosynthesis;* Trends in Environmental Science; 2014; pp 53-70.

(14) Grimes, C. A.; Varghese, O. K.; Ranjan, S., Eds.; In *Light, Water, Hydrogen;* Springer: 2008; Vol. 1, pp 546.

(15) Fujishima, A.; Honda, K. Electrochemical Photolysis of Water at a Semiconductor Electrode. *Nature* **1972**, *238*, 37-38.

(16) Navarro, R. M.; del Valle, F.; Villoria de la Mano, J. A.; Álvarez-Galván, M. C.; Fierro, J. L. G. Photocatalytic Water Splitting Under Visible Light: Concept and Catalysts Development. *Advances in Chemical Engineering* **2009**, *36*, 111-143.

(17) Navarro Yerga, R. M.; Alvarez-Galván, M. C.; Vaquero, F.; Arenales, J.; Fierro, J. L. G. In *Hydrogen Production from Water Splitting Using Photo-Semiconductor Catalysts;* Renewable Hydrogen Technologies: Production, Purification, Storage, Applications and Safety; 2013; pp 43-61.

(18) Takanabe, K. Solar Water Splitting using Semiconductor Photocatalyst Powders. *Top. Curr. Chem.* **2015**, *371*, 73-104.

(19) Abe, R. Recent Progress on Photocatalytic and Photoelectrochemical Water Splitting Under Visible Light Irradiation. *Journal of Photochemistry and Photobiology C: Photochemistry Reviews* **2010**, *11*, 179-209.

(20) Moniruddin, M.; Kudaibergenov, S.; Nuraje, N. Chapter 7: Hierarchical Nanoheterostructures for Water Splitting. *RSC Green Chem.* **2016**, *2016-January*, 142-167.

(21) Yoshida, M.; Hirai, T.; Maeda, K.; Saito, N.; Kubota, J.; Kobayashi, H.; Inoue, Y.; Domen, K. Photoluminescence Spectroscopic and Computational Investigation of the Origin of the Visible Light Response of $(Ga_{1-x}Zn_x)(N_{1-x}O_x)$ Photocatalyst for overall Water Splitting. *J. Phys. Chem. C* **2010**, *114*, 15510-15515.

CHAPTER 2

EXPERIMENTAL METHODS

2.1 Introduction

This chapter gives a brief description of the working principles of the experimental techniques used to synthesize, characterize and study the photoelectrochemistry of materials used. The chapter is divided into three parts (1) material synthesis techniques, (2) material characterization techniques: provides a brief overview of the working principles of characterization techniques such as scanning electron microscopy (SEM), transmission electron microscopy (TEM), UV-Visible spectroscopy, and (3) photoelectrochemical characterization: describes the specific methods used to characterize the synthesized oxides for photocatalytic water splitting.

2.2 Material synthesis techniques

2.2.1 Chemical Vapor Deposition

Chemical vapor deposition is a class of *in situ* deposition technique where the constituents of the vapor phase react chemically near or on a substrate surface to form a solid product. The CVD technique is one of the most important methods for creating thin films and coatings of a very large variety of materials essential to advanced technology like solid-state electronics. A good example is the deposition of single crystal silicon layers by hydrogen reduction of dichlorosilane vapors for semiconductor devices.[1] It is a versatile technique where a precise control of phase,

composition and film thickness can be attained. The chemical reaction types include pyrolysis (thermal decomposition), oxidation, reduction, hydrolysis, nitride and carbide formation. A combination of several reaction types are also involved in more complex situations to obtain a particular end- product. The deposition variables such as temperature, pressure, input concentrations, gas flow rates, reactor geometry and operating principle determine the deposition rate and the properties of the film deposit. Depending on the procedure for deposition, there are different type of CVD techniques. They are listed as follows:

(i) Atmospheric pressure CVD technique (APCVD)

As the name suggests, the CVD is carried out under atmospheric pressure. The substrates are placed in a heated chamber, the precursor gases when introduced in the chamber react on the substrate to form the desired film. The advantages include low operation cost due to lack of vacuum system and the disadvantages include low control of uniformity and low control of gas flow at high temperatures.[1]

(ii) Low pressure CVD technique (LPCVD)

LPCVD is similar to APCVD but operate in a low pressure of (0.1 to 10 mTorr). As opposed to APCVD provides a better control of deposition.[1]

(iii) Metal-organic CVD (MOCVD)

This type of CVD involves a metalorganic precursor in gas form for growing epitaxial films, particularly of compound semiconductors. Based on the different activation methods these can be further classified as plasma enhanced CVD (PECVD) , plasma created by AC or DC power source to create reactive ions), photo-enhanced CVD (PHCVD, short-wave ultraviolet radiation is used to activate precursor); laser-induced CVD (LCVD, activate gaseous reactant atoms or

molecules by absorption of the specific wavelength of the photonic energy supplied). In case of a liquid precursor being used, a vaporizer is used to evaporate the liquid and create vaporizer precursors and is known as direct liquid injection CVD (DLI –CVD).[2]

A home- assembled direct liquid injection CVD system was used to deposit semiconductor oxide thin films in the current study.[3] A schematic of the system is as shown below (figure 2.1):

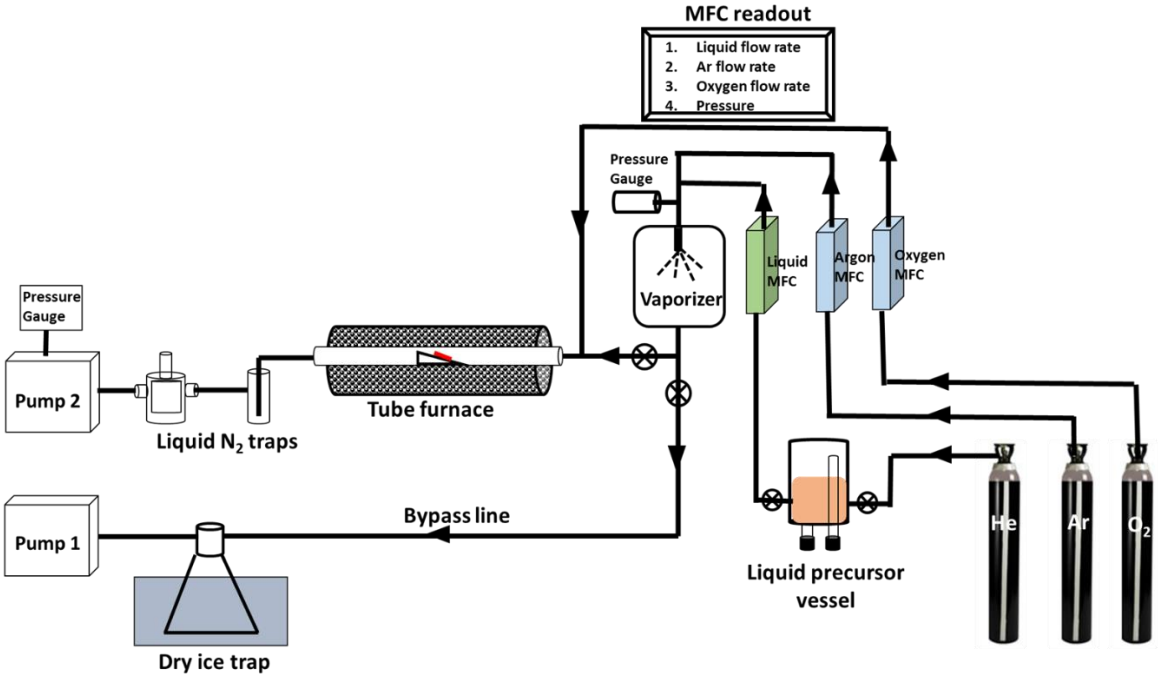

Figure 2.1 Schematic of the DLI-CVD system.

The CVD system consists of the following parts: (a) quartz tube in a tube furnace (b) vacuum pumps (c) liquid precursor bubbler (d) liquid and gas mass flow controllers (MFC), (e) vaporizer, and (f) digital read out for MFCs. A step- by- step process for deposition of thin films is outlined as follows: The substrates are loaded into the quartz tube and the vacuum pump is turned on to obtain a vacuum of 0.005 psi. The tube furnace is heated to the desired deposition temperature. The vaporizer is heated up at vaporization temperature of the solvent used to prepare the precursor

solution. The precursor solution with suitable concentration in the desired solvent is prepared and introduced in the bubbler vessel. A helium flow attached to the vessel drives the precursor solution to the liquid MFC, which maintains the liquid flow at a desired flow rate (1-9g/h). The liquid is introduced in the heated vaporizer to generate vapors. Argon gas flow is used as a carrier gas to carry the vapors from the vaporizer to the furnace. An external supply of oxygen is introduced in the furnace for the decomposed precursor to be oxidized on the substrate. Both argon and oxygen flow rates are maintained by mass flow controllers. Liquid nitrogen traps attached to the quartz tube are cooled to capture residual vapors from the reactor. After the desired deposition time the valve to the furnace is closed and the bypass line is opened up to clean the vaporizer and liquid MFC of residual precursor with pure solvent.

2.2.2 Spin coating

Spin coating is a chemical solution deposition technique used to deposit films on a flat substrate. It is a versatile technique and can be used to deposit films with thickness varying from nanometer (nm) to micrometer (μm) range. The process of spin coating involves maintaining a flat substrate on a sample stage under vacuum. The precursor solution of the material to be deposited is then dropped on the substrate. The substrate can be already rotating or starts to rotate after the solution is dropped.[4] The equipment used for spin coating is known as a spin coater. Modern day spin coaters are programmable for multiple step rotations and time settings. The three important steps involved in the preparation of films by spin coating are as follows:

(i) Preparation of precursor solution: The deposition solution must contain precursors completely dissolved in the solvent. A solvent which wets the substrate and are more volatile than the precursors must be chosen. Alcohols such as ethanol and propanol are preferred solvents. Acetic acid is also used where in the precursor ions are to be stabilized by coordination bonds.

Precursor are chosen such that the dry intermediate layer contains only the necessary species for the formation of the final film. Metallorganic precursors such as metal alkoxides, metal acetates and metal acetylacetonoates are preferred due to their stability and solubility in organic solvents.[5]

(ii) Spin coating conditions: Typical rotation speeds are about 1,000 to 10,000 rpm depending on the viscosity of the solution and final desired thickness. The rotation times depends on the volatility of the solvent and condensation rate of precursor ions on the substrate.

(iii) Post treatment of spin coated films: The final step involved in obtaining the film is the post annealing at suitable temperature to obtain the right phase of target material.

2.2.3. Electrodeposition of metal nanoparticles

Electrodeposition is a deposition technique on a conductive substrate by reducing dissolved metal ions in an electrolyte solution using electric current. The experimental set up for the electrodeposition is shown below in figure 2.2. It consists of a reference electrode (RE), counter electrode (CE), and working electrode (WE) on which the metal has to be deposited. The electrodes are immersed in a solution containing metal salts and are connected to a potentiostat for application of a potential. In most cases the WE is the cathode (negative) electrode. The reduction of metal ions occurs when a potential is applied across the electrodes. The potential to be applied depends on a number of factors such as the reduction potential of the ions in solution, conductivity of the WE and the distance between WE and CE. A reference electrode provides a stable, reproducible voltage to the working electrode.

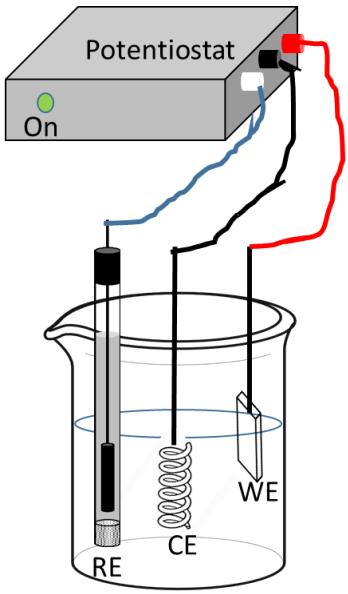

Figure 2.2 Schematic of a three electrode cell for electrodeposition of metals.

The electrodeposition process proceeds in two steps, the first step involves the generation of nanoparticle seeds followed by growth of these seeds due to reduction of ions on the seed surface. A dilute metal ion solution (<1 mM) with a supplementary electrolyte (0.1M NaCl, 0.1M KOH, etc.) to increase the conductivity of the solution is used to obtain nanoparticles as a concentrated solution generates large size seeds followed by its growth to rapidly form metal films.[6, 7] Cyclic voltammetry (CV) is an effective method to electrodeposit metal nanoparticles on a substrate. A CV is performed by cycling the potential of a WE and measuring the resulting current. Peaks in a CV indicate oxidation (positive current) and reduction events (negative current) on the WE. Thus the CV can be used to determine the reduction potential of the metal ions on the working electrode surface. When used for metal ion deposition, the first few cycles create metal nanoparticle seeds on the electrode surface. In subsequent cycles, the growth of seeds occur to increase their size. The voltage scan rate in CV is a key factor that determines the size of the metal seeds and the growth rate of seeds on the WE. Figure 2.3 shows the CV of a TiO_2 nanotube surface in a 0.1 mM $HAuCl_4$

solution in 0.1 M NaCl at a scan rate of 50 mV/s. The reduction of Au^{3+} occurs at -0.7 V vs Ag/AgCl reference electrode. The SEM images (figure 2.4) shows the increase in number of Au nanoparticle seeds and growth with increasing number of CV cycles.

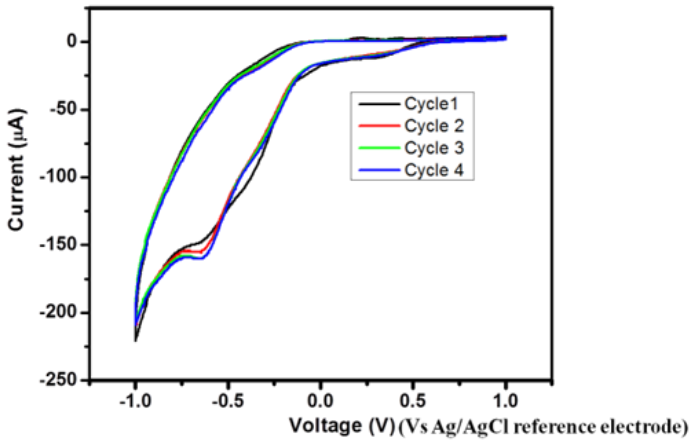

Figure 2.3 CV of a TiO_2 nanotube surface in a 0.1 mM $HAuCl_4$ solution in 0.1 M NaCl at a scan rate of 50 mV/s.

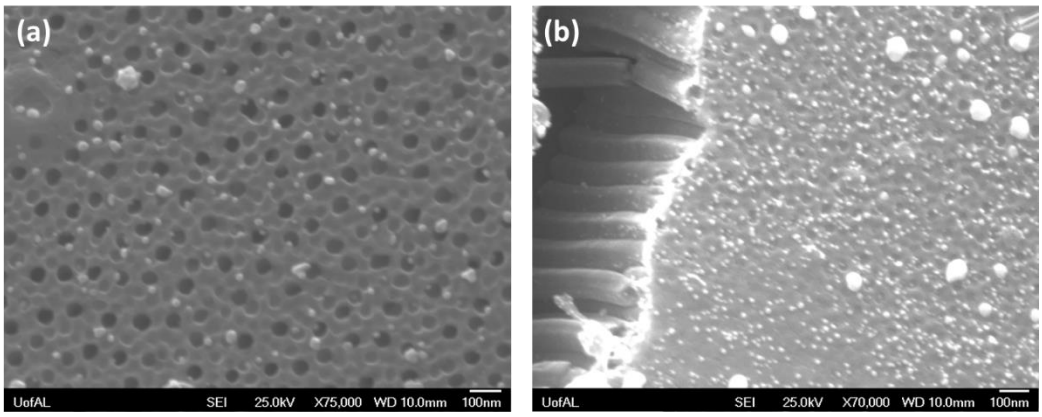

Figure 2.4. SEM images of Au nanoparticle deposited TiO_2 nanotubes for different CV cycles (a) 2 cycles and (b) 4 cycles

2.3 Material characterization techniques

2.3.1 Scanning electron microscopy (SEM)

Scanning electron microscopy is a technique used to image surface of samples with the help of focused electron beam. When an electron beam with a high accelerating voltage (10-30 kV) is incident on a sample they are elastically or inelastically scattered from the surface of the sample as seen in figure 2.5. The kinetic energy of the inelastically scattered electrons is lower than the incident beam. Such electrons are known as secondary electrons and contain the topographical information about the sample surface. The direct collision of incident beam with the atomic nuclei in the sample generates electrons with kinetic energy comparable to the incident beam and are known as back scattered electrons. The kinetic energy of back scattered electrons is proportional to the atomic weight of the elements in the sample and are used for chemical mapping.[8]

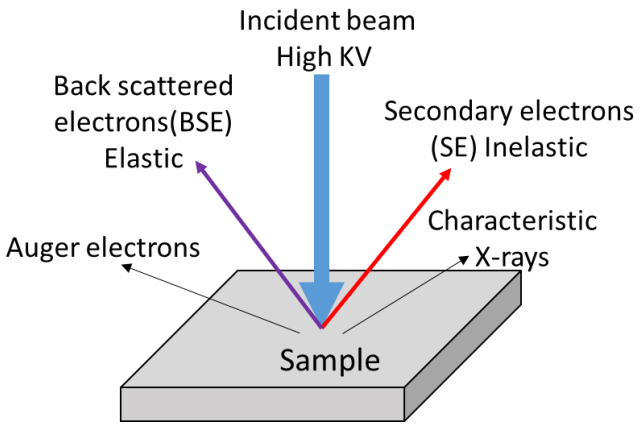

Figure 2.5 Electron bean interactions when a high energy beam is incident on a sample.

In addition to the scattering phenomenon, X-rays and Auger electrons are created due to the excitation and relaxation of electrons in the atoms of the sample. The energy of the X-rays gives the information of the chemical composition of the sample. A schematic of the instrumental

setup of a scanning electron microscope is shown in figure 2.6. The instrument consists of an electron source, a series of electromagnetic lenses to and detectors to detect the secondary, and backscattered electrons and X-rays.

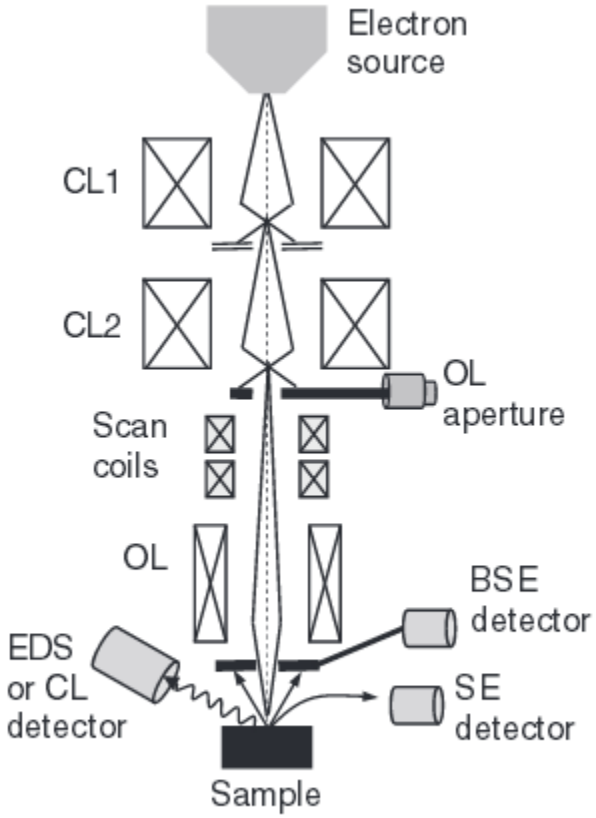

Figure 2.6 Schematic of instrumentation of a scanning electron microscope (figure adopted from Ref. 9, Copyright 2013, John Wiley and Sons)

The electron beam is generated either by thermionic emission or field emission from a tungsten filament. The electron beam that has an accelerating voltage of 0.4 to 40 kV is condensed to a spot size of 0.4 to 5 nm by a first and second condenser lenses. The scanning coils helps to deflect the electron beam in the ‘x’ and ‘y’ axes so it scans in a raster fashion over a rectangular area of the sample surface. A final objective lens is used to tune the deflected beam to obtain a

focused image. Since the energy of the back scattered electrons is similar to the incident electrons, the back scattered detector, which is in the form a ring is located just below the objective lens. A secondary electron detector and X-ray detector (also known as energy dispersive spectrometer (EDS)) are located close to the sample.[8] The instrument is maintained under vacuum of ~ 10^{-4} Pa. An example of SEM imaging and EDS spectrum are shown in figure 2.7.

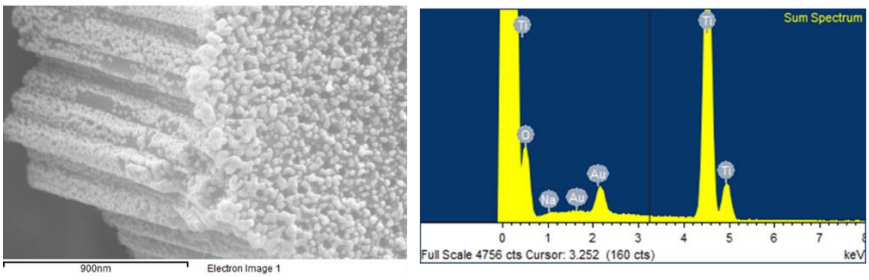

Element	Weight%	Atomic%
O K	50.67	76.95
Ti K	43.24	21.93
Au M	5.69	0.70

Figure 2.7 (a) SEM image of TiO_2 nanotubes coated with Au nanoparticles (b) Corresponding EDS spectrum and calculated composition.

2.3.2 Transmission electron microscopy (TEM)

As opposed to SEM which utilizes the scattered electrons from a sample surface to produce images, a transmission electron microscope uses transmitted electrons through ultrathin samples to create images. The electron beam interacts with the sample and is transmitted through it to create an image which is magnified and focused onto a fluorescent screen. The accelerating voltage of incident electron beam in a TEM is typically 200-300 kV. The pressure in the chamber is of the order 10^{-7} to 10^{-9} Pa. The TEM consists of three sets of lenses: condenser, objective and projector lenses. The condenser lenses (CL1 and CL2) concentrate the beam from the source, the objective lens (OL) focuses the beam through the sample and projector lens expands the beam on phosphor screen.[9] Sample preparation for TEM analysis is an important aspect as the beam typically passes through the specimen and cannot be thick. Nanoparticle samples are prepared by ultrasonicating a

solution of sample in organic solvent such as methanol and drop casting it on a carbon coated copper mesh. Bulk samples are prepared by minting a 0.3 mm disk and making a dimple in the center to sufficiently reduce the thickness for the electron beam to be transmitted through.

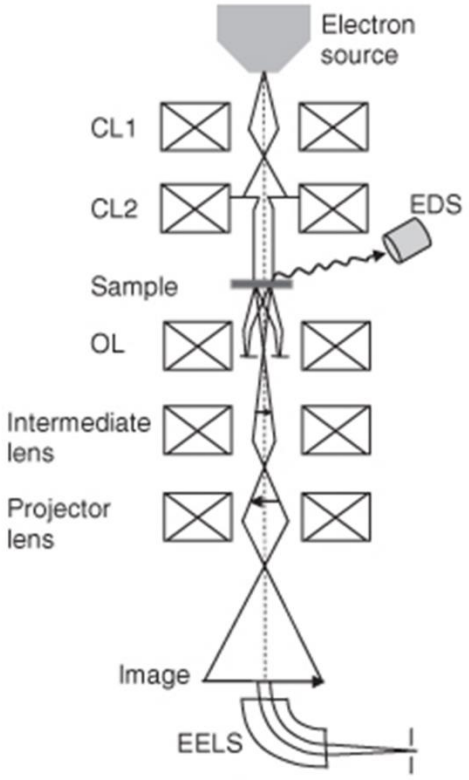

Figure 2.8: A schematic representation of TEM instrument. Figure adopted from ref 9 Copyright 2013, John Wiley and Sons.

A TEM can be used to generate electron diffraction images of the samples by adjusting the back focal plane of the condenser lens on the imaging apparatus. A crystalline sample generates spots which give information about crystal orientation and space group of the sample. A polycrystalline or amorphous samples yield a series of concentric sharp or diffuse rings. The radius of the rings could be used to calculate the *d* spacing of the lattice planes.[10] Figure 2.9 (a) and (b)

shows a low resolution and high resolution TEM image of TiO_2 nanotubes. Corresponding selected area electon diffraction is shown in figure 2.9 (c).

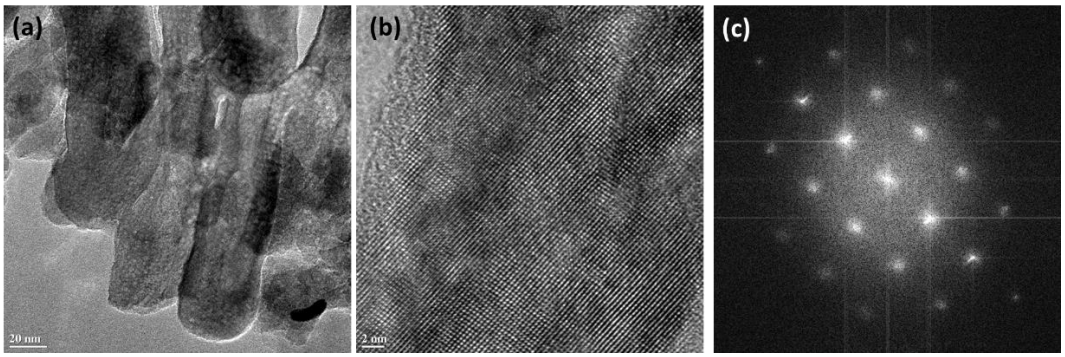

Figure 2.9 TEM image of TiO_2 nanotube (a) low magnification (b) high resolution (c) corresponding electron diffraction image.

2.3.3 X-ray diffraction (XRD)

X-ray diffraction is a technique used to determine the atomic structure and orientation of a crystal from the diffraction data of an incident X-ray beam on the crystal surface. Crystals are regular arrays of atoms in a three dimensional space. The distance between two crystallographic planes (d) and the wavelength of X-rays are of the same order (~ 1-2 Å) which facilitates the diffraction of the incident X-ray beam. A constructive interference occurs when the Braggs condition of diffraction, $2d\ sin\theta = n\lambda$ is met. Where, d is the lattice spacing of the crystal, θ is the incident X-ray radiation angle, λ is the wavelength of X-ray and n is the order of diffraction (figure 2.10 a). A X-ray diffraction spectrum is measured by impinging X-rays at different incident angles on a crystal surface and recording the intensity of diffracted rays. When the intensity of the diffracted X-rays is plotted as a function of the 2θ angle of incident X-rays it yields the X-ray diffraction pattern.[14] The position and intensity of the peaks in a XRD pattern is a signature of a given phase of a material. Figure 2.10 (b) shows the XRD pattern of TiO_2 nanotubes.

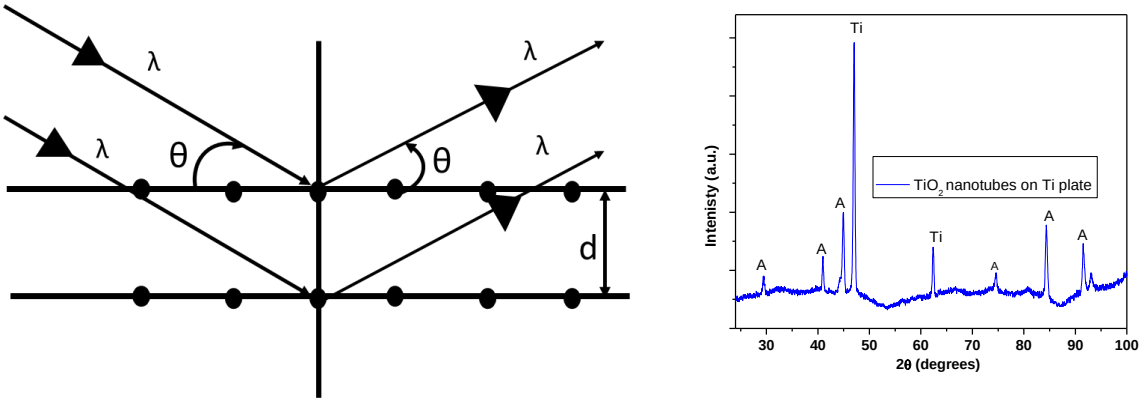

Figure 2.10 (a) Schematic representation of X-ray diffraction from crystal planes (b) XRD spectrum of TiO_2 nanotubes on Ti plate: peaks marked as 'A' indicate TiO_2 anatase phase, 'Ti' indicate metallic titanium.

2.3.4 UV- Vis absorption spectroscopy

Light absorption in a material is a result of excitation of outer electrons. A number of mechanism exists for light absorption such as (i) transition metal ion centers in organic molecules absorb light via d-d transitions, (ii) highly conjugated organic molecules absorb via π orbital transitions, (iii) charge transfer mechanism where donor and acceptor molecules from complexes; and (iv) excitation of electrons from valence band to conduction band, which is commonly observed in semiconductor oxides. This property of absorption in materials could be used for qualitative as well as quantitative analysis of materials based on the Beer-Lambert's law $A = \varepsilon cL$ where A is the absorption, ε is the absorption coefficient, c is the concentration and L is the path length. The UV-Vis spectrophotometer consists of a tungsten filament light source, a monochromator which splits light into different wavelength, a beam splitter to divide the beam to reference, sample chambers and finally a photodiode to record the light passing through the sample. A UV-Vis spectrophotometer records the absorbance, transmittance or reflectance of the

material as function of incident light wavelength. A typical absorption spectrum is shown in figure 2.11.

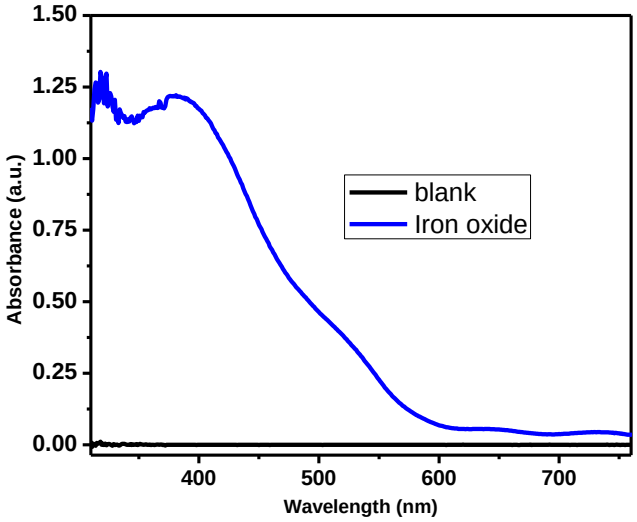

Figure 2.11 UV-Vis absorption spectrum of iron oxide thin film.

2.4 Photoelectrochemical characterization

To study the photoelectrical characteristics of a powder material it is first coated onto a suitable conducting substrate (a transparent conducting oxide coated glass or a metal plate). The coating is usually done by preparing a paste with suitable polymer binders and solutions followed by coating (dip coating, doctor blading or spin coating), the film is dried and finally annealed to discard the organic materials. A good quality electrode comprises of crack free surface, uniform thickness and good adherence to the electrode. In the current study, materials to be studied were directly deposited onto a conducting substrate via CVD or by electrochemical anodization. Electrochemical characteristics of an electrode are studied in a three electrode cell consisting of the material electrode as WE, a platinum wire as CE and a Ag/AgCl electrode as RE, w.r.t which a potential is applied at the working electrode. Since light dependent photoactivity of the materials

are studied the electrochemical characteristics are studied in presence and in absence of a simulated solar light source. A schematic of the set up for photoelectrochemical measurements is shown below.

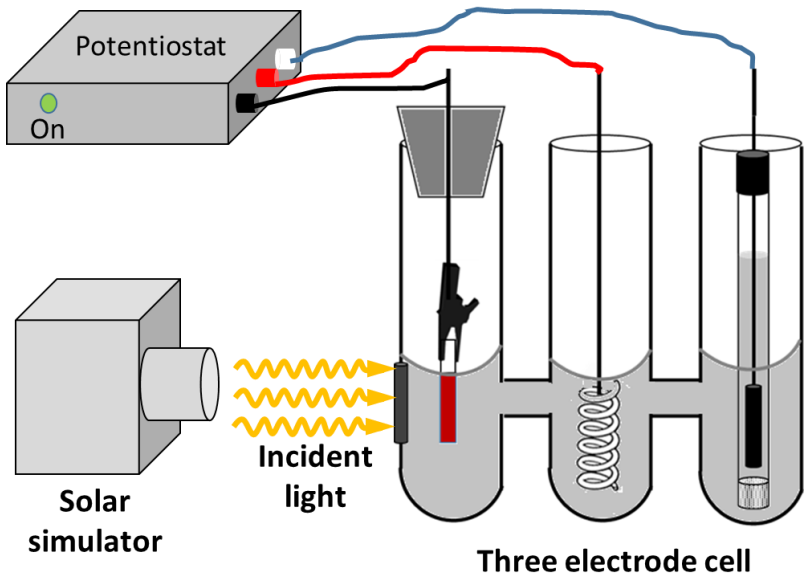

Figure 2.12 Setup for photoelectrochemical characterizations which consists of a three electrode cell, potentiostat and a solar simulator.

2.4.1 Current voltage (I-V) characteristics of a photoelectrode

Current voltage characteristics of an electrode is measured by applying different potential w.r.t the reference electrode at the working electrode and recording the output current in dark and light. I-V characteristics of the electrode depends on the type of oxide (p or n) and the nature of reaction (oxidation or reduction) on its surface, (figure 2.13 a and b).[11] Figure 2.13 c and d shows the I-V characteristics of Fe_2O_3 in a basic solution[12] and Cu_2O electrode in an acidic solution.[13] Iron oxide favors water oxidation on its surface with absorption of radiation due to the suitable position of valence band hence shows a positive (anodic) photocurrent. Copper oxide on the other

shows a negative (cathodic) photocurrent as it favor water reduction reaction on its surface in presence of light. The performance of the electrode is evaluated by the onset potential and the photocurrent obtained at 1.23 V vs RHE. Onset potential is defined as the potential at which the photocurrent starts to increase above the base value. For a photoanode a negative onset potential while for a photocathode a positive onset potential is preferred.

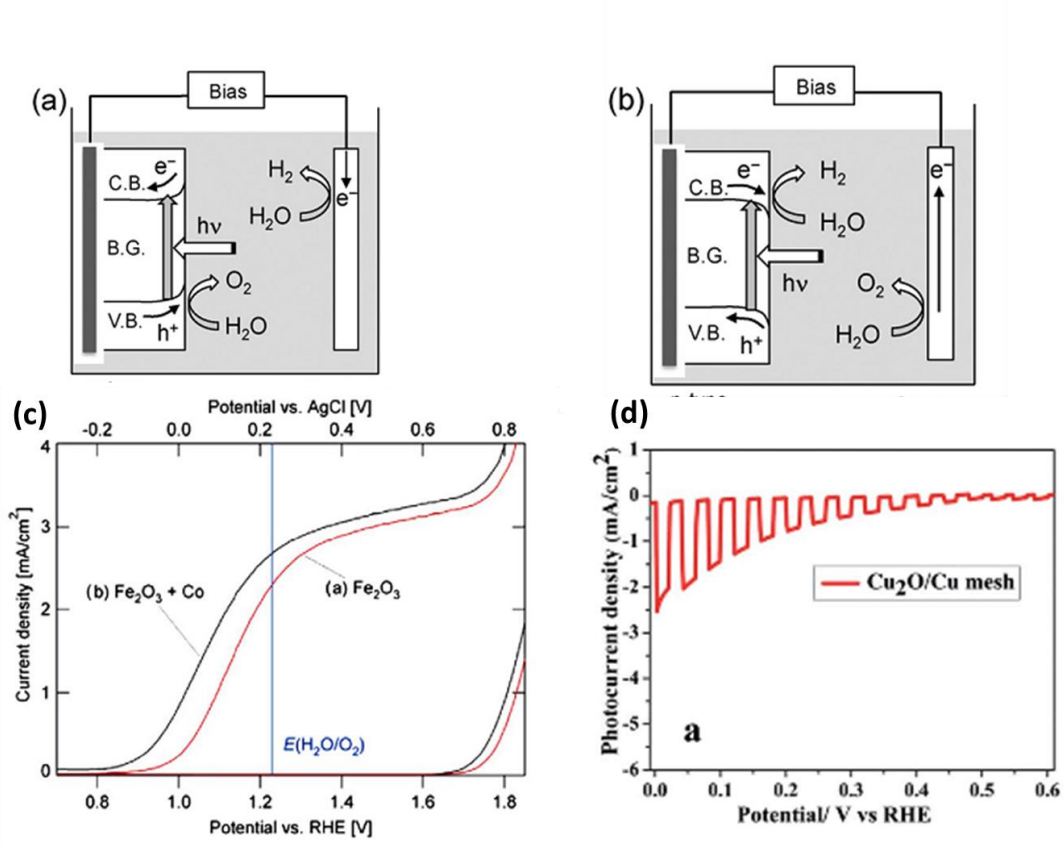

Figure 2.13: (a) Water Oxidation on surface of iron oxide electrode on light irradiation (b) Water reduction of copper oxide electrode on light irradiation, reproduced from ref 11, copyright 2011 Elsevier B.V. (c) Positive photocurrent at iron oxide surface, reproduced from ref 12, copyright 2006, American Chemical Society (d) Negative photocurrent in copper oxide due to reduction, reproduced from ref 13, Copyright 2014, Royal Society of Chemistry.

2.4.2 Incident Photon Conversion Efficiency (IPCE)

Incident photon conversion efficiency is a measure of the efficiency of electrode to convert incident light into electrical energy at a given wavelength. The photocurrent of the electrode as a function of wavelength of light and can be converted to IPCE by the equation, $IPCE(\%) = \frac{1240 \times J_{(\lambda)}}{\lambda \times P_{(\lambda)}}$ where $J_{(\lambda)}$ is the current density in mA/cm^2 obtained at a certain λ (nm) and $P_{(\lambda)}$ is the power of the incident light radiation in mW/cm^2. A typical IPCE graph for hematite thin films is shown in figure 2.14.

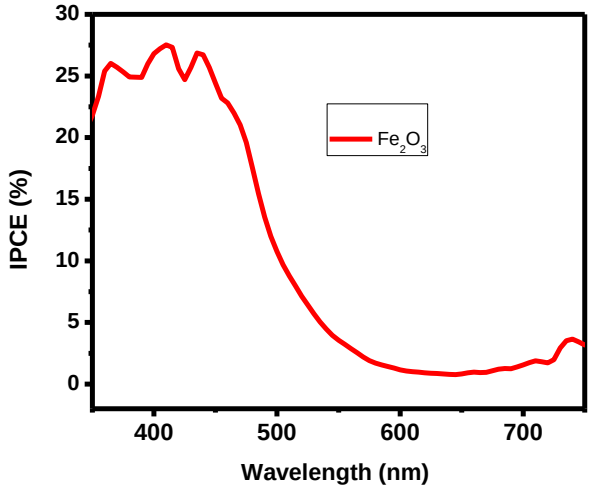

Figure 2.14 IPCE spectrum of a CVD grown iron oxide electrode

2.4.3 Electrochemical Impedance Spectroscopy

Electrochemical impedance spectroscopy is a characterization technique which involves the modulation of Fermi level electrons in a semiconductor by A.C sinusoidal potential of different frequencies (0.01-10^3 Hz) and measuring the corresponding output current. Impedance spectra are

represented as Bode plots (frequency of AC signal vs phase angle) and Nyquist plot (real value vs imaginary value of impedance) at different potentials. A number of important characteristics of the electrode such as the charge carrier density, charge transfer resistance (R_{CT}), series resistance (R_S), trap state resistance (R_T), space charge capacitance (C_{SC}), could be obtained by fitting the Nyquist plot to an equivalent circuit. Figure 2.15 shows the Nyquist plot of hematite electrode in light and dark. The radius of the semicircle is indicative of the R_{CT} of the electrode. In presence of light due to the increase in carriers.

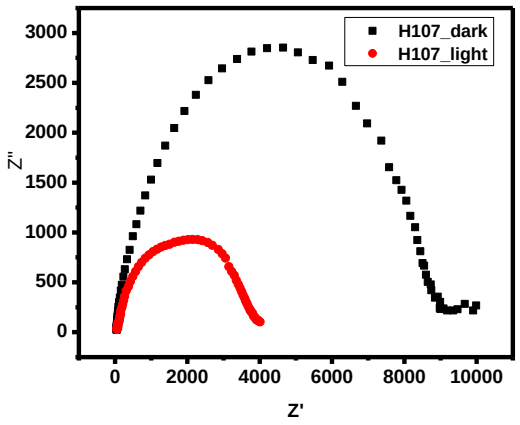

Figure 2.15 Nyquist plot of hematite electrode in light and dark at a potential of 0.4 V vs Ag/AgCl.

2.5 References

(1) Kern, W.; Schuegraf, K. K. In *1 - Deposition Technologies and Applications: Introduction and Overview;* Seshan, K., Ed.; Handbook of Thin Film Deposition Processes and Techniques (Second Edition); William Andrew Publishing: Norwich, NY, **2001**; 11-43.

(2) Moniruddin, M.; Kudaibergenov, S.; Nuraje, N. Chapter 7: Hierarchical Nanoheterostructures for Water Splitting. *RSC Green Chem.* **2016**, *2016-January*, 142-167.

(3) Li, N.; Wang, Y. A.; Iliev, M. N.; Klein, T. M.; Gupta, A. Growth of Atomically Smooth Epitaxial Nickel Ferrite Films by Direct Liquid Injection CVD. *Chemical Vapor Deposition* **2011**, *17*, 261-269.

(4) Grosso, D.; Boissière, C.; Faustini, M. In *Thin Film Deposition Techniques;* The Sol-Gel Handbook; 2015; Vol. 1-3, 277-316.

(5) Birnie, D. P. In *Spin coating: Art and science;* Chemical Solution Deposition of Functional Oxide Thin Films; **2013**; 263-274.

(6) Penner, R. M. Mesoscopic Metal Particles and Wires by Electrodeposition. *J Phys Chem B* **2002**, *106*, 3339-3353.

(7) Zhang, D.; Diao, P. Size-Controlled Electrochemical Synthesis of Hemispherical Gold Nanoparticles on ITO Substrates. *J Electroanal Chem* **2015**, *755*, 174-181.

(8) Zhou, W.; Wang, Z. L. In *Scanning microscopy for nanotechnology: Techniques and applications;* Scanning Microscopy for Nanotechnology: Techniques and Applications; **2007**; 1-522.

(9) Bell, D. C.; Erdman, N.; Brooks, S. In *Low Voltage Electron Microscopy: Principles and Applications;* Low Voltage Electron Microscopy: Principles and Applications; **2012**.

(10) Williams, D. B.; Carter, C. B. In *Transmission electron microscopy: A textbook for materials science;* Transmission Electron Microscopy: A Textbook for Materials Science; **2009**; 1-760.

(11) Abe, R. Recent Progress on Photocatalytic and Photoelectrochemical Water Splitting Under Visible Light Irradiation. *Journal of Photochemistry and Photobiology C: Photochemistry Reviews* **2010**, *11*, 179-209.

(12) Kay, A.; Cesar, I.; Gratzel, M. New Benchmark for Water Photooxidation by Nanostructured α-Fe_2O_3 Films. *J. Am. Chem. Soc.* **2006**, *128*, 15714-15721.

(13) Dubale, A. A.; Su, W.; Tamirat, A. G.; Pan, C.; Aragaw, B. A.; Chen, H.; Chen, C.; Hwang, B. The Synergetic Effect of Graphene on Cu_2O Nanowire Arrays as a Highly Efficient Hydrogen Evolution Photocathode in Water Splitting. *J. Mater. Chem. A* **2014**, *2*, 18383-18397.

(14) Pachauri, N.; Fabrication and Ferromagnetic Resonance Study of Epitaxial Spinel Ferrite Films for Microwave Device Applications, Ph.D. Dissertation **2014**, The University of Alabama.

CHAPTER 3

CHEMICAL VAPOR DEPOSITED HEMATITE THIN FILMS FOR PHOTOCATALYTIC WATER SPLITTING

3.1 Hematite: A superior material for water splitting

Hematite (α-Fe_2O_3) is one of the most promising photocatalysts for water splitting due to its abundance in nature, low cost and high stability. It has a band gap of 1.9-2.2 eV and thus absorbs light in the visible wavelength (330-600 nm) range which makes up ~ 40% of the solar spectrum. It is suitable as a photoanode due its valence band edge (2.24V vs NHE) position being thermodynamically suitable for water oxidation reaction (E^o =1.23 V) by photogenarated holes (figure 3.1).[1] When hematite electrode is immersed in an electrolyte a space charge depletion layer (W) is formed at the electrode surface due to diffusion of charges across the interface. On light irradiation excitons generated in hematite layer are separated to electrons and holes at the depletion layer. The electrons are transported through the material to the counter electrode to carry out the water reduction reaction at the counter electrode and the holes perform water oxidation at the hematite surface. The overall quantum efficiency (η) of a reaction at a semiconductor-liquid junction interface is given by equation 1,[2]

$$\eta = \frac{1-\exp(-\alpha W)+\frac{L_K}{L_K+\alpha^{-1}}\exp(-\alpha W)}{1+\frac{k}{k_\epsilon}\left(\frac{L_D}{\sqrt{2v_0}}+\frac{L_K}{\exp(v_{0)})}\right)} \qquad (1)$$

where, W= depletion width, α= absorption coefficient of the material, L_K = recombination distance, L_D= diffusion length, k = recombination rate of charges, k_ε = Faradaic rate constant and v_0 =degree of band bending. The theoretical calculated efficiency of hematite is 12.7-16.8 %.[2] However, the experimentally obtained values on hematite electrodes are far from the theoretically calculated values due to the poor absorption coefficient, low hole diffusion length of holes and high recombination rate of carriers. The obstacles to obtain the predicted efficiency in hematite are the following: (i) a large value of overpotential for water oxidation, (ii) low absorption coefficient (α) requiring thick (~500 nm) films for effective light absorption; (iii) poor electron conductivity; and (iv) short hole diffusion length (L_D) of ~ 2-4 nm, causing relatively rapid recombination.[1]

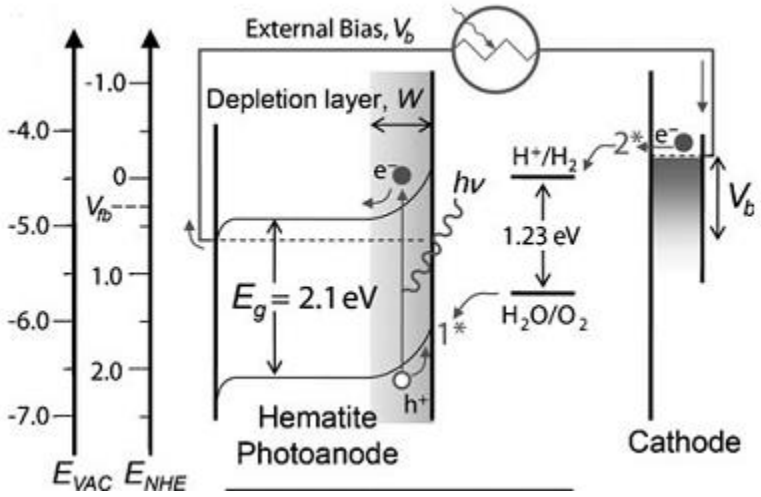

Figure 3.1 Band structure of hematite electrode and mechanism of photocatalytic water splitting when light is incident. Figure reproduced with permission from Ref 1, Copyright 2011 WILEY-VCH Verlag GmbH & Co. KGaA, Weinheim.

3.2 Material characteristics of hematite

Hematite crystallizes in a trigonal-hexagonal lattice system with lattice parameter values of *a*=5.0356 Å, *c*=13.7489 Å with six repeating formulas in a unit cell.[3] The structure of hematite can

be understood by considering it to be made up of FeO_6 octahedrons (figure 3.2). Each octahedron shares edges with three neighboring octahedra in the same plane and one face with an octahedron in an adjacent plane. The face sharing causes a trigonal distortion in the octahedron and thus hematite has two different Fe-O bond lengths.[4]

The electrical conductivity in hematite occurs via a polaron hopping mechanism.[5] Single crystal hematite exhibits anisotropic electrical conductivity. The conduction along the Fe^{3+} bilayer (001) basal plane is up to four orders of magnitude greater than in the perpendicular direction. The transport of both hole and electrons is slow across the basal oxygen planes giving rise to poor conductivity.[1]

The lifetime of excited carriers in hematite is also found to be poor. For example, in epitaxially grown 100 nm thick hematite thin films the hot electrons relax to the valence band within 300 fs, while recombination occurr within 3 ps. The mid-gap Fe^{3+} *d-d* states are the major trap states for recombination. When a bias is applied to deplete the photogenerated holes have an improved lifetime of ~3 s.[1]

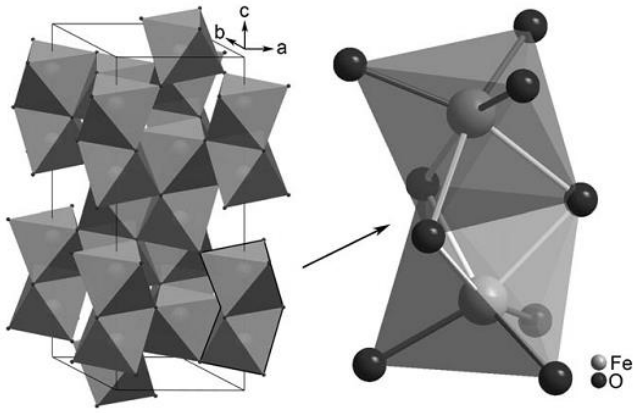

Figure 3.2: Unit cell of hematite formed by repeating units of FeO_6 octahedra (left). Face sharing of octahedral to form FeO_9 dimers. Reprinted with permission from ref 22. Copyright 2010 American Chemical Society.

The conduction band of hematite comprises of empty Fe^{3+} *3d* orbitals and the valence band consisting of full $2t_{2g}$ Fe *3d* ligand field orbitals with some contribution from the oxygen antibonding *2p* orbitals.[6] Density functional theory (DFT) based calculations and Tauc analysis of absorption of hematite indicates it to be an indirect band gap semiconductor.[7, 8] The absorption in hematite begins in the infra-red region due to the Fe^{3+} *d-d* transitions and increases at the band gap (visible and UV region) due to the additional absorption from O *2p* orbitals to Fe^{3+} *3d* orbitals.[9] The absorption coefficient (α) of hematite is of order 10^5 cm^{-1} in the visible and UV region.[1]

3.3 Strategies employed to enhance photocurrent in hematite

3.3.1 Nanostructuring

The thickness of hematite electrode is limited by its hole diffusion lengths (2-4 nm). However its low absorption coefficient requires a much thicker hematite layer. Thus a suitable hematite electrode would be vertically aligned nanotubes or nanowires with 5-10 nm in diameter and a thickness of 450- 500 nm.[10] Vertically aligned nanostructures provide a direct pathway for the transport of carriers in the electrode thus helping in increasing the thickness of electrode without compromising the diffusion length. Synthesis of vertically aligned 1-D hematite wires on substrates have been reported using several techniques such as hydrothermal[11], and electrochemical anodization[12] and have shown improved performance (figure 3.3). In addition to nanowires, vertically grown porous cauliflower - like structures by atmospheric pressure chemical vapor deposition (APCVD) with feature size of 5-10 nm have shown photocurrents as high as 1.8 mA/cm^2 at 1.23 V vs RHE.[13]

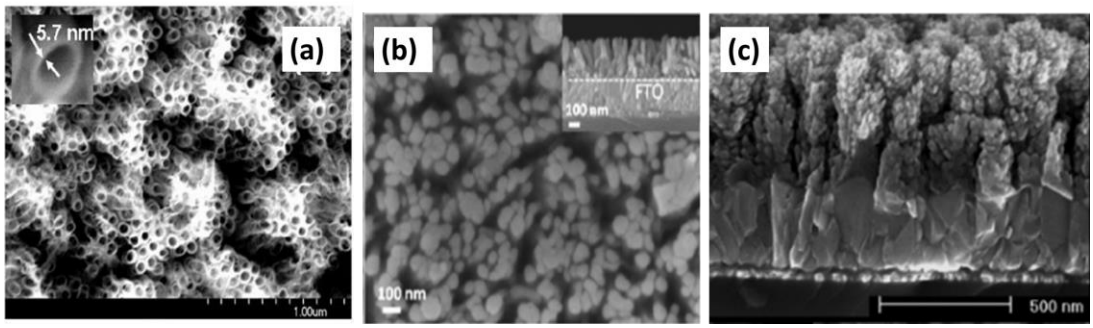

Figure 3.3 Morphology of vertically alligned hematite nanostructures (a) nanotubes, (b) nanowires, and (c) cauliflower -like hematite. Reprinted with permission from ref 11, 12, 13 copyrights (2009, 2012, 2006) American Chemical Society.

3.3.2 Doping

The conductivity in pure crystalline hematite is of the order of $10^{-14}\ \Omega^{-1}\ cm^{-1}$ with a carrier density of (~ $10^{18}\ cm^{-3}$) which limits the photoactivity.[10] The conductivity can be increased by substitutional doping of atoms such as Mg^{2+}, Cu^{2+} (p- type) or with Ti^{4+}, Si^{4+}, Zr^{4+} (n- type) etc.[14] Gratzel et al reported an increase in photocurrent in cauliflower like Fe_2O_3 structures on doping with Si^{4+} due to an increase in carrier density to up to $1.7\times10^{20}\ cm^{-3}$.[15]

3.3.3 Surface treatment with co-catalysts

The hole transport across the hematite-electrolyte interface is quite sluggish which causes higher overpotential for the electrode and pushes the water oxidation to positive onset potentials. Several oxygen evolution catalysts such as Co-Pi (a cobalt phosphate oxygen evolution catalyst), IrO_2 and cobalt oxide (Co_3O_4) have been used with hematite.[10] Surface catalysts act as an effective mediator to ease hole transfer from the electrode surface to electrolyte, reducing the kinetic barrier. The photocurrent of hematite surface modified by IrO_2 nanoparticles, prepared by APCVD method is shown to increase by ~ 0.5 mA/cm^2 and the onset potential shifted by 0.2 V.[16]

To summarize, the overall hematite performance can be improved by increasing the number of charge carriers in the electrode (doping and nanostructuring) and reducing the overpotential for water oxidation (surface catalysts), as shown in figure 3.4.

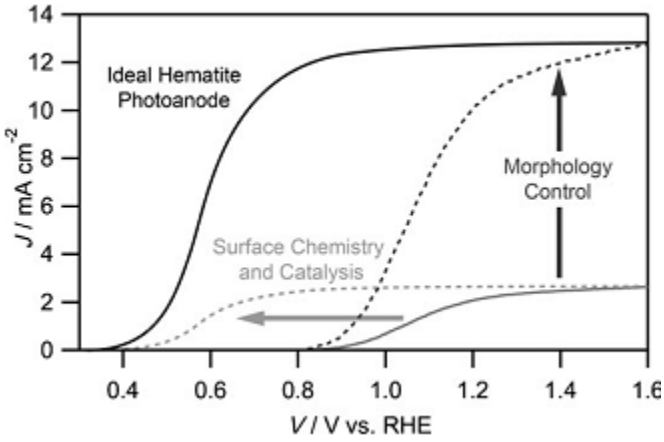

Figure 3.4: Enhancing overall hematite performance by increasing the carriers by nanostructuring and doping, improving onset potential by surface catalyst. Figure reproduced with permission from Ref 1, Copyright 2011 WILEY-VCH Verlag GmbH & Co. KGaA, Weinheim.

3.4 Hematite thin films for photocatalysis

Considering the drawbacks and strategies outlined in the previous sections, high surface mesoporous oxide films are an obvious choice over compact thin films for high photo electrochemical performance. However with increasing surface area, the number of structural defects induced in the electrode reduces its performance (figure 3.4). Thin films grown by high temperature deposition techniques such as chemical vapor deposition (CVD) have the advantage of high range crystallinity and orientation of grains to maximize carrier transport. By tailoring the film thickness and particle size to be about the same dimension of the depletion layer, recombination of carriers can be reduced. Several groups have reported the synthesis of hematite

by different CVD techniques, the most cited one being the cauliflower - like hematite grown by APCVD by Gratzel et al.[17] Plasma enhanced CVD (PECVD)[18] and ultrasonic spray pyrolysis[19] techniques have also been utilized to synthesize good quality hematite on FTO substrates. PE-CVD technique reported by Mathur *et al* produced hierarchical morphologies that could be finely tailored as a function of deposition parameters and annealing. In addition, they succeeded in obtaining grains with (110) overall orientation which enhanced the photoelectrochemical performance of the electrode.[20] Their thickness dependent study also indicated that as feature size increased with film thickness, affecting the diffusion of Sn^{4+} ions from FTO substrate into hematite thus decreasing the overall photoactivity.[21, 22]

Besides the grain size and orientation, the underlayer also plays a crucial role in the photoelectrochemical performance of the electrodes. Bisquert *et al* studied the effect Nb_2O_5 and SiO_2 underlayers on 100 nm thick hematite by spray pyrolysis and observed that doping from underlayers helped in increasing the carrier density. Moreover, an overlayer of Ga_2O_3 helped to shift the onset potential by 200 mV by surface passivating the surface states in hematite.[23] Thus choosing a suitable underlayer can aid in achieving optimum photoelectrochemical performance for a given method of deposition. In the current chapter the synthesis of hematite films by a DLI-CVD has been outlined. To obtain maximum photocurrent from the electrodes various interfacial oxide layers have been investigated.

3.5 Experimental methods

3.5.1 FTO substrate cleaning and TiO_2 layer coating:

FTO coated glass substrates (1.5 cm × 1 cm; 25 Ω/□, Pilkington Glass Co. Ltd., U.S.A) were cleaned using detergent followed by washing with copious amount of DI water prior to being cleaned ultrasonically in acetone and isopropanol, each for 30 min.

3.5.2 Preparation and deposition of different interlayers

(i) Thin layers (~ 50nm) of TiO_2, Nb_2O_5, ZnO, NiO and SiO_2

The precursor solutions for deposition of thin layers of metal oxide interlayers were prepared by dissolving 0.05% of titanium isopropoxide, niobium ethoxide, zinc acetylacetonate, nickel acetylacetonate or tetraethylorthosilicate in absolute ethanol. The resulting solution was spin coated on FTO glass and annealed in a box furnace at 500^oC to yield ~50 nm thick TiO_2, Nb_2O_5, ZnO, NiO or SiO_2 films.

(ii) Titania (TiO_2) layer of ~100 nm thickness

A polymeric titania sol was prepared by dissolving polyvinylpyrrolidone (0.3 g, PVP, MW ~ 180,000) in ethanol (3.5 ml) followed by drop-wise addition of titanium isopropoxide (0.5 g) and acetic acid (1ml). The titania sol was spin-coated onto the cleaned FTO glass at 3500 rpm for 30 seconds. The titania coated FTO plates were then annealed in air at 500 ^oC in a box furnace for 30 minutes and cooled to room temperature to produce a ~100 nm thick TiO_2 layer.

(iii) Mesoporous titania layers

Mesoporous titania layers of 1 μm thickness were deposited on FTO substrate by doctor blading a commercial Degussa P25 TiO_2 paste. A 0.2% TiO_2 paste diluted in absolute ethanol was spin coated to obtain a 150 nm thick TiO_2 mesoporous particle layer.

3.5.3 Deposition of hematite

Direct liquid injection chemical vapor deposition (DLI-CVD) technique was used for the deposition of α-Fe_2O_3 films on different substrates. A 0.05 M iron acetylacetonoate solution in dimethyl formamide (DMF) was used as precursor solution. The following deposition conditions were used for growing Fe_2O_3 on FTO substrates. Hematite was deposited for 1 hour to obtain a film thickness of 230 nm.

Deposition parameter	**Values**
Argon (career gas) flow rate	300 sccm
Oxygen flow rate	120 sccm
Base pressure	1 Torr
Precursor solution flow rate	4 g/hr
Deposition temperature	500 ^oC

Table 3.1: Hematite deposition conditions.

3.5.4 Structural and photoelectrochemical characterizations:

SEM images of the samples were recorded by using a JEOL 7000 scanning electron microscope. The absorption characteristics of the films were recorded with a UV-Visible spectrophotometer (Agilent, Cary 500, USA). X-ray diffraction (XRD) patterns of the samples were measured by an X-ray diffractometer (XRD, Bruker D8) employing CoKα (λ=1.789 Å) radiation. The water splitting characteristics of the films were studied by recording I-V characteristics in a three-electrode cell configuration consisting of a platinum wire and Ag/AgCl (saturated with KCl) as counter and reference electrodes, respectively, in 0.5 M NaOH. The electrode potential was scanned from -0.5 to 1.0 V using a potentiostat (Princeton EG&G Applied

Research) and the corresponding current was recorded. The measurements were performed in dark and under light using a Xe arc lamp at AM 1.5G conditions. Electrochemical impedance spectra of the electrodes in three-electrode configuration were recorded in the dark and under light conditions using a CHI760 bipotentiostat (CH Instruments, Inc., Austin, TX**)** in the 0.1 Hz-10 KHz frequency range from a voltage range of -0.2 to 0.7 V (vs. Ag/AgCl).

3.6 Results and discussions

3.6.1. Morphological and structural characterizations

SEM images of the interlayer oxides and hematite coated oxides were record. Figure 3.5(a) and (b) show the surface morphology of the oxide coated FTO substrates and hematite (230 nm) coated on the oxide layers. The interlayers are not thick enough to be observed in the cross sectional SEM, hence estimated to be < 20 nm.

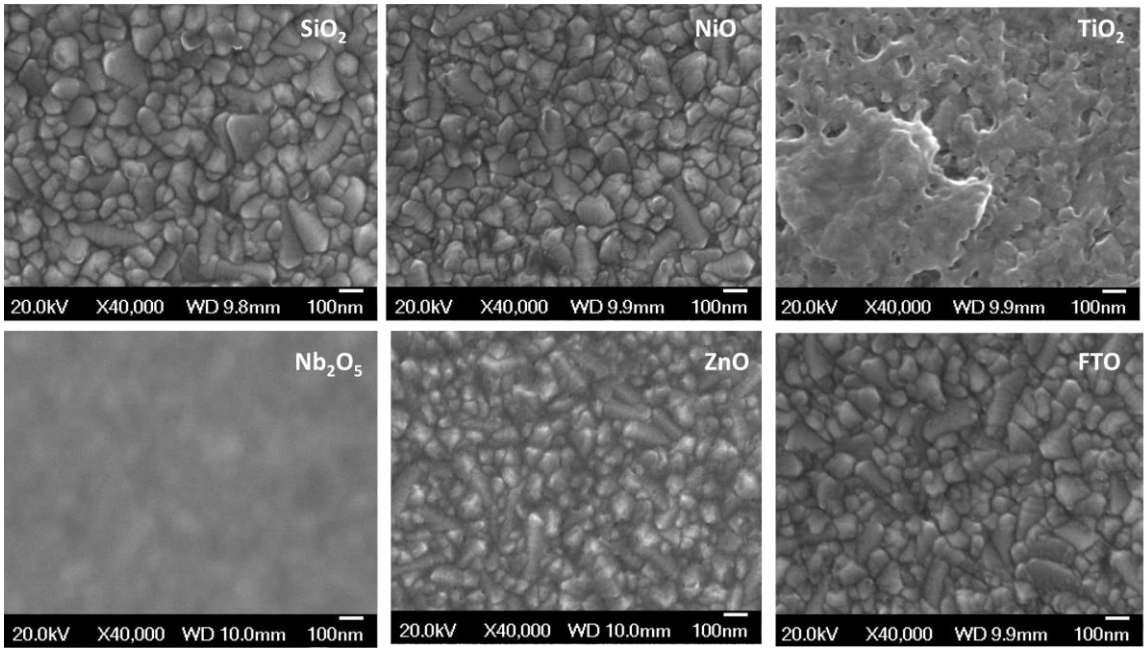

Figure 3.5 (a) Surface morphology of oxide layers prepared by spin coating.

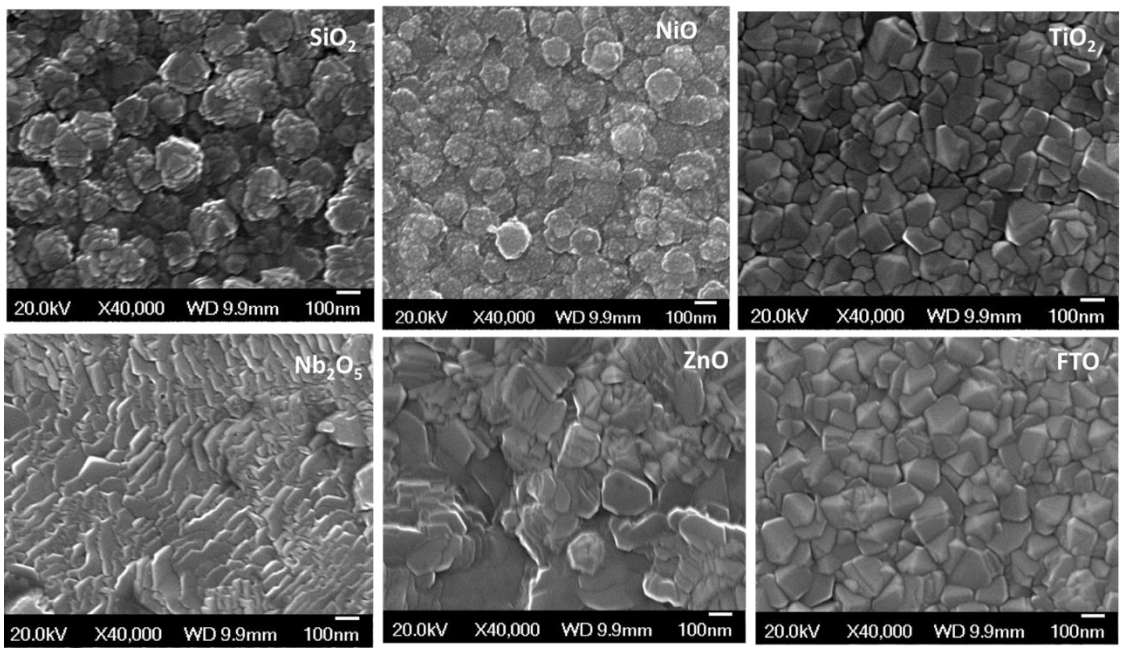

Figure 3.5 (b) Surface morphology of hematite deposited by CVD on different oxide layers.

The interlayer oxides influences the grain size and the morphology of the hematite film grown by CVD. Cross section SEM images of samples have been taken from which the thickness of deposited hematite is observed to be 230 nm (figure 3.6 a). The UV-Vis spectrum of the hematite deposited on different oxide interlayers is shown in figure 3.6 (c). All samples show samilar absorbance values, hence have the similar thickness of α-Fe_2O_3 and there is no significant contribution to the spectra from the oxide underlayer. We can thus expect that any discrepancies in the film characteristics are not due to variations in thickness of the α-Fe_2O_3. XRD patterns of the deposited films (figure 3.7) show only the hematite phase with peaks indicated with asterisk corresponding to the FTO.

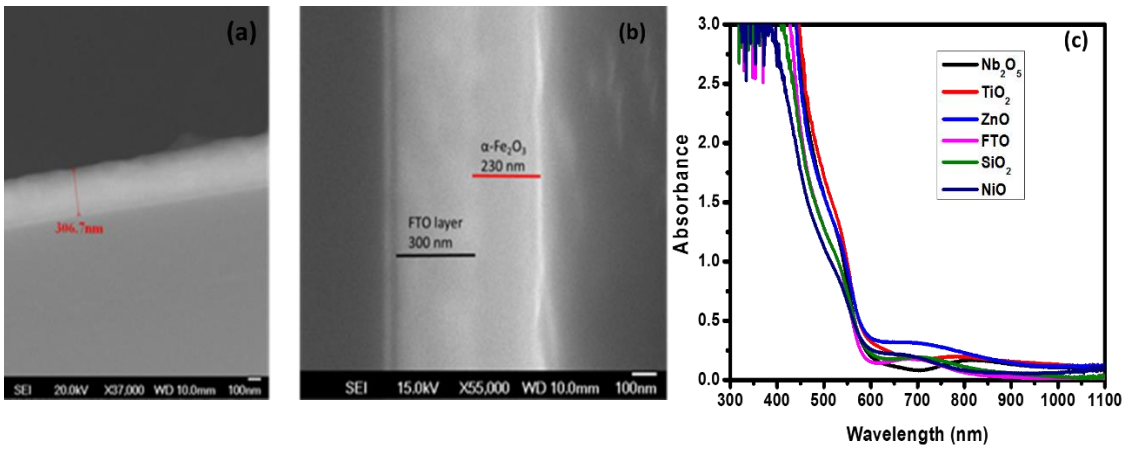

Figure 3.6 : Cross section image of (a) bare FTO showing thickness of FTO=300 nm, (b) FTO coated with hematite, thickness = 230 nm, (c) Absorption spectrum of hematite on different interlayers.

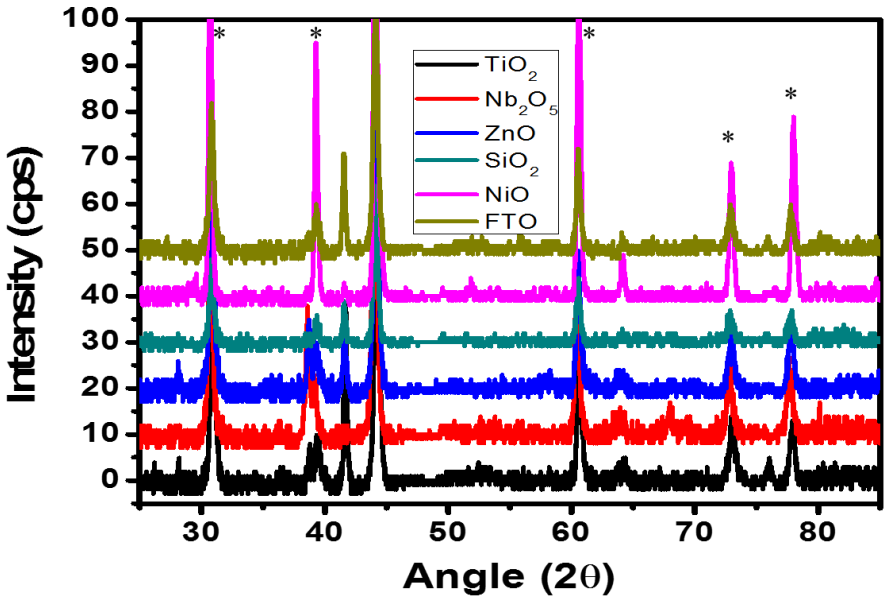

Figure 3.7 XRD patterns of hematite on different oxide layers on FTO. The order from the bottom correspond to hematite on TiO_2, Nb_2O_5, ZnO, SiO_2, NiO and FTO.

3.6.2 Current-voltage characteristics:

The PEC water splitting performance of hematite electrodes was tested by recording the current - voltage (I-V) characteristics in the dark and under irradiation conditions. It was observed that

hematite grown on SiO_2 and NiO showed photocurrents less than 0.1 mA/ cm^2 (figure 3.8 a). This could be due to NiO being p - type oxide causing recombination of electrons being transferred through FTO to the counter electrode. The SiO_2 layer on the other hand possibly acts as an electron barrier layer causing recombination of carriers in hematite. Thus SiO_2 and NiO were ruled out from further detailed characterization due to poor photocurrent obtained. Hematite grown on n- type oxide layers TiO_2, Nb_2O_5, and ZnO show photocurrents higher than that on the bare FTO (figure 3.8 (b)). Additionally, improved onset potentials for water oxidation were observed for hematite grown on TiO_2 and Nb_2O_5 as compared to that on ZnO and bare FTO.

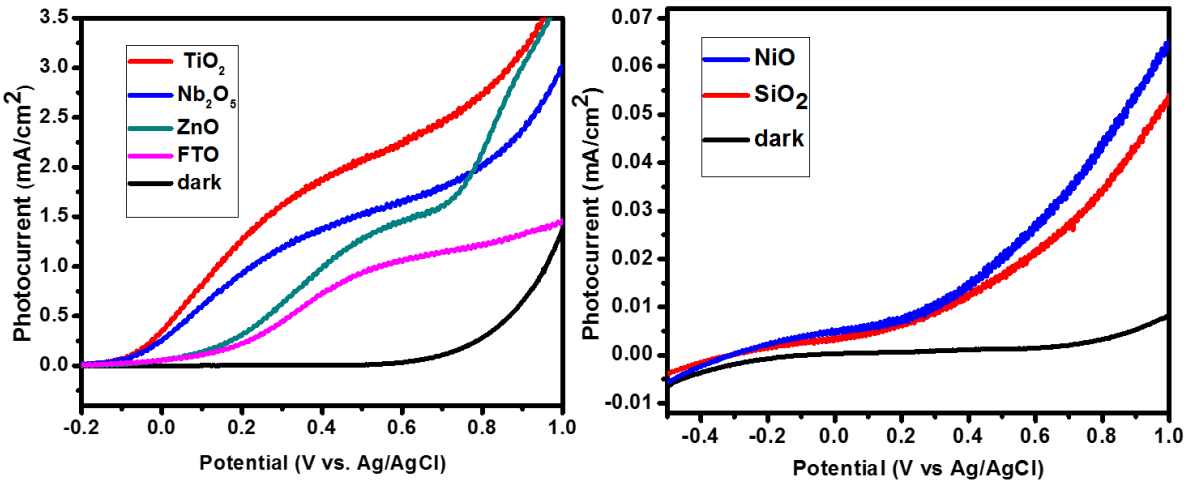

Figure 3.8: I-V characteristics of hematite electrode on (a) from the bottom dark current, FTO, ZnO, Nb_2O_5, TiO_2 (b) From the bottom dark current, SiO_2, NiO. Graphs recorded in 0.1 M KOH in a three electrode cell with Pt wire as a counter electrode at a scan rate of 20 mV/s.

3.6.3 Mott Schottky plots and electrochemical impedance spectroscopy studies:

Mott-Schottky analysis has been performed on the hematite deposited on FTO, ZnO, Nb_2O_5, and TiO_2. Capacitance (C) of the samples are calculated from the imaginary component Z" of the impedance spectra by the equation, $Z'' = \frac{1}{2\pi f C}$. Mott-Schottky plots of the samples are obtained by

plotting ($1/C^2$) vs. the potential (V vs Ag/AgCl) values in the dark (figure 3.9). The plots are fitted to a straight line and the slopes are used to calculate the carrier densities using equation 1:

$$\frac{1}{C^2} = \frac{2}{A^2 q \varepsilon \varepsilon_0 N_D}\left(V - V_{fb} - \frac{kT}{q}\right) \ldots\ldots \quad (2)$$

where A is the area of the film, q is the elementary charge, ε_0 is the permittivity of free space, ε is the dielectric constant of the hematite (ε=80, for hematite[15]), *k* is the Boltzmann constant, T is the absolute temperature of the system, V is the applied potential and V_{fb} is the flat band potential. Table 1 shows the extracted carrier densities for each electrode. In spite of poor electrochemical performance the number of carriers in hematite grown on ZnO ($7.16\times10^{17}/cm^3$) is determined to be higher as compared to that obtained on TiO_2 and Nb_2O_5 ($1.46\times10^{17}/cm^3$). Hematite grown on FTO shows an order of magnitude lower charge carrier density of $4.16\times10^{16}/cm^3$. While flat band potentials calculated from the Y intercept of the straight lines, show the highest value for hematite on FTO.

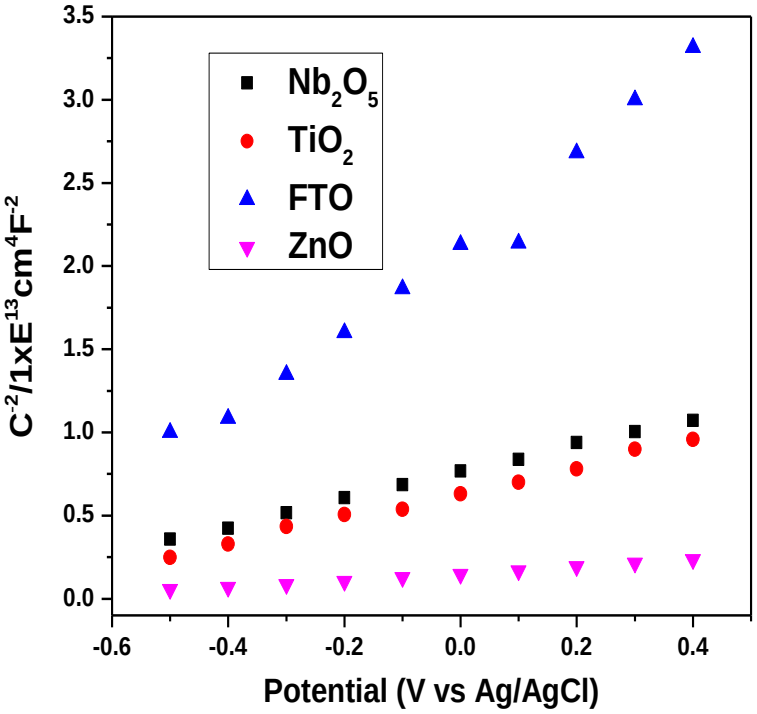

Figure 3.9: Mott Schottky for plots hematite electrode on (from the bottom) ZnO (pink downwards pointing triangle), TiO_2 (red circles), Nb_2O_5 (black squares), FTO (blue, upward pointing triangles).

Interlayer	**Electron density (/cm^3)**	**Flat band potential (V vs Ag/AgCl)**
Nb_2O_5	1.41×10^{17}	-1.06
TiO_2	1.67×10^{17}	- 1.21
FTO	4.14×10^{17}	- 0.83
ZnO	7.16×10^{17}	- 1.34

Table 3.2: Extracted charge carrier densities from hematite on different oxide layers.

Nyquist plots were recorded for each electrode at 0.2 V vs. Ag/AgCl in light (figure 3.10). The diameter of the semicircles represent the charge transfer resistance. It was observed that the hematite on ZnO electrode has a higher charge transfer resistance, which explains the reason for poor photocurrent in hematite on ZnO electrode. Bode plots were obtained from the Nyquist plots to extract the rate constant for charge transfer (k_t) and charge recombination (k_r) and the space charge capacitance (C_{SC}) of the films. The k_t and k_r values were obtained from the peak value of phase angle at low and high frequencies of Bode plots, respectively. The space charge capacitance values were calculated from the following equation:[24]

$$C_{SC} = \frac{1}{k_r(Z'' - R_s)}$$

where, Z'' is the value of the imaginary part of impedance at the point of intersection of peaks and R_{ser} is the series resistance obtained from the first point of the Nyquist plot.

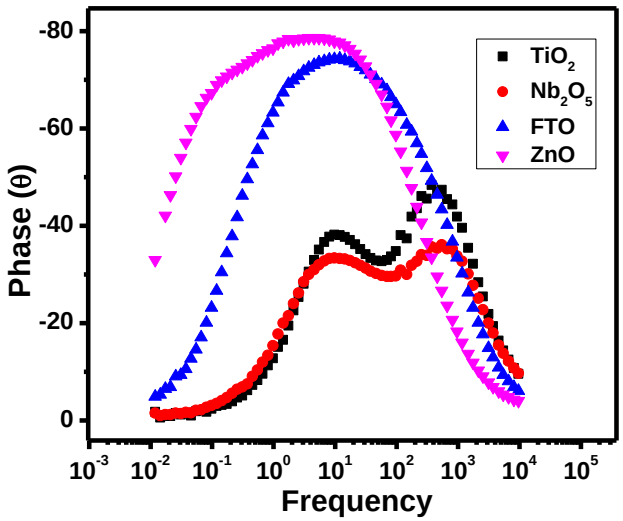

Figure 3.10: Bode plots of hematite on (from the bottom) Nb_2O_5, TiO_2, FTO, ZnO at 0.2 V vs. Ag/AgCl under 1 Sun condition.

Interlayer oxide	**k_t (s^{-1})**	**k_r (s^{-1})**	**Ratio (k_t/k_r)**	**C_{SC} (F)**
TiO_2	9.77±0.01	75.98±0.01	0.128	8.001×10^{-6} $\pm0.05\times10^{-6}$
Nb_2O_5	9.77±0.01	83.87±0.01	0.116	7.026×10^{-6} $\pm0.1\times10^{-6}$
FTO	2.55±0.01	275.58±0.01	0.009	1.994×10^{-4} $\pm0.05\times10^{-4}$
ZnO	0.12±0.01	21.99±0.01	0.005	1.326×10^{-6} $\pm0.1\times10^{-6}$

Table 3.3: Extracted values for rate constant for charge transfer (k_t) and charge recombination (k_r) and space charge capacitance (C_{SC}).

Similar values of k_t and k_r were obtained for hematite films on TiO_2 and Nb_2O_5 with C_{sc} values in the order of 1×10^{-6}. A lower value of capacitance indicates carriers being transported effectively in the electrode. The k_r value for FTO was highest indicating higher recombination in the hematite film with one order higher value of capacitance as compared to TiO_2. The ratio of transfer to recombination events was the lowest for FTO and ZnO films. The capacitance value for hematite on ZnO film was the highest indicating higher number of defects in hematite grown on ZnO film resulting in charges to be trapped causing recombination. Thus TiO_2 was found to be the most effective electron transport layer. Hematite grown on TiO_2 possibly had least defects, which gave a higher photocurrent as compared to ZnO and FTO.

3.6.4 Effect of TiO_2 porosity on hematite photoactivity

The effect of TiO_2 thickness and porosity of TiO_2 on the performance of hematite was also tested. These included (a) 50 nm thin layer, (b) 100 nm porous, (c) 150 nm mesoporous particle layer, and (d) 1 micron mesopoprous particle layer. Figure 3.11 shows the surface morphology of the TiO_2 layers. Hematite (230 nm thick) was deposited on the TiO_2 layers and I-V characteristics were recorded to measure the water splitting activity. Hematite on 50 nm thick TiO_2 layer showed the best photocurrent of 1.5 mA/cm^2, followed by hematite on 100 nm porous particle layer of 1.2 mA/cm^2 (figure 3.12). Increasing the thickness and porosity of the TiO_2 layers resulted in an increase in the the onset potential of the hematite electrode and shift to positive values. This could be attributed to the defects induced due to the high surface area.

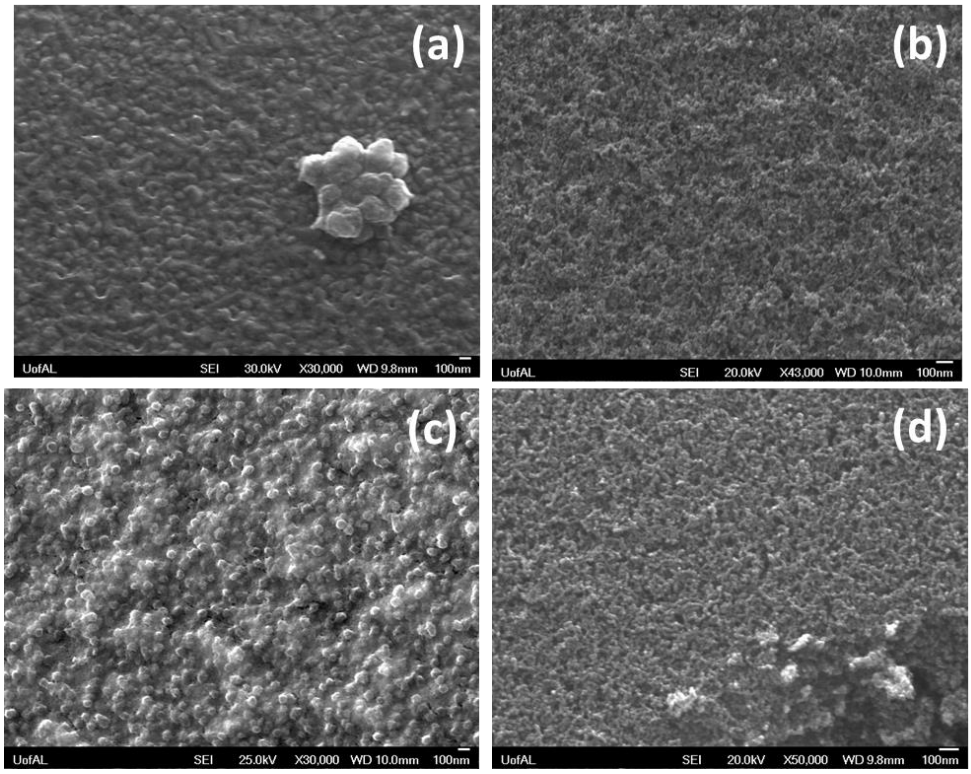

Figure 3.11: Surface morphology of the TiO_2 layers (a) 50 nm thin layer (b) 100 nm porous (c) 150 nm mesoporous particle layer, and (d) 1 μm mesoporous particle layer.

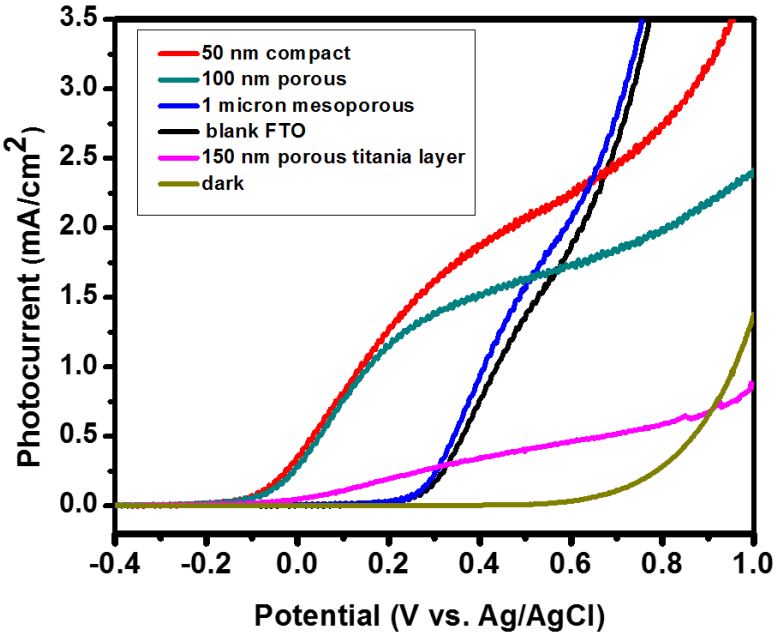

Figure 3.12: I-V characteristics of hematite on different thickness and porosity TiO_2 layers (from the bottom) (a) dark current (b) 1 μm mesoporous particle layer (c) blank FTO (d) 150 nm mesoporous particle layer (e) 100 nm porous layer (f) 50 nm thin layer

3.7 Conclusions

The DLI-CVD process was optimized to grow high quality phase-pure α-Fe_2O_3 on FTO substrates. Different n- and p- type oxides were used as interlayers to obtain optimum photocurrent. It was observed that the nature of the interlayer oxide influenced the photoelectrochemical water oxidation performance of the hematite. The interlayer oxides affect the grain growth characteristics of the hematite possible due to ion diffusion from the substrate. The n- type oxides (TiO_2, Nb_2O_5 and ZnO) proved to better interlayers as compared to p-type interlayers (SiO_2, NiO). A detailed impedance spectroscopic study of hematite electrodes indicated

that the highest carrier density in hematite grown on ZnO but due to poor charge transfer rate at the surface due to high defect concentration they showed poor photocurrent. TiO_2 and Nb_2O_5 proved to be ideal electron transport layer without inducing defects in hematite film. The morphology and thickness of the TiO_2 layer also affected the performance of the hematite. A thin 50 nm TiO_2 layer gives the highest photocurrent. As the thickness and porosity of the underlying TiO_2 increased the photocurrent in hematite films reduced due to increasing resistance and higher porosity inducing surface defects. The water splitting performance of hematite was optimized with TiO_2 interlayer and its morphology.

3.8 References

(1) Sivula, K.; Le Formal, F.; Grätzel, M. Solar Water Splitting: Progress using Hematite (α-Fe_2O_3) Photoelectrodes. *ChemSusChem* **2011**, *4*, 432-449.

(2) Lin, Y.; Yuan, G.; Sheehan, S.; Zhou, S.; Wang, D. Hematite-Based Solar Water Splitting: Challenges and Opportunities. *Energy Environ. Sci.* **2011**, *4*, 4862-4869.

(3) Cornell, R. M.; Schwertmann, U. In *Introduction to the Iron Oxides;* The Iron Oxides; Wiley-VCH Verlag GmbH & Co. KGaA: **2004**; pp 1-7.

(4) Cornell, R. M.; Schwertmann, U. In *Crystal Structure;* The Iron Oxides; Wiley-VCH Verlag GmbH & Co. KGaA: 2004; pp 9-38.

(5) Rettie, A. J. E.; Chemelewski, W. D.; Emin, D.; Mullins, C. B. Unravelling Small-Polaron Transport in Metal Oxide Photoelectrodes. *J. Phys. Chem. Lett.* **2016**, *7*, 471-479.

(6) Gilbert, B.; Frandsen, C.; Maxey, E. R.; Sherman, D. M. Band-Gap Measurements of Bulk and Nanoscale Hematite by Soft X-Ray Spectroscopy. *Phys. Rev. B Condens. Matter Mater. Phys.* **2009**, *79*.

(7) Praveen, C. S.; Timon, V.; Valant, M. Electronic Band Gaps of Ternary Corundum Solid Solutions from Fe_2O_3-Cr_2O_3-Al_2O_3 System for Photocatalytic Applications: A Theoretical Study. *Comput Mater Sci* **2012**, *55*, 192-198.

(8) Townsend, T. K.; Sabio, E. M.; Browning, N. D.; Osterloh, F. E. Photocatalytic Water Oxidation with Suspended α-Fe_2O_3 Particles-Effects of Nanoscaling. *Energy Environ. Sci.* **2011**, *4*, 4270-4275.

(9) Ma, Y.; Johnson, P. D.; Wassdahl, N.; Guo, J.; Skytt, P.; Nordgren, J.; Kevan, S. D.; Rubensson, J.; Baske, T.; Eberhardt, W. Electronic Structures of α-Fe_2O_3 and from Fe_3O_4 from O *K* -Edge Absorption and Emission Spectroscopy. *Phys. Rev. B* **1993**, *48*, 2109-2111.

(10) Bassi, P. S.; Gurudayal; Wong, L. H.; Barber, J. Iron Based Photoanodes for Solar Fuel Production. *Phys. Chem. Chem. Phys.* **2014**, *16*, 11834-11842.

(11) Xi, L.; Tran, P. D.; Chiam, S. Y.; Bassi, P. S.; Mak, W. F.; Mulmudi, H. K.; Batabyal, S. K.; Barber, J.; Loo, J. S. C.; Wong, L. H. Co_3O_4-Decorated Hematite Nanorods as an Effective Photoanode for Solar Water Oxidation. *J. Phys. Chem. C* **2012**, *116*, 13884-13889.

(12) Mohapatra, S. K.; John, S. E.; Banerjee, S.; Misra, M. Water Photooxidation by Smooth and Ultrathin Fe_2O_3 Nanotube Arrays. *Chem. Mater.* **2009**, *21*, 3048-3055.

(13) Kay, A.; Cesar, I.; Gratzel, M. New Benchmark for Water Photooxidation by Nanostructured Alpha-Fe_2O_3 Films. *J. Am. Chem. Soc.* **2006**, *128*, 15714-15721.

(14) Mettenbörger, A.; Gönüllü, Y.; Fischer, T.; Heisig, T.; Sasinska, A.; Maccato, C.; Carraro, G.; Sada, C.; Barreca, D.; Mayrhofer, L.; Moseler, M.; Held, A.; Mathur, S. Interfacial Insight in Multi-Junction Metal Oxide Photoanodes for Water-Splitting Applications. *Nano Energy* **2016**, *19*, 415-427.

(15) Cesar, I.; Sivula, K.; Kay, A.; Zboril, R.; Grätzel, M. Influence of Feature Size, Film Thickness, and Silicon Doping on the Performance of Nanostructured Hematite Photoanodes for Solar Water Splitting. *Journal of Physical Chemistry C* **2009**, *113*, 772-782.

(16) Tilley, S. D.; Cornuz, M.; Sivula, K.; Grätzel, M. Light-Inducedwater Splitting with Hematite: Improved Nanostructure and Iridium Oxide Catalysis. *Angew. Chem. Int. Ed.* **2010**, *49*, 6405-6408.

(17) Warren, S. C.; Voïtchovsky, K.; Dotan, H.; Leroy, C. M.; Cornuz, M.; Stellacci, F.; Hébert, C.; Rothschild, A.; Grätzel, M. Identifying Champion Nanostructures for Solar Water-Splitting. *Nature Materials* **2013**, *12*, 842-849.

(18) Singh, A. P.; Mettenbörger, A.; Golus, P.; Mathur, S. Photoelectrochemical Properties of Hematite Films Grown by Plasma Enhanced Chemical Vapor Deposition. *Int J Hydrogen Energy* **2012**, *37*, 13983-13988.

(19) Duret, A.; Grätzel, M. Visible Light-Induced Water Oxidation on Mesoscopic α-Fe_2O_3 Films made by Ultrasonic Spray Pyrolysis. *J Phys Chem B* **2005**, *109*, 17184-17191.

(20) Warwick, M. E. A.; Kaunisto, K.; Barreca, D.; Carraro, G.; Gasparotto, A.; Maccato, C.; Bontempi, E.; Sada, C.; Ruoko, T. -.; Turner, S.; Van Tendeloo, G. Vapor Phase Processing of α-Fe_2O_3 Photoelectrodes for Water Splitting: An Insight into the Structure/Property Interplay. *ACS Appl. Mater. Interfaces* **2015**, *7*, 8667-8676.

(21) Warwick, M. E. A.; Carraro, G.; Gasparotto, A.; Maccato, C.; Barreca, D.; Sada, C.; Bontempi, E.; Gönüllü, Y.; Mathur, S. Interplay of Thickness and Photoelectrochemical Properties in Nanostructured α-Fe_2O_3 Thin Films. *Phys. Status Solidi A Appl. Mater. Sci.* **2015**, 1501-1507.

(22) Sivula, K.; Zboril, R.; Le Formal, F.; Robert, R.; Weidenkaff, A.; Tucek, J.; Frydrych, J.; Grätzel, M. Photoelectrochemical Water Splitting with Mesoporous Hematite Prepared by a Solution-Based Colloidal Approach. *J. Am. Chem. Soc.* **2010**, *132*, 7436-7444.

(23) Steier, L.; Herraiz-Cardona, I.; Gimenez, S.; Fabregat-Santiago, F.; Bisquert, J.; Tilley, S. D.; Grätzel, M. Understanding the Role of Underlayers and Overlayers in Thin Film Hematite Photoanodes. *Adv. Funct. Mater.* **2014**, *24*, 7681-7688.

(24) Upul Wijayantha, K. G.; Saremi-Yarahmadi, S.; Peter, L. M. Kinetics of Oxygen Evolution at α-Fe_2O_3 Photoanodes: A Study by Photoelectrochemical Impedance Spectroscopy. *Phys. Chem. Chem. Phys.* **2011**, *13*, 5264-5270.

CHAPTER 4

PLASMONIC ENHANCEMENT OF PHOTOACTIVITY BY GOLD NANOPARTICLES EMBEDDED IN HEMATITE FILMS

4.1 Surface plasmon resonance

Surface plasmon resonance (SPR) is the collective oscillation of conduction electrons in metallic nanostructures induced by an electromagnetic field of light. The phenomenon of SPR imparts distinct color to the nanoparticles depending on its shape, size and the surrounding media. A simplified explanation of the SPR phenomenon can be offered by considering the conduction electrons in a metal nanoparticles oscillating against the restorative force of positive ionic cores. When the frequency of incident electromagnetic radiation matches with the frequency of the electron cloud, the phenomenon is known as surface plasmon resonance. The oscillation of electrons also causes an increase in kinetic and electrostatic energies associated with electric dipoles; this energy is lost in the form of light and heat energy. In addition to absorption, metal nanoparticles can scatter light changing the propagation direction, energy and momentum. The resonant frequency and wavelength is dependent on the nature, shape and size of the metal nanoparticle (figure 4.1).[1, 2] It can also be modified by the dielectric constant of the surrounding media. The properties such as high absorption coefficient, concentrate, amplify and manipulate

light at the nanoscale through SPR have been used for several practical applications such as biomedicine, solar cells, photocatalysis, etc.[3-5]

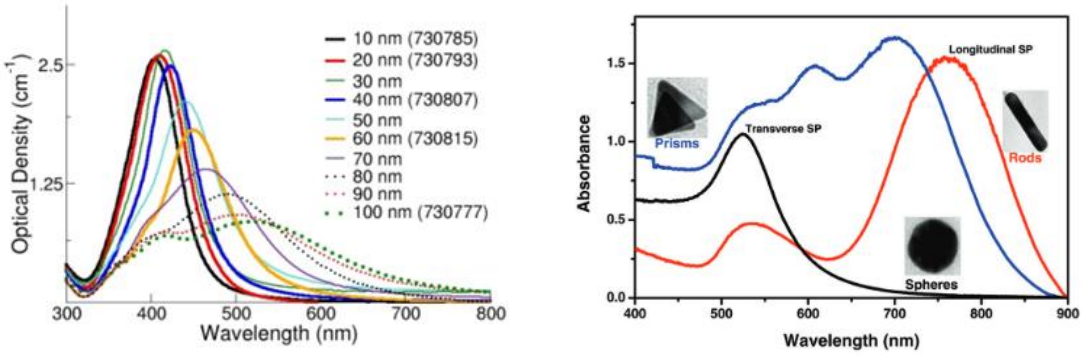

Figure 4.1: (a) Size-dependent absorption spectrum of Ag nanoparticles ranging from size 10 - 100 nm. (b) Shape dependent absorption properties of Au nanostructers. Figure reproduced with permission from Ref. 1 and 2. Copyrights 2014 and 2015 Royal Society of Chemistry.

Nanostructures of metals such as Au, Ag, and Cu are well known to exhibit localized surface plasmon resonance (LSPR) characteristics under visible light. These nanostructures have shown capabilities of enhancing the PEC water splitting efficiency by enhancing the absorption cross-section and photon penetration depth of a metal oxide semiconductor.[3, 6, 7] Three mechanisms have been proposed for this enhancement.[8] The first mechanism involves a direct electron transfer from plasmonic structure to semiconductor valence band when the plasmonic structure is placed on top of the semiconductor. Charge transfer is expected in such a top configuration when the plasmonic structure is in intimate contact with the underlying semiconductor surface.[3] A drawback of such a configuration is the electrochemical corrosion of the plasmonic structure in aqueous solution, and electron back transfer from semiconductor to the metallic NPs due to Fermi level equilibration occurring upon light absorption of the semiconductor.[9] Nevertheless, plasmonic

metal NPs can help impart visible light activity to the semiconductor in a top configuration when the semiconductor-metal nanocomposite is irradiated with visible light.[10] The second mechanism involves the interaction of semiconductor with LSPR-enhanced local electromagnetic field, which enhances the light absorption cross section of a semiconductor layer and results in enhanced population of e^-–h^+ pairs in the semiconductor.[8] The third mechanism is based on efficient scattering mediated by LSPR (far-field effect), which leads to longer optical path lengths for photons in the semiconductor that increase the number of e^-–h^+ pairs. The second and third mechanisms are observed in the embedded configuration, wherein the plasmonic NPs are embedded in a metal oxide layer.[11] A comparative study of surface and embedded configuration of spherical Au NPs with hematite by Warren *et al* reveals an overall photocurrent increase in the embedded system and a visible light photoactivity in the surface configuration due to the spectral overlap of absorption of Au NPs and hematite catalyst.[12] However, there is no systematic study of hematite film thickness dependence of the photocurrent and no mention regarding the background current generated from the exposed metallic surface.

N-type hematite (α-Fe_2O_3) is one of the most promising metal oxide semiconductor (MOS) catalysts for solar water oxidation[13]. A serious issue pertaining to hematite photoanodes is the poor photon penetration depth (~118 nm at λ=550 nm)[14] in spite of its visible light absorption over a wide wavelength range (300-500 nm).[15, 16] Thus, hematite thickness is limited to < 100 nm for water splitting due to its poor absorptivity and short hole diffusion length. We have studied an improved embedded configuration of electrodeposited Au NPs coated with a smooth hematite photocatalyst layer for water oxidation. The Au NPs are isolated from the conductive FTO electrode surface by a thin layer of TiO_2. The improved embedded configuration has the advantage of consistent protection and performance of plasmonic nanostructure for long cycles of operation

and enhancing light absorption of the hematite film. Chemical vapor deposition (CVD) is used to deposit the high quality crystalline hematite layer. The process involves direct decomposition of precursor vapors on a heated substrate producing smooth, uniform and highly crystalline hematite films. We observe a nearly three-fold increase in light scattering efficiency and photocurrent enhancement in thin hematite films embedded with Au NPs. For a given thickness of hematite the plasmonic enhancement increases with the density of Au NPs. Thickness- dependent plasmonic activity studies show photocurrent enhancement in films as thick as 650 nm.

4.2. Experimental

Figure 4.2 shows the schematic of the hematite electrodes prepared using CVD technique with embedded Au NPs on TiO_2 coated FTO substrate. Detailed conditions used for substrate preparation and hematite film coating are described below.

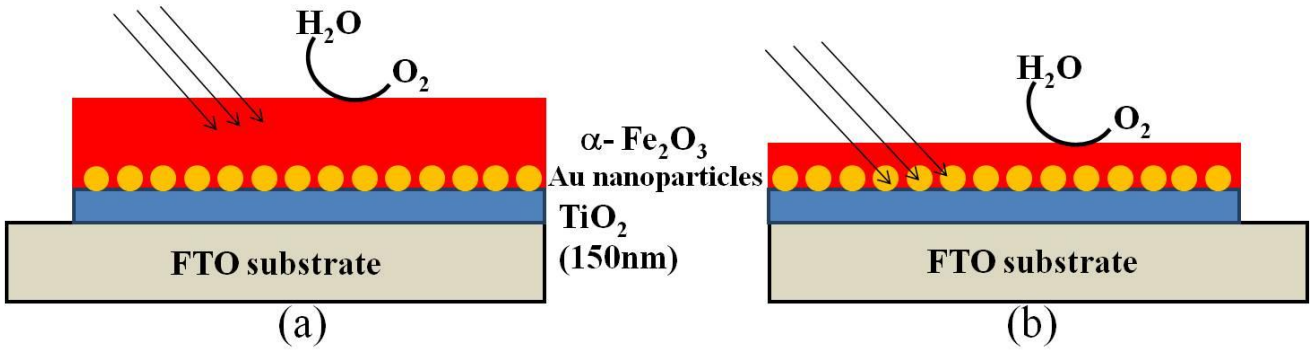

Figure 4.2: Schematic of hematite electrode grown by CVD technique on TiO_2 coated FTO substrate with embedded Au nanoparticles. (a) Thick and (b) thin hematite film.

4.2.1 FTO substrate cleaning and TiO_2 layer coating

FTO coated glass substrates (1.5 cm × 1 cm; 25 Ω/□, Pilikington Glass Co. Ltd., U.S.A) were cleaned using detergent followed by washing with copious amount of DI water prior to being ultrasonically cleaned in acetone and isopropanol, each for 30 min. A polymeric titania sol was

prepared by dissolving polyvinylpyrrolidone (0.3 g, PVP, MW ~ 180,000) in ethanol (3.5 ml) followed by drop-wise addition of titanium isopropoxide (0.5 g) and acetic acid (1ml). The titania sol was spin-coated onto the cleaned FTO glass at 3500 rpm for 30 seconds. The titania coated FTO plates were then annealed in air at 500 ^{o}C in a box furnace for 30 minutes and cooled to room temperature to produce a ~100 nm thick TiO_2 layer. The TiO_2 layer was used to reduce the surface roughness of FTO and minimize the background current of the top hematite layer by preventing Au NPs from direct contact with the FTO surface.

4.2.2 Electrodeposition of Au NPs

Au NPs were electrodeposited on the TiO_2 coated substrates using a three-electrode cell containing Pt wire counter electrode and an Ag/AgCl reference electrode. As-received Orotemp 24 (Pottasium cyanoaurate, 6.87%) Au plating solution (Technic Inc, Cranston, Rhode Island, U.S.A) was diluted five times with DI water for Au NP deposition on TiO_2 coated FTO. Cyclic voltammetric scans from 0.3 V to -1.5 V (vs. Ag/AgCl) at a scan rate of 50 mV/s was used for electrodeposition. Different nanoparticles densities were obtained by varying the number of cyclic voltammetric scans on the FTO substrate. The electrodeposited Au NPs were characterized by scanning electron microscopy (SEM; JEOL 7000, USA).

4.2.3 Deposition of hematite films

Direct liquid injection chemical vapor deposition (DLI-CVD) technique was used for the deposition of α-Fe_2O_3 on Au NP coated substrates. Thickness of the deposited films was varied by diluting the precursor concentration and/or varying the deposition times from 15, 30, 45, 60, 75 and 90 minutes.

4.2.4. Structural and photoelectrochemical characterizations

The absorption characteristics of the films were recorded with a UV-Visible spectrophotometer (Agilent, Cary 500, USA). X-ray diffraction (XRD) patterns of the samples were measured by an X-ray diffractometer (XRD, Bruker D8) employing CoKα radiation. The water splitting characteristics of the films were studied by recording I-V characteristics in a three-electrode cell configuration consisting of platinum wire and Ag/AgCl (saturated with KCl) as counter and reference electrodes, respectively, in 0.5 M NaOH. The electrode potential was scanned from -0.5 to 1.8 V using a potentiostat (Princeton EG&G Applied Research) and the corresponding current was recorded. The measurements were performed in dark and under light using a Xe arc lamp at AM 1.5G conditions. Action spectra of the electrodes were recorded in 0.5 M NaOH by measuring the current response while holding the potential constant at 0.6 V (vs. Ag/AgCl) using a CHI 760 potentiostat (CH Instruments, Inc., Austin, TX**)**. Monochromatic light from 300 to 750 nm was achieved from a monochromator (MD 1000, Optical Building Blocks) with white light input from a Xe arc lamp. Current vs. time graphs were recorded with the potentiostat and the time scale was then converted to wavelength scale to obtain the action spectra characteristics. The action spectra were converted to incident photon conversion efficiency (IPCE) using equation 1,

$$IPCE(\%) = \frac{1240 \times I(mA/cm^2)}{\lambda(nm) \times P_{inc}(mW/cm^2)} \times 100. \quad \text{Equation (1)}$$

Electrochemical impedance spectra of the electrodes in three-electrode configuration were recorded under dark and light conditions using a CHI760 bipotentiostat (CH Instruments, Inc., Austin, TX**)** in the 0.1 Hz-10 KHz frequency range from a voltage range of -0.2 to 0.7 V (vs. Ag/AgCl).

4.3. Results and discussions

4.3.1. Morphological and structural characterizations

We prepared three different electrodes for a given thickness of hematite by varying the CVD deposition time. The first had no embedded Au NPs and was used as a control, the second and third had two different Au NP densities. The different Au NP densities was achieved by varying the number of electrodeposition cycles. Figure 4.3 a shows the cyclic voltammogram (CV) of TiO_2-coated FTO electrode in diluted Orotemp solution. The $[Au(CN)_2]^-$ ion reduction occurs at -1.5V vs. Ag/AgCl on TiO_2 coated FTO. Average Au NP densities determined from SEM images are Au1=4×10^9 ($\pm$ 1×10^9) and Au2= $9\times10^9/cm^2$ ($\pm$ 1×10^9) for particles shown in figure 4.3 c and d, obtained after 2 and 4 cycles of CV at 50 mV/sec, respectively. Histogram of the Au NPs size (figure 4.3 c and d insets) show the average particle size to be in the range of 70-80 nm. Small variations in the NP densities from sample to sample under nominally the same electrochemical deposition conditions were observed due to differences in the substrate surface roughness.

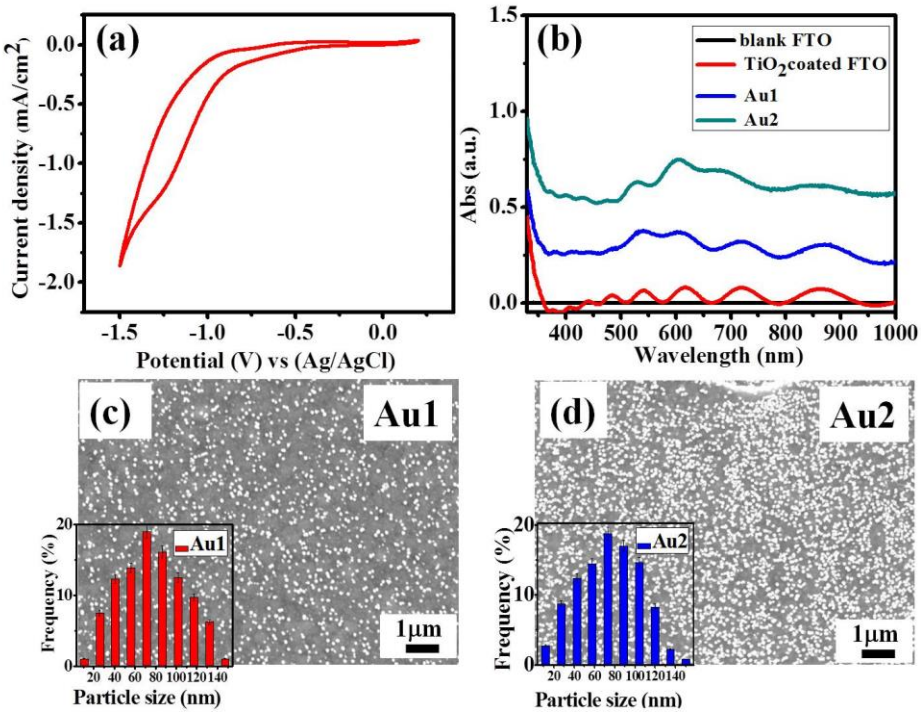

Figure 4.3: (a) Cyclic voltammogram of TiO_2 coated FTO in (1:5) diluted Orotemp Au solution in water at a scan rate of (50 mV/s) (b) U.V- vis absorption characteristics of Au NPs deposited on TiO_2 coated FTO, Au1 corresponds to image (c) and Au2 corresponds to image (d) Spectrum appears wavy due to the interference from the TiO_2 layer on FTO. SEM images of electrodeposited Au NPs on FTO for 2 and 4 cycles of cyclic voltammogram; (c) and (d), respectively. (Number densities: Au1=4×10^9 and Au2= $9\times10^9/cm^2$). Insets in (c) and (d) show the nanoparticle size distribution histograms. The average particle size is ~75 nm.

X-ray diffraction characteristics of the CVD grown films (figure 4.4a) at 500 ^oC show well-defined hematite peaks indicating that this is a suitable growth temperature for the films. Deposition at temperatures lower than 500 ^oC yielded amorphous Fe_2O_3. Hematite film thicknesses have been measured by imaging their cross-sections with SEM. The thickness is found to increase with deposition time as shown in figure 4.4 b. Representative SEM images of cross-sections are shown in figure 4.4 c and 4.4 d. The CVD grown samples are designated as H50, H70, H110, H170, H350 and H650, where the last digits indicate the film thickness in nm. SEM images of the

Au NPs films are recorded before and after deposition of hematite. It should be noted that the average size and shape of Au NPs remain intact even after exposure to temperatures as high as 500ºC. From 45 minutes CVD deposition time (hematite film thickness = 110 nm, Au NP size ~ 75 nm) onwards the Au NPs are completely covered with hematite and are not visible in the SEM imaging (figure 4.5).

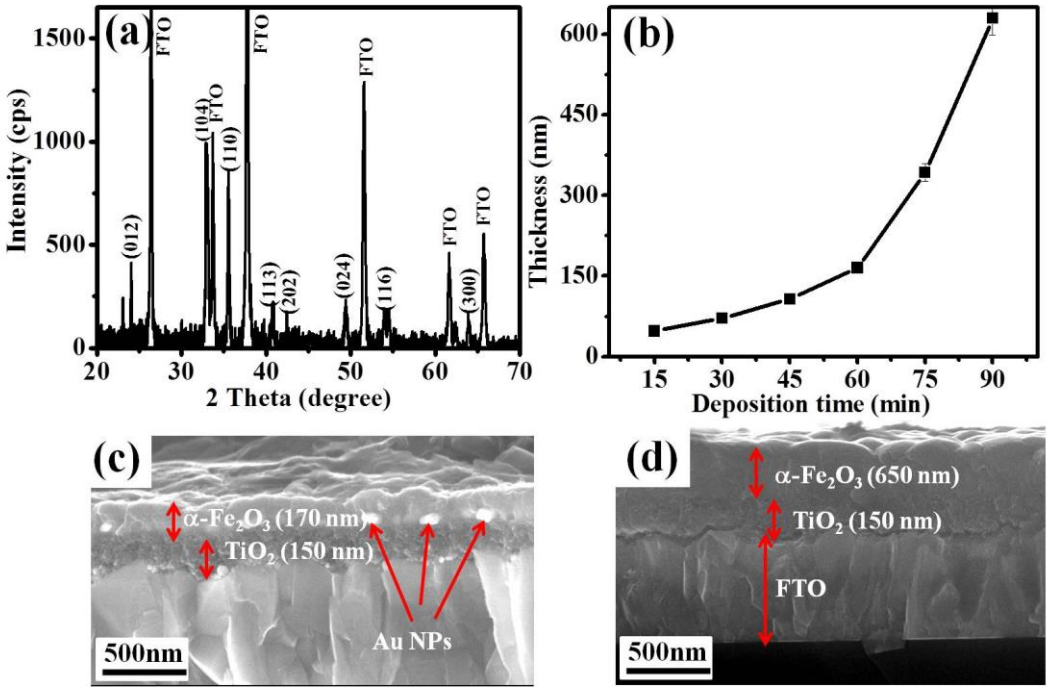

Figure 4.4: (a) XRD pattern of hematite films, (b) Thickness of CVD grown hematite films with increasing deposition time. (c), (d) Cross section SEM images of CVD grown films for 60 minutes (170 nm) (c) and 90 minutes (650nm) (d), respectively. (c) Shows the Au NPs embedded in hematite film.

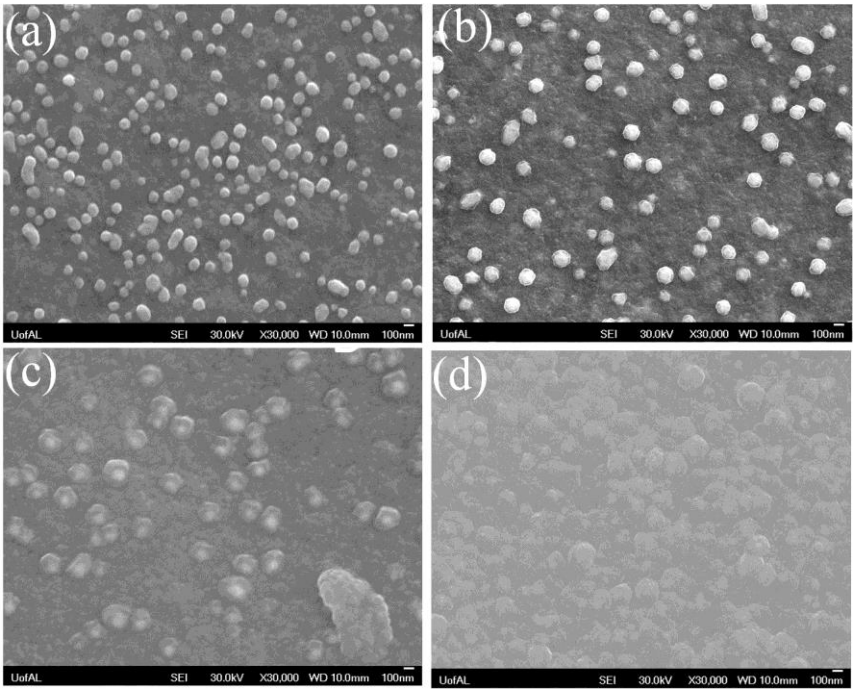

Figure 4.5: SEM images of Au NPs. (a) As deposited on TiO_2 coated FTO and after deposition of hematite of thickness (b) 50 nm (c) 70 nm and (d) 110 nm.

4.3.2 Optical characteristics:

The absorption and transmittance spectra are influenced by optical interference effects from the TiO_2 layer on FTO. Figure 4.3 b shows the absorption spectrum of Au NPs on TiO_2 coated FTO with a plasmonic resonance peak at 600 nm, which is comparable to the reported value of 640 nm for Au NP size of ~70 nm on ITO substrate by Sakai et.al.[17] The plasmon absorption peak wavelength is not affected with the increase in Au NPs coverage (Au2) as the particle size distribution remains unaltered.[18] However, light absorption and scattering effects in Au NPs films, which depend on the spacing between the NPs is observed to increase with increasing coverage.[17] Figure 4.6 shows the absorption and transmittance spectra of the hematite films with and without Au NPs. The absorption and transmittance spectra are accompanied with optical interference effects from the underlying TiO_2 layer and FTO. Absorbance in the region of 300-600 nm is from

both the hematite film and Au NPs and the additional peak around 600-700nm is due to Au NP surface plasmon absorption. As expected, the absorbance due to hematite increases with film thickness. The plasmonic peak also increases in intensity with increasing surface coverage of Au NPs. This effect is more pronounced in the transmittance spectra of the samples, wherein a decrease in transmittance with increasing film thickness and Au NP coverage is observed. For example, the transmittance of 110 nm hematite film (H110), which is 80% at 600 nm, is reduced to 40% for a similar thickness hematite film containing Au NPs (Au1H110) and further decreased to 20% for a 110 nm film containing more Au NPs (Au2H110). In fact, this value of transmittance is similar to that of a bare 650 nm hematite film. Such increased light absorption in the plasmon region in the presence of Au NPs is expected to localize the incident light intensity to help increase the light absorbed by the hematite layer in this wavelength region. The surface plasmon peak of Au NPs shows a red shift from 575 to 600-700 with increasing hematite thickness. Such a red shift is associated with weakened oscillator strength of plasmon resonance in the presence of a high dielectric constant material in the embedded configuration.[12] The scattering of light in thicker films causes the absorption onset of the samples to shift to longer wavelengths as seen by comparing the spectra of bare 70 nm hematite film (H70) and 110 nm film (H110). This observation is consistent with the Au NPs films coated hematite.

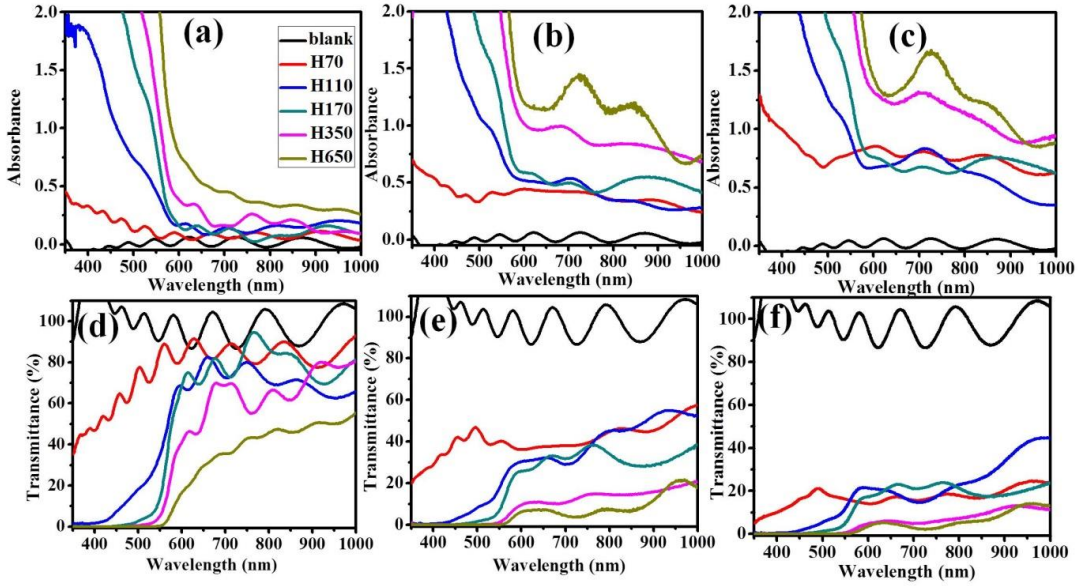

Figure 4.6: Top panel graphs show the UV-Vis absorption characteristics and bottom panel show transmittance characteristics of different hematite films. (a) Hematite films with varying thickness, (b) various thickness hematite coated Au1 films, (c) various thickness hematite coated Au2 films. (d), (e), (f) Corresponding transmittance spectra. (Number densities: Au1=4×10^9 and Au2= $9\times10^9/cm^2$)

4.3.3 Current-voltage (I-V) characteristics

The PEC water splitting performance of hematite and Au modified hematite electrodes have been tested by recording the current - voltage (I-V) characteristics in the dark and under irradiation conditions. Overall enhancement in the photocurrent density is observed in all the Au NP modified hematite films as compared to bare hematite films. For thinner hematite films embedded with Au NPs, the I-V curves show electrochemical oxidation peaks of Au NPs (figure 4.7), indicating that the Au NPs are not completely covered with hematite. Such oxidation peaks are not observed for 15 min (50 nm) and 30 min (70 nm) hematite films in the absence of Au NPs. This indicates that the growth of thinner hematite films on 100 nm Au NPs is not conformal. From a deposition time of 45 minutes (thickness =110 nm) onwards, a complete coating on the Au NPs is obtained, hence no background current or Au oxidation peaks are observed in the I-V graphs

(figure 4.8). Photocurrent in pure hematite films increased with thickness because of increase in optical density and improved crystallinity of hematite films over extended period of treatment at high temperature in the CVD reactor.

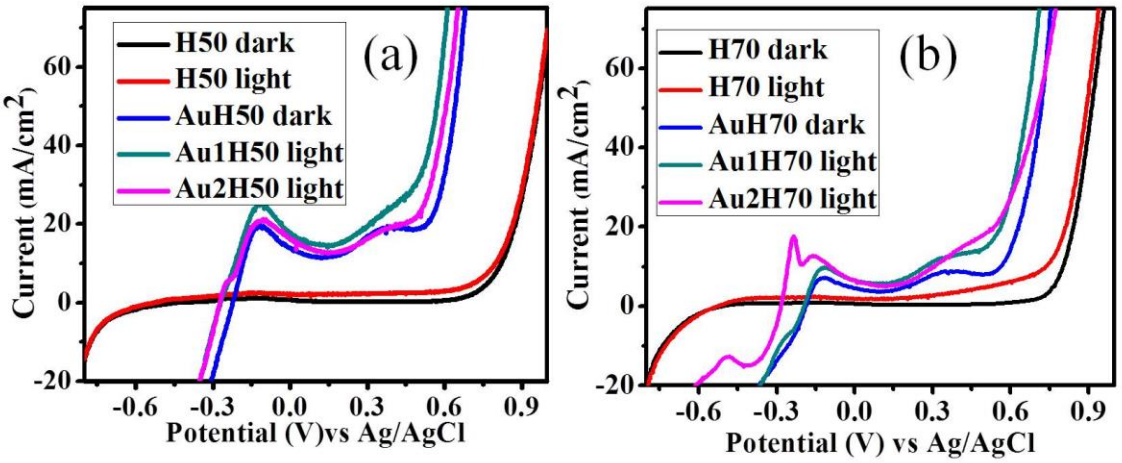

Figure 4.7: Current-voltage (I-V) characteristics of CVD hematite films for (a) 15 minutes growth: hematite film thickness=50 nm, (b) 30 minutes growth: hematite film thickness=70 nm. (Number densities: Au1=4×10^9 and Au2= $9\times10^9/cm^2$)

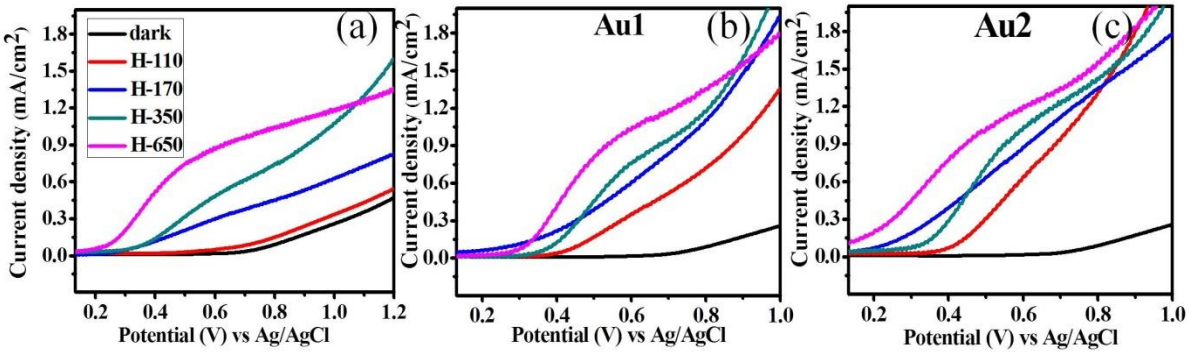

Figure 4.8: Current-voltage (I-V) characteristics of hematite deposited films. (a) Hematite films deposited on TiO_2 coated FTO at different times. The numbers indicate the thickness of the films. (b) Au1 deposited hematite and (c) Au2 deposited hematite. (Number densities: Au1=4×10^9, Au2= $9\times10^9/cm^2$)

4.3.4 Incident photon conversion efficiency characteristics

Incident photocurrent conversion efficiency (IPCE) of the hematite electrodes is shown in figure 4.9 to determine the photoactive wavelength range of the electrodes. The IPCE is observed to follow a similar trend to that of the UV-Vis absorption characteristics of the electrodes. IPCE curves do not show any dominant peaks at the surface plasmon absorption region above 600 nm for Au NP modified hematite samples, indicating that no direct electron injection from the Au NPs to hematite occurs in the embedded configuration. The improved IPCE below 600 nm is attributed to significant improvement of PEC effect by Au NPs, with local-field enhanced light absorption cross-section of hematite likely playing a role. Other mechanisms such as improved hematite film conductivity for charge collection and change in the electronic structure of hematite film on Au NPs may also contribute to the enhancement. Carrier dynamics and transient spectroscopy measurements are ongoing to help understand these contributing factors. By assuming no changes in electronic structure and charge transfer distances in hematite layer on Au NPs, plasmon absorption-induced field enhancement effect should play a major role in generating an enhanced population of e^--h^+ pairs in the Au modified hematite layer. The IPCE peaks show a red shift with increase in Au NP coverage (figure 4.9 b and c) indicating that absorption enhancement does play a role. More quantitative analysis cannot be achieved without detailed understanding of the changes in both electronic structure and charge transport capability in hematite film grown on Au NPs.

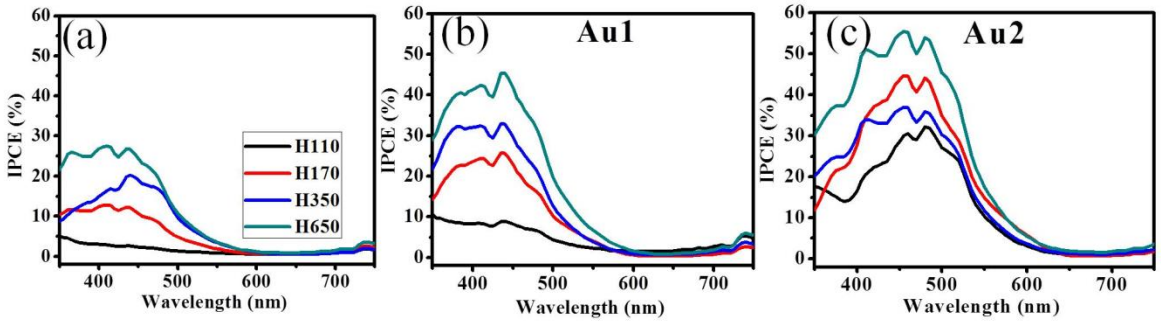

Figure 4.9: IPCE characteristics of hematite deposited films. (a) Hematite films deposited on TiO_2 coated FTO at different times. The parenthesis indicates the thickness of the films. (b) Au1 deposited hematite and (c) Au2 deposited hematite. Potential of the electrodes were maintained at 0.6 V vs. Ag/AgCl. (Number densities: Au1=4×10^9 and Au2= $9\times10^9/cm^2$)

Figure 4.10(a) shows the absorbance at 700 nm as a function of the film thickness. As discussed earlier, an overall increase in absorption with Au NPs is observed. Figure 4.10(b) shows a plot of photocurrents at 0.6V vs. Ag/AgCl under 1 Sun irradiation as a function of thickness of the hematite layer. Enhanced photocurrents are observed with increasing Au NP density and hematite film thickness. Photocurrent enhancement factor in Au NPs coated hematite, calculated by normalizing the photocurrent w.r.t the corresponding hematite thickness and Au NP density (figure 4.10c and d), shows a decreasing trend. This can be explained by the light penetration depth in different thickness hematite samples in the presence and absence of Au NPs. Figure 4.11 shows a schematic representation of three different thicknesses of hematite films (650 nm, 350 nm and 110 nm) with embedded Au NPs prepared by CVD technique. The depletion width (w) of a metal oxide electrode is defined as the band bending at the electrode-electrolyte interface and is a thickness dependent parameter: a greater thickness of the film implies increased charge transfer across the interface. Excitons generated in the film migrate towards the surface and separation occurs in the depletion region to form charge carriers for the water splitting reaction. The depletion

width is crucial to the performance of the photocatalytic film. As the thickness of the films increases, higher number of charges diffuse to form a thicker depletion layer. In the 110 nm hematite electrode modified with Au NPs, a greater number of charges are generated on irradiation due to plasmonic light scattering, thus increasing the width of depletion layer. The width of the depletion layer in a thick hematite film (650 nm) will be the same in a thin film with plasmonic light scattering due to the enhancement in absorption by Au NPs, which explains the similar photocurrent in Au NPs incorporated hematite film of thickness 110 nm with that of pure hematite film of thickness 650 nm. As the thickness of the hematite increases, most of the light is absorbed in the thick hematite layer, leaving no photons to interact with the plasmonic Au NPs. Thus thin hematite films of 100-200 nm are ideal for providing optimal plasmon-hematite interaction for the charge carrier population for PEC reaction.

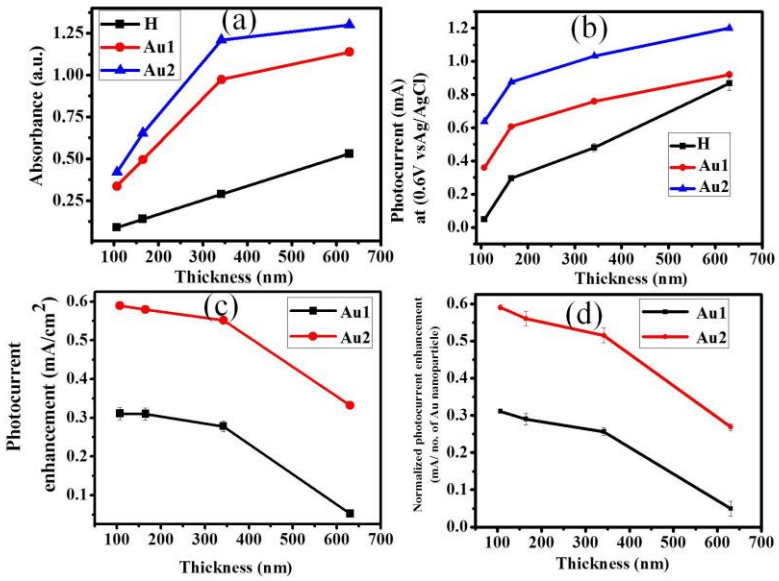

Figure 4.10: Increasing trend in (a) absorbance and (b) photocurrent at 0.6 V vs. Ag/AgCl in hematite films with increased number density of Au NP for increasing thickness of films. (c) Decreasing trend of photocurrent enhancement in Au incorporated hematite films with increasing trend. (d) Normalized photocurrent enhancements w.r.t Au NP number density at hematite film of 110 nm. (Number densities: Au1=4×10^9, Au2= 9×10^9/cm^2).

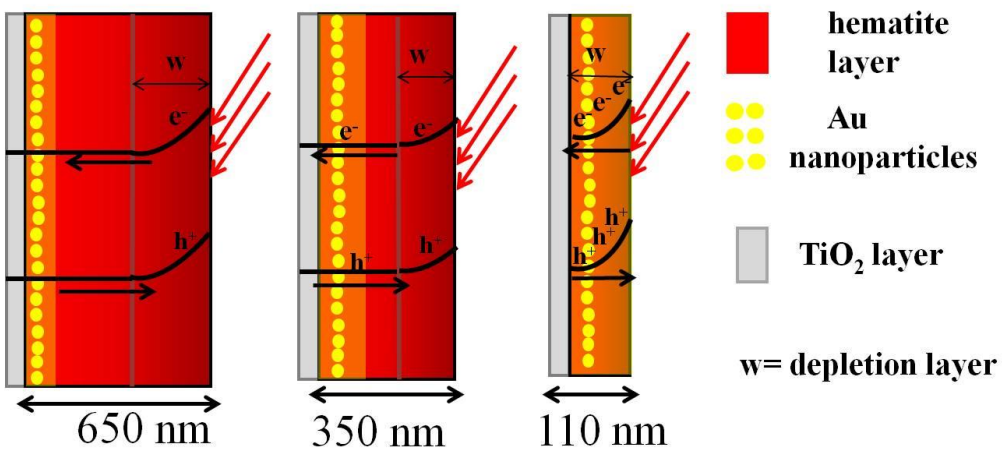

Figure 4.11: Schematic representation of the hematite thickness shielding effect in different thickness hematite films.

4.3.5 Mott-Schottky plots and electrochemical impedance spectroscopy studies

To support the hypothesis regarding the number of carriers in the hematite films, we performed Mott-Schottky analysis on selective hematite electrodes, namely electrodes with thickness of 110 and 650 nm and with Au NPs with number density $9\times10^9/cm^2$ (Au2). Capacitance (C) of the samples are calculated from the imaginary component Z" of the impedance spectra by the equation $Z" = \frac{1}{2\pi f C}$. Mott-Schottky plots of the samples are obtained by plotting ($1/C^2$) vs. the potential (V vs Ag/AgCl) values in the dark (figure 4.12). The plots are fitted to a straight line and the slopes are used to calculate the carrier densities using equation 1;

$$\frac{1}{C^2} = \frac{2}{A^2 q \varepsilon \varepsilon_0 N_D}\left(V - V_{fb} - \frac{kT}{q}\right) \quad (2)$$

where A=area of the film, q is the elementary charge, ε_0 is the permittivity of free space, ε is the dielectric constant of the hematite (ε=80, for hematite[19]), *k* is the Boltzmann constant and T is the absolute temperature of the system. The carrier densities in the films increase with increasing

thickness of hematite and with incorporation of Au NPs in the hematite. Total number of carriers in the 110 nm hematite film (H110) increased from $1.03\times10^{15}/cm^2$ to $1.95\times10^{18}/cm^2$ by the introduction of Au NPs. This value is of the same order as that of a bare 650 nm hematite, which has a carrier density of $8.70\times10^{17}/cm^2$. However, the increase in the carrier density in Au modified 650 nm hematite electrode ($1.17\times10^{18}/cm^2$) is observed as compared to bare 650 nm hematite film. These results are in accordance with the measured photocurrent densities by I-V characteristics. The calculated carrier densities are lower compared to the reported values of ~10^{20}- 10^{22} in mesoporous and cauliflower-like structures due to the planar and compact nature of the films and possibly lower defects[20].

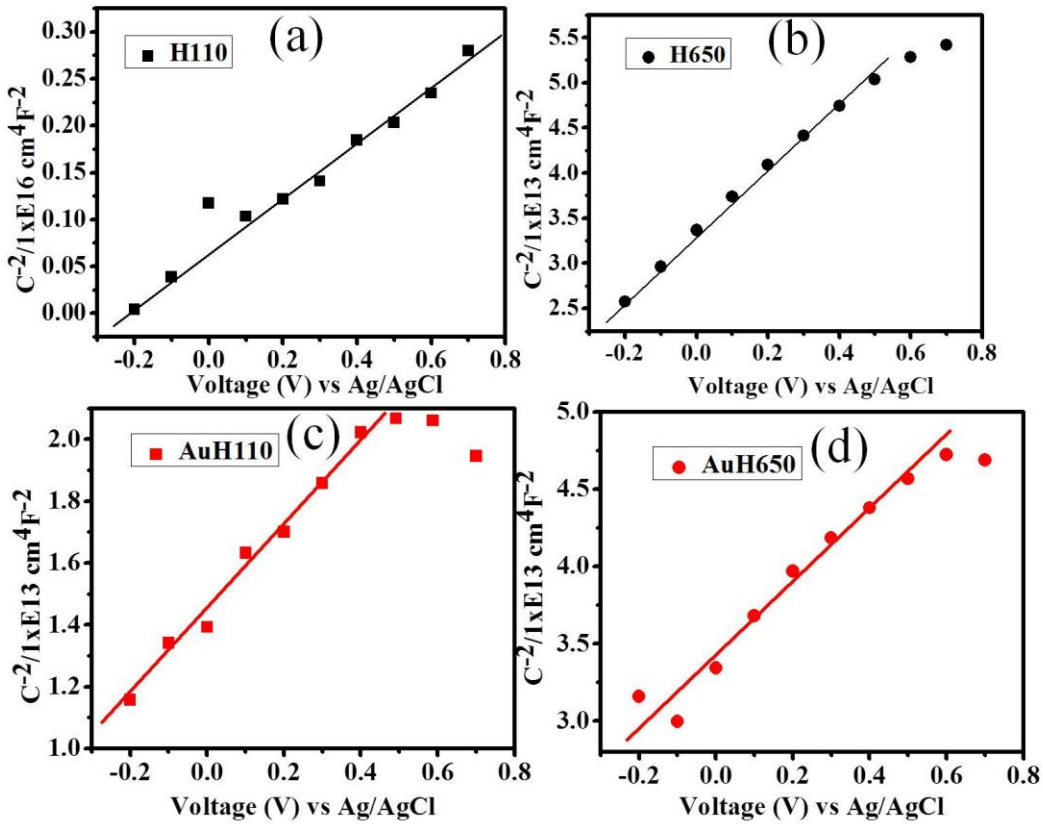

Figure 4.12: Mott-Schottky plots of selected hematite electrodes (a) H110, (b) H650, (c) AuH110, and (d) AuH650 (Number density : Au2= $9\times10^9/cm^2$)

Figure 4.13 shows the Nyquist plots of the hematite films with thicknesses of 110 nm and 650 nm with and in the absence of Au NPs at 0.7V vs Ag/AgCl in dark and light, respectively. An equivalent circuit shown in figure 4.13 (e) is applied to fit the Nyquist plots of the electrodes at 0.7V in dark and at 1 Sun illumination conditions. Table 1 shows the statistics of extracted parameters. Variation in R_s values from 50 to 90 Ω are observed due to the variations in FTO substrate resistance. The double layer charging capacitance of the solid-liquid junction (C_{SC}) of the electrodes are approximately constant. The charge transfer resistance (Rct) values of the electrodes are lower under irradiation conditions compared to the dark due to the photo-induced charge transfer events. The trap state capacitances (C_{trap}) of the Au embedded electrode (Au2H110, Au2H650) are higher compared to that of hematite electrodes (H110, H650) in the hematite film C_{trap} indicating greater bumber of holes could be stored in the intermediate states, facilitating the participation of the holes in the photocurrent conversion processes. The decrease of R_{ct}, and R_{trap} indicates increased charge carriers in the film facilitate charge transfer of holes to the donor species in solution and suppress the recombination of photogenerated electron−hole pairs, and improve the photocurrent.[21] A higher value of C_{trap} also indicates a higher number of trap states being filled in the hematite film resulting in increased carrier density.

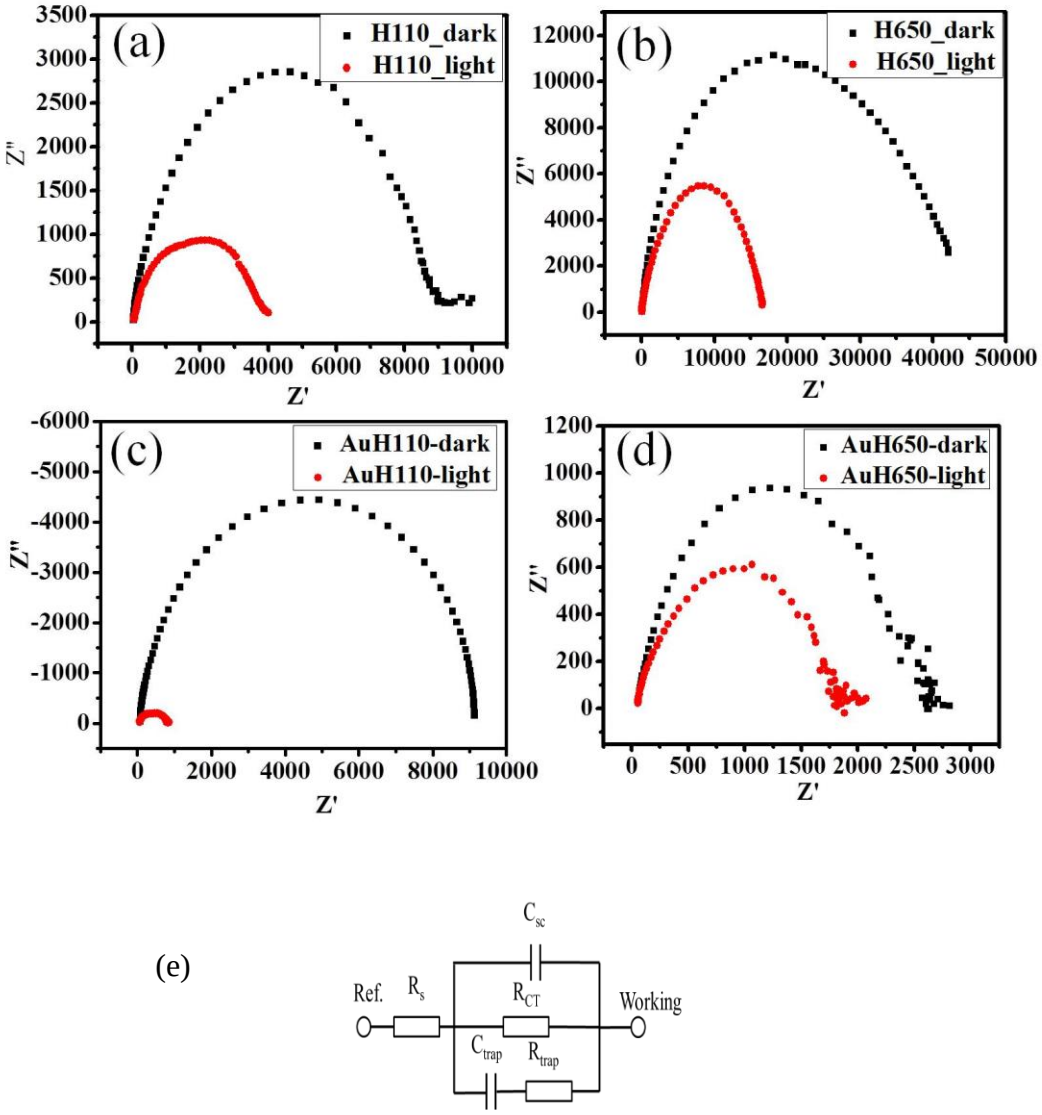

Figure 4.13: Nyquist plots of hematite electrodes at 0.7 V (vs Ag/AgCl) in dark (black squares) and in light (red circles) measured in a frequency range of 0.1Hz to 10,000Hz. (a) H110, (b) Au2H110, (c) H650, (d) Au2H650. (e) Equivalent circuit used to fit the Nyquist plots. (Number density: Au2= $9\times10^9/cm^2$).

		R_s (Ω)	C_{sc} (μF)	R_{ct} (Ω)	C_{trap} (μF)	R_{trap} (Ω)
Dark	**H110**	52.18(2.09)	0.829 (0.017)	7997(160)	1.36 (0.10)	3256(260)
	HAu110	74.18 (2.97)	1.52(0.046)	3146(63)	4.75(0.38)	1510(105)
	H650	70.65 (3.53)	0.725(0.022)	29536(886)	1.15(0.07)	5209(468)
	HAu650	66.94(2.68)	0.734(0.015)	14183(283)	1.54(0.06)	2576(154)
Light	**H110**	77(2)	2.49(0.12)	9059(272)	0.426(0.021)	8255(330)
	HAu110	60.4(1.8)	1.77(0.07)	715.9(14.3)	6.24(0.62)	557.7(44.6)
	H650	90.05(5.40)	0.131(0.003)	2460(25)	0.103(0.009)	2973(357)
	HAu650	56.91(1.71)	0.855(0.017)	1681(17)	1.32(0.07)	771.4(54.0)

Table 4.1: Experimental fit parameters along with their fitting errors obtained from fitting Nyquist plots using equivalent circuit shown in figure 4.13 (e).

4.4 Conclusions

High quality hematite PEC electrodes embedded with Au NPs have been developed to demonstrate the plasmonic enhancement effect. Different thickness hematite films (110 to 650 nm) are grown on TiO_2 coated FTO substrates via direct liquid injection chemical vapor deposition

technique. Plasmonic Au NPs embedded in hematite films increases the absorbance in hematite films by plasmonic light concentration and scattering effects of Au surface plasmon resonance. The increased absorption leads to a higher number of charge carriers in the film and hence higher water oxidation capability. Au nanoparticle films with thin hematite coating (110 nm) show a greater enhancement in photocatalytic activity compared to a thick hematite film with Au NPs due to the greater interaction of Au NPs with light, generating higher number of charge carriers in the film. Mott-Schottky plots indicate an enhancement in charge carrier density of thin hematite film by incorporation of Au NPs. Electrochemical impedance spectroscopy data show a lower value for charge transfer resistance in Au NP embedded films indicating improved carrier transport and/or an efficient water oxidation kinetics at the surface. A drawback of the current electrode system is that complete conformal coating of hematite on the Au NPs is not obtained by CVD technique and a minimum hematite thickness of 110 nm is required to prevent the electrochemical corrosion of Au NPs. This can be overcome by optimizing our CVD conditions and following surface passivation of exposed Au NPs surface in our future work. An enhanced rate of water oxidation on the surface of hematite can likely be achieved by conformal coating by taking maximum advantage of the SPR of Au NPs.

4.5 References

(1) Paramelle, D.; Sadovoy, A.; Gorelik, S.; Free, P.; Hobley, J.; Fernig, D. G. A Rapid Method to Estimate the Concentration of Citrate Capped Silver Nanoparticles from UV-Visible Light Spectra. *Analyst* **2014**, *139*, 4855-4861.

(2) Attia, Y. A.; Buceta, D.; Requejo, F. G.; Giovanetti, L. J.; López-Quintela, M. A. Photostability of Gold Nanoparticles with Different Shapes: The Role of Ag Clusters. *Nanoscale* **2015**, *7*, 11273-11279.

(3) M, A. G. Surface Plasmons in Metallic Nanoparticles: Fundamentals and Applications. *J. Phys. D* **2011**, *44*, 283001.

(4) El-Sayed, M. A. Some Interesting Properties of Metals Confined in Time and Nanometer Space of Different Shapes. *Acc. Chem. Res.* **2001**, *34*, 257-264.

(5) Kelly, K. L.; Coronado, E.; Zhao, L. L.; Schatz, G. C. The Optical Properties of Metal Nanoparticles: The Influence of Size, Shape, and Dielectric Environment. *J Phys Chem B* **2003**, *107*, 668-677.

(6) Abe, R. Recent Progress on Photocatalytic and Photoelectrochemical Water Splitting Under Visible Light Irradiation. *Journal of Photochemistry and Photobiology C: Photochemistry Reviews* **2010**, *11*, 179-209.

(7) Linic, S.; Christopher, P.; Ingram, D. B. Plasmonic-Metal Nanostructures for Efficient Conversion of Solar to Chemical Energy. *Nat Mater* **2011**, *10*, 911-921.

(8) Zhang, X.; Zhu, Y.; Yang, X.; Wang, S.; Shen, J.; Lin, B.; Li, C. Enhanced Visible Light Photocatalytic Activity of Interlayer-Isolated Triplex $Ag@SiO_2@TiO_2$ Core-Shell Nanoparticles. *Nanoscale* **2013**, *5*, 3359-3366.

(9) Subramanian, V.; Wolf, E. E.; Kamat, P. V. Catalysis with TiO_2/Gold Nanocomposites. Effect of Metal Particle Size on the Fermi Level Equilibration. *J. Am. Chem. Soc.* **2004**, *126*, 4943-4950.

(10) Pu, Y.; Wang, G.; Chang, K.; Ling, Y.; Lin, Y.; Fitzmorris, B. C.; Liu, C.; Lu, X.; Tong, Y.; Zhang, J. Z.; Hsu, Y.; Li, Y. Au Nanostructure-Decorated TiO_2 Nanowires Exhibiting Photoactivity Across Entire UV-Visible Region for Photoelectrochemical Water Splitting. *Nano Lett.* **2013**, *13*, 3817-3823.

(11) Bumajdad, A.; Madkour, M. Understanding the Superior Photocatalytic Activity of Noble Metals Modified Titania Under UV and Visible Light Irradiation. *Physical Chemistry Chemical Physics* **2014**, *16*, 7146-7158.

(12) Thimsen, E.; Le Formal, F.; Grätzel, M.; Warren, S. C. Influence of Plasmonic Au Nanoparticles on the Photoactivity of Fe_2O_3 Electrodes for Water Splitting. *Nano Letters* **2011**, *11*, 35-43.

(13) Bora, D. K.; Braun, A.; Constable, E. C. "In Rust we Trust". Hematite-the Prospective Inorganic Backbone for Artificial Photosynthesis. *Energy and Environmental Science* **2013**, *6*, 407-425.

(14) Itoh, K.; Bockris, J. O. Thin Film Photoelectrochemistry: Iron Oxide. *J. Electrochem. Soc.* **1984**, *131*, 1266-1271.

(15) Glasscock, J. A.; Barnes, P. R. F.; Plumb, I. C.; Bendavid, A.; Martin, P. J. Structural, Optical and Electrical Properties of Undoped Polycrystalline Hematite Thin Films Produced using Filtered Arc Deposition. *Thin Solid Films* **2008**, *516*, 1716-1724.

(16) Al-Kuhaili, M. F.; Saleem, M.; Durrani, S. M. A. Optical Properties of Iron Oxide (α-Fe_2O_3) Thin Films Deposited by the Reactive Evaporation of Iron. *J. Alloys Compounds* **2012**, *521*, 178-182.

(17) Sakai, N.; Fujiwara, Y.; Arai, M.; Yu, K.; Tatsuma, T. Electrodeposition of Gold Nanoparticles on ITO: Control of Morphology and Plasmon Resonance-Based Absorption and Scattering. *J Electroanal Chem* **2009**, *628*, 7-15.

(18) Wang, J.; Wang, L.; Di, J.; Tu, Y. Electrodeposition of Gold Nanoparticles on Indium/Tin Oxide Electrode for Fabrication of a Disposable Hydrogen Peroxide Biosensor. *Talanta* **2009**, *77*, 1454-1459.

(19) Cesar, I.; Sivula, K.; Kay, A.; Zboril, R.; Grätzel, M. Influence of Feature Size, Film Thickness, and Silicon Doping on the Performance of Nanostructured Hematite Photoanodes for Solar Water Splitting. *Journal of Physical Chemistry C* **2009**, *113*, 772-782.

(20) Hiralal, P.; Saremi-Yarahmadi, S.; Bayer, B. C.; Wang, H.; Hofmann, S.; Upul Wijayantha, K. G.; Amaratunga, G. A. J. Nanostructured Hematite Photoelectrochemical Electrodes Prepared by the Low Temperature Thermal Oxidation of Iron. *Solar Energy Mater. Solar Cells* **2011**, *95*, 1819-1825.

(21) Miao, C.; Shi, T.; Xu, G.; Ji, S.; Ye, C. Photocurrent Enhancement for Ti-Doped Fe_2O_3 Thin Film Photoanodes by an in Situ Solid-State Reaction Method. *ACS Appl. Mater. Interfaces* **2013**, *5*, 1310-1316.

CHAPTER 5

SYNTHESIS OF BISMUTH VANADATE FILMS BY CHEMICAL VAPOR DEPOSITION AND THEIR CHARACTERIZATION

5.1 Introduction

Bismuth vanadate, $BiVO_4$ (BVO), with a band gap of 2.4 eV, is a recently discovered photocatalyst for water splitting, first reported in 1999.[1] Its conduction band minimum lies at -0.46 V (vs. NHE) and valence band maxima at 1.94 V (vs NHE), which makes it suitable for water oxidation (1.23 V vs. NHE). It is a low cost material with high absorption coefficient and high abundance. The theoretical calculated water splitting conversion efficiency has been reported to be 9.2 %, with a maximum photocurrent of 7.5 mA/cm^2 under standard 1.5 solar light irradiation.[2] However, the experimentally attained efficiency is far less than the calculated efficiency because of the following material drawbacks: (i) poor electron transport, leading to majority of carriers to be recombined and lost; (ii) sluggish water oxidation kinetics at the catalyst surface; (iii) leaching of V^{5+} ion in aqueous environment that causes instability.[3, 4]

BVO exists in three polymorphs - orthorhombic pucherite, tetragonal dreyerite and monoclinic clinobisvanite. The monoclinic clinobisvanite phase is thermodynamically the most stable phase and exhibits the best photocatalytic behavior amongst the three phases. The clinobisvanite crystal has a space group of I2/b with lattice parameter values of a=5.1935 Å, b=5.0898 Å, c=11.6972 Å, β=90.3871°.[5] The crystal structure of $BiVO_4$ consists of alternate Bi_2O_3 and V_2O_5 units stacked along the c-axis direction. The Bi^{3+} ion is connected to oxygen in a distorted oxygen octahedron

and the V^{5+} ion connects to oxygen via distorted tetrahedron. The crystal lattice consists of a layered structure with alternating -Bi-V- configuration along the *a* and *c* axis, and -Bi-V-V-Bi- along the *b* axis (figure 5.1).[5, 6] $BiVO_4$ is a direct band gap semiconductor with two (Γ(000) and A(1/2 00)) high symmetry lines in the Brillouin zone. At the Γ(000) point, the valence band maxima consists of O 2*p* while the conduction band minima consists of V 3*d*. At the A(1/2 00), the valence band maxima consists of Bi 6*s* while the conduction band has contributions from Bi 6*p* and O 2*p*. This leads to the localization of photoinduced electrons, which in addition to the polar nature of $BiVO_4$ causes self-trapping of electrons that results in poor charge separation.[7] The direct band gap enables higher light absorption cross section, thus a thin layer of the semiconductor can be effective for absorbing the radiation. Despite the poor electron conductivity, $BiVO_4$ has a relatively long hole diffusion length of 70 nm due to the lower effective mass of holes (m_0=0.7 c.a.) as compared to the effective mass of electron (m_e=0.9 c.a.).[4, 6, 8]

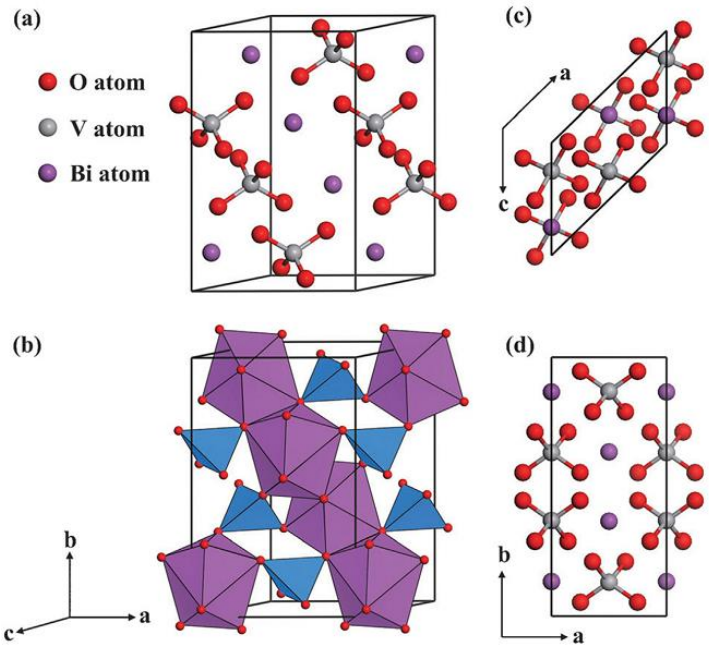

Figure 5.1: Crystal structure of $BiVO_4$ (Blue: bismuth, red: oxygen, green: vanadium). Reproduced with permission from ref. 6 copyright 2011, Royal Society of Chemistry

5.2 Strategies to improve the photocatalytic efficiency of $BiVO_4$

Several synthesis strategies have been utilized to overcome the material drawbacks of BVO and improve its effectiveness for water oxidation. These are listed below:

5.2.1 Doping

Modification of electrical and optical properties by doping is one of the important strategies to improve the photoactivity of $BiVO_4$. Structurally, doping of ions in a semiconductor lattice can have the following effects: (i) alter the band gap by introducing donor or acceptor levels in the forbidden region, and (ii) increasing the carrier density. Depending on the nature of the dopant ion, it can have a positive or negative effect on the photoactivity. For e.g., W and Mo dopants in $BiVO_4$ have been shown to enhance photoactivity by increasing the carrier density and does not introduce discrete energy levels.[8-10] However, Cr^{5+} doping introduces a localized impurity state which acts as a recombination center. This is due to the lower *d* orbital energy in Cr^{5+} as compared to W and Mo (Cr 3*d* < Mo 4*d* < W 5*d*).[11] Based on DFT calculations, Mo^{6+} and W^{6+} have higher orbital overlap and effective hybridization with V^{5+}, leading to higher carrier density.[11] $BiVO_4$ has a poor electron conductivity and thus a significant difference is observed between the front and back side illumination photocurrents. Introduction of dopant ions in the lattice and increased carrier density results in a decrease in the difference between front and back illumination.

In addition to cation doping, oxyanion doping has been reported for $BiVO_4$. An increase in the carrier density with no change in the band gap is observed when PO_4^- anions are used to replace VO_4^-, similar to Mo/W doping.[12]

5.2.2 Facet engineering

The electronic structure of materials are dependent on the crystal structures and thus certain crystal facets have higher surface active sites and exhibit higher reaction rates as compared to others. Thus, synthesis of catalysts with different exposed facets have been widely studied and explored. For $BiVO_4$, DFT calculations show that the (011) and (010) facets have a higher activity because of higher carrier mobility, easier adsorption of water and lower overall potential energy for O_2 evolution.[13] $BiVO_4$ nanoplatelets with exposed {001} facets, [14] and dodecahedron crystals with {010}, {011}, {011}, and {011} exposed facets have been reported to show higher photocatalytic activity.[15]

5.2.3 Co-catalysts

Oxygen evolution catalysts such as transition metal oxides: RuO_2, IrO_2, CoO_x, MnO_x, RhO_x, hydroxides such as FeOOH, NiOOH, and phosphate such as Co-Pi help to accelerate the surface reaction kinetics.[2] Choi *et al* observed that a single OER catalyst cannot make good interfaces with $BiVO_4$ and water simultaneously. Thus they chose to separate this by employing iron oxide for forming good junction with $BiVO_4$ and NiOOH for good interface with water. They photodeposited both FeOOH and NiOOH on $BiVO_4$ layers of 76 nm thickness and observed photocurrents as high as 4.5 mA/cm^2.[16]

5.2.4 Composites

Several different BVO composites have been synthesized to enhance the electron mobility, increase absorption and improve charge separation efficiency. BVO has been coupled with carbon, carbon nanotubes and graphene. Due to the abundance of delocalized electrons from the conjugated sp^2 bonded carbon network, such materials help enhance the transport of photoinduced

electrons.[17-20] Plasmonic nanostructures have been incorporated in $BiVO_4$ that show enhanced photoactivity due to additional optical absorption from the SPR of nanoparticles.[21]

Forming semiconductor heterostructures based on valence band and conduction band positions of metal oxides is known to improve the charge separation efficiency of BVO. Guo *et al* synthesized WO_3 nanowires coated with $BiVO_4$ and found an increase in the photoresponse since the WO_3 nanowires help in efficient transport of the photogenerated electrons. In addition, as the conduction band of WO_3 is slightly lower in position as compared to $BiVO_4$, it helps in efficient charge transfer.[22] P-N junctions have also been formed by the association of oxide layers. For e.g., Song *et al* synthesized a BiOCl-$BiVO_4$ p-n junction where the BiOCl acts as a *p*-type layer and $BiVO_4$ as *n*-type layer. Both the materials absorb light and because of suitable band alignment, the holes are transferred to the BiOCl layer and electrons to the $BiVO_4$ layer. Such composite showed enhanced photodegradation of methyl orange dye due to enhanced carrier separation efficiency.[23]

5.2.5 Morphology control

Considering the poor electron transport in $BiVO_4$, use of 1-dimensional nanostructures such as nanowires, nanorods, nanowires, nanotubes or nanobelts, which accelerate charge movement and assist collection and electron-hole pair separation at the material interface. Higher photoactivity is expected with improved electron transport in dimensional nanostructures.[20] Tailoring porosity of the material in order to increase the surface reaction sites has also been explored. Ordered mesoporous $BiVO_4$ fabricated by nanocasting using mesoporous silica template exhibit higher photoactivity as compared to a conventional $BiVO_4$.[24] It was also observed that there exists an optimum pore size for an efficient photo-induced charge drift mobility.[24]

Thin films of $BiVO_4$ have been synthesized by methods such as aerosol assisted CVD,[25] vapor transport CVD,[26] and pulsed laser deposition (PLD).[27] Such methods have the advantage of producing high quality films with fewer grain boundaries and other defects, which help in more efficient charge carrier transport. Thin film deposition techniques such as PLD require high vacuum and high deposition temperatures that can affect the FTO substrate, and have a low deposition rate. Herein we report the synthesis of pure-phase monoclinic $BiVO_4$ by direct liquid injection CVD technique. It involves the use of a moderate vacuum and temperatures to yield high quality epitaxial and polycrystalline films with high deposition rate (~10 nm/min).[28] The DLI-CVD technique has been optimized to grow epitaxial films on cubic yttria-stabilized zirconia (YSZ) at 500 and 550 ^oC. To the best of our knowledge, epitaxial films have previously not been grown on YSZ substrate by DLI-CVD technique. Similar conditions are used to deposit continuous and dense polycrystalline $BiVO_4$ films on FTO substrate and tested for photocatalytic water splitting.

5.3 Materials and methods

FTO coated glass substrates (0.5 cm × 1 cm; 25 Ω/□, Pilkington Glass Co. Ltd., U.S.A) were cleaned using detergent followed by washing with copious amount of DI water prior to being cleaned ultrasonically in acetone and isopropanol, each for 30 min. Yttria-stabilized zirconia (YSZ) substrates (5 ×5 mm) of (001) orientation were purchased from CrysTec GmbH Kristalltechnologie, Berlin Germany. A thin layer of WO_3 was deposited by spin coating a solution of HWO_4 (0.01g) in 1:1 solution of ammonium hydroxide and ethanol. Direct liquid injection chemical vapor deposition (DLI-CVD) technique was used for deposition of $BiVO_4$ films. Vanadyl acetylacetonoate ($VO(C_5H_7O_2)_2$) and triphenyl bismuth ($Bi(C_6H_5)_3$), Acros Organics, were chosen as precursors because of their solubility and stability in dimethyl formamide (DMF)

solvent. A solution consisting of 0.0125 M triphenyl bismuth (Acros Organics) and 0.025M vanadyl acetylacetonoate solution in DMF was used as precursor solution. Vanadyl acetylacetonoate had partial solubility in DMF hence half the concentration of triphenyl bismuth was used. Thickness of the deposited films was varied by varying the deposition times from 15, 30, 45, 60, 75 and 90 minutes.

Deposition parameter	**Values**
Argon (carrier gas) flow rate	300 sccm
Oxygen flow rate	120 sccm
Base pressure	1 Torr
Precursor solution flow rate	5 g/hr
Deposition temperatures	500, 550^{o}C

Table 5.1: CVD parameters for deposition of BVO.

5.4 Structural and photoelectrochemical characterizations

The absorption characteristics of the films were recorded with a UV-Visible spectrophotometer (Agilent, Cary 500, USA). X-ray diffraction (XRD) patterns of films grown on YSZ substrates were recorded using a X-ray diffractometer (Philips X'Pert Pro, Cu Kα source), while those grown on FTO substrates were recorded with a Bruker D8 Discover XRD with GADDS, employing CoKα radiation. Surface morphology and chemical composition of the thin films were studied by JEOL 700 Scanning electron microscope. The surface roughness of $BiVO_4$ films on YSZ samples was determined by AFM (Asylum Research).

The water splitting characteristics of the films were studied by recording I-V characteristics in a three-electrode cell configuration consisting of platinum wire and Ag/AgCl (saturated with KCl) as counter and reference electrodes, respectively, in 0.1 M Na_2SO_3 solution. The electrode potential was scanned from -0.5 to 1.2 V using a potentiostat (Princeton EG&G Applied Research) and the corresponding current was recorded. The measurements were performed in the dark and under light using a Xe arc lamp at AM 1.5G conditions. Action spectra of the electrodes were recorded in 0.1 M Na_2SO_3 by measuring the current response while holding the potential constant at 0.3 V (vs. Ag/AgCl) using a CHI 760 potentiostat (CH Instruments, Inc., Austin, TX). Monochromatic light from 300 to 750 nm was obtained from a monochromator (MD 1000, Optical Building Blocks) with white light input from a Xe arc lamp. Current vs. time graphs were recorded with the potentiostat and the time scale was then converted to wavelength scale to obtain the action spectra characteristics. The action spectra were converted to incident photon conversion efficiency (IPCE) using the relation,

$$IPCE(\%) = \frac{1240 \times I(mA/cm^2)}{\lambda(nm) \times P_{inc}(mW/cm^2)} \times 100$$

5.5 Results and discussions

5.5.1 Characterization of $BiVO_4$ on YSZ substrate

Polished cubic yttria-stabilized zirconia (a = 5.145 Å) substrates with (001) orientation were chosen to grow epitaxial $BiVO_4$ (a = 5.1956 Å) films because of low mismatch in the lattice parameter values. $BiVO_4$ was grown on YSZ substrates at two different temperatures, 500 and 550 ^oC for 45 mins to yield a film thickness of 400 nm. Epitaxial growth of $BiVO_4$ results in *c*-oriented crystal growth exhibiting only the (*00h*) diffraction peaks. The XRD patterns of the as-deposited films are shown in figure 5.2 a. Besides substrate peaks, all the remaining peaks can be indexed to

$BiVO_4$ corresponding to (001) orientation, which confirm the epitaxial growth at both temperatures. Rocking curve (ω) scan analysis of $BiVO_4$ (004) diffraction peak was used to characterize the degree of film texture. The measured full width at half maximum (FWHM)values are 0.25° and 0.13° for film grown at 500 and 550 °C, respectively (figure 5.2 b).

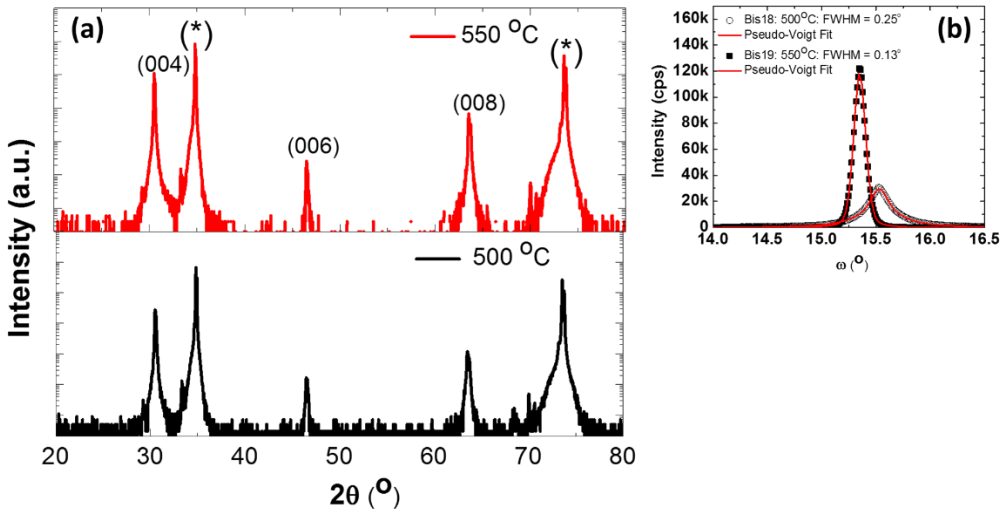

Figure 5.2: θ- 2θ XRD scan of BVO (400 nm)/YSZ showing only (001) reflections of BVO and YSZ (marked by *). (b) Rocking curve around the (004) peak of the epitaxial BVO film (2θ= 30.545°).

Figure 5.3 shows AFM images of the $BiVO_4$ films grown on YSZ substrates. The roughness values were calculated to be 12 and 8 nm for the 500 and 550 °C films, respectively. EDS analysis to determine chemical composition reveals a Bi: V ratio of ~1 for the 550 °C sample and somewhat excess V in the 500 °C sample. (Table 1)

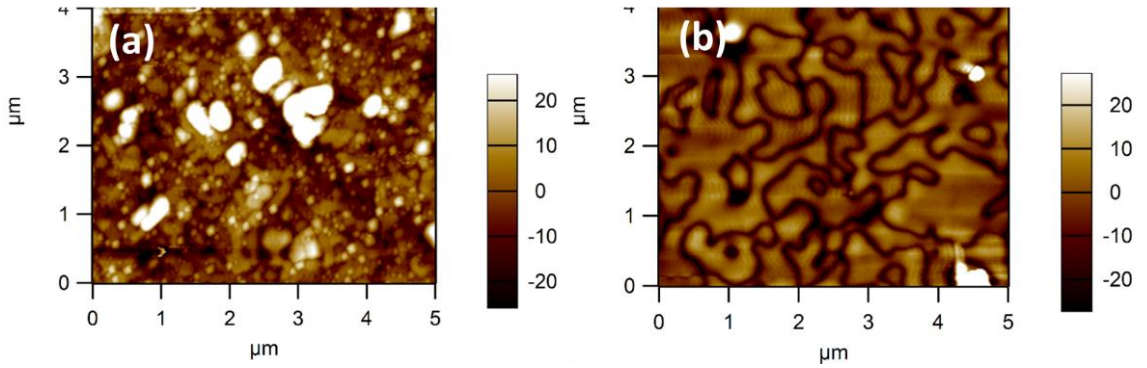

Figure 5.3: AFM images of epitaxial BVO grown on YSZ (a) 500 ºC and (b) 550 ºC.

Substrate temperature (º C)	Chemical composition (at. wt. %)		Roughness (nm)	Rocking curve FWHM (º)	Thickness (nm)
	Bi	V			
500	45.12	54.88	12.8 ± 2	0.25	400 ± 5
550	49.40	50.60	8 ± 2	0.13	400 ± 5

Table 5.2: Characteristics of BVO film grown on YSZ substrates by DLI-CVD technique.

Absorption spectra of the BVO films grown on YSZ were recorded (figure 5.4 a). Absorption in thin films is a complex function of grain size and morphology. The band gap of BVO is reported to be ~2.4 eV for nanoparticles, while thin films have been reported to have a band gap of 2.5 -2.6 eV. Tauc plots were obtained from the absorption spectrum of samples using the following equation:

$$(\alpha h\nu)^n = A(h\nu - E_g)$$

where, α = absorbance at given wavelength, h = Planck's constant, ν = frequency, E_g = band gap of the material, A = absorption coefficient, n = 2 or 0.5 for a direct and indirect band gap semiconductor, respectively.[25] A graph of $(\alpha h\nu)^2$ vs. $h\nu$ was plotted. Extrapolation of the plot to the x-axis gives a direct band gap value of 2.57 eV for the films grown both at 500 and 550 °C (figure 5.4 b).

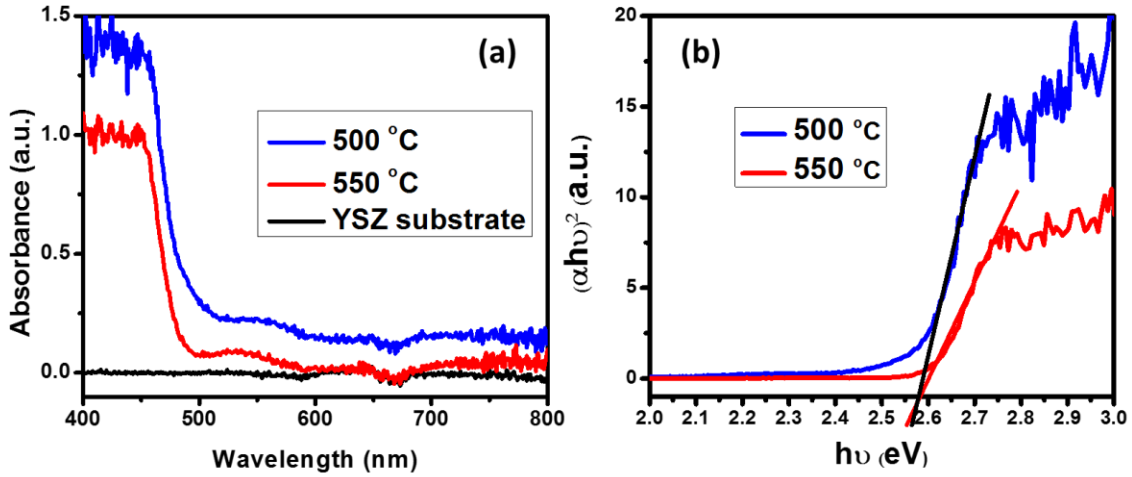

Figure 5.4: (a) UV-Vis absorption spectrum of BVO films grown at 500 and 550 °C on YSZ substrates. (b) Tauc plots to calculate the band gap of the films.

Thus the direct liquid injection CVD technique enables growth of high quality BVO films on YSZ substrates at much lower temperatures (500 - 500 °C) than reported using PLD method grown (700 °C).[27] In addition, they have FWHM values of 0.25 and 0.13° as compared to PLD grown films of 0.3°.

5.5.2 Characterization of $BiVO_4$ films on FTO substrate

The optimized conditions were used to grow polycrystalline films on FTO substrates. Figure 5.5 shows the XRD pattern of BVO grown on FTO substrates at 500 and 550 °C. The XRD patterns

match well with the standard monoclinic phase $BiVO_4$ (Clinobisvanite) pattern (JCPDS-00-014-0688) indicated with a stick plot in the figure 5.5. EDS analysis was performed to determine the chemical composition of the samples and were found to be similar to that of BVO grown on YSZ at the two temperatures. UV-Vis absorption spectra of the films were recorded and band gaps were calculated (figure 5.6). The band gap values of BVO on FTO at the two growth temperatures were the same as those grown on YSZ substrates. Thus it can be concluded that the growth characteristics of BVO on FTO are the same as that on YSZ substrates.

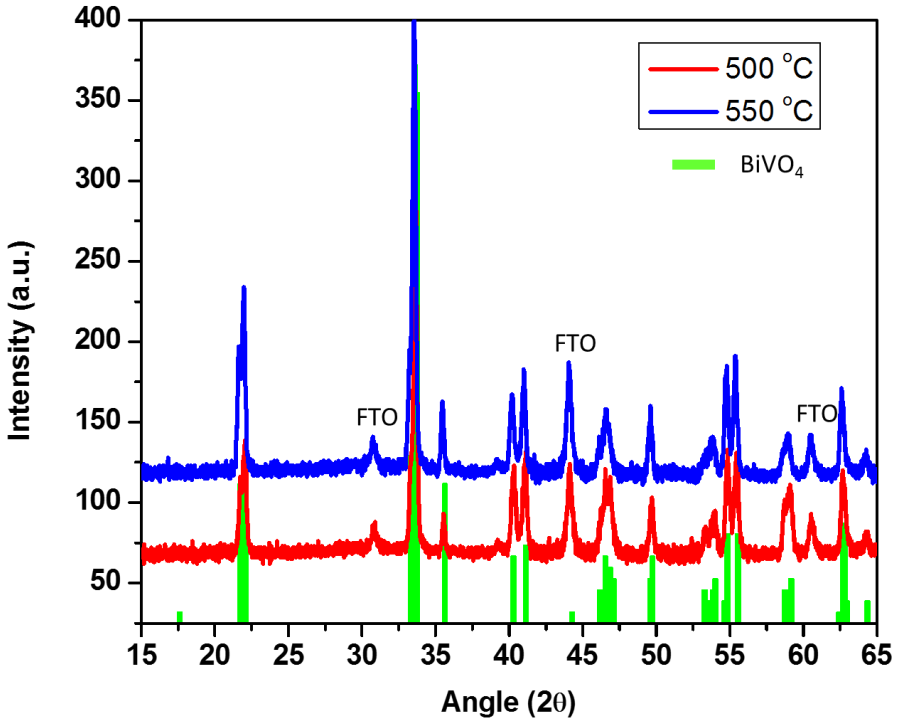

Figure 5.5: XRD patterns of BVO grown on FTO at 500 and 550°C in comparison with standard monoclinic phase clinobisvanate BVO pattern (JCPDS-00-014-0688) represented as a stick plot.

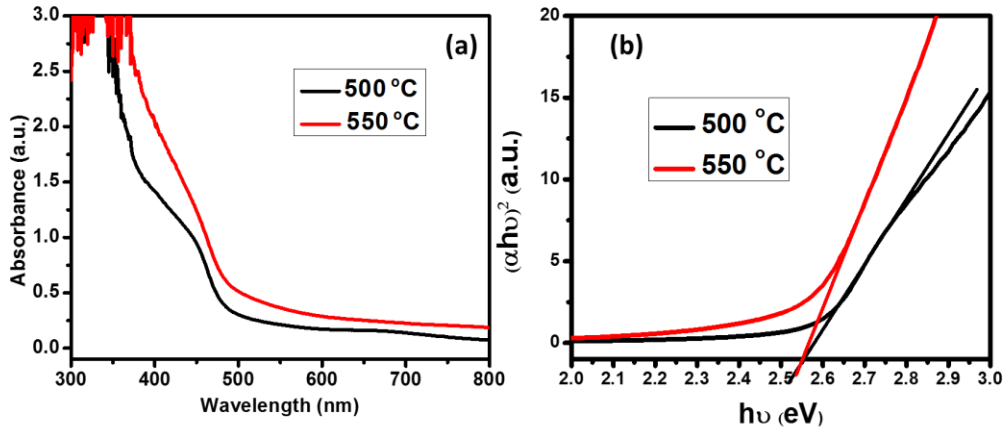

Figure 5.6: (a) UV Vis spectra of BVO films grown on FTO substrate at 500 and 550 ^{o}C. (b) Corresponding Tauc plots to determine the band gap of 2.55 eV.

5.5.3 Growth of different thickness BVO films on FTO substrates

To study photocatalytic water splitting activity, different thickness BVO were deposited on FTO by changing the deposition time from 30, 45, 60, 90 mins to yield thicknesses of 250, 400, 600, 800 nm each. The thickness of the films were determined by cross section SEM. The deposition rate of BVO is the same at 500 and 550 ^{o}C. The surface morphology of the BVO films with increasing thickness is shown in Figure 5.7. After 30 mins deposition (250 nm thickness) the film morphology is continuous, and with increasing thickness the grain size of the films increases. Films grown at 550 ^{o}C show a smoother texture and larger grain size as compared to those grown at 500 ^{o}C.

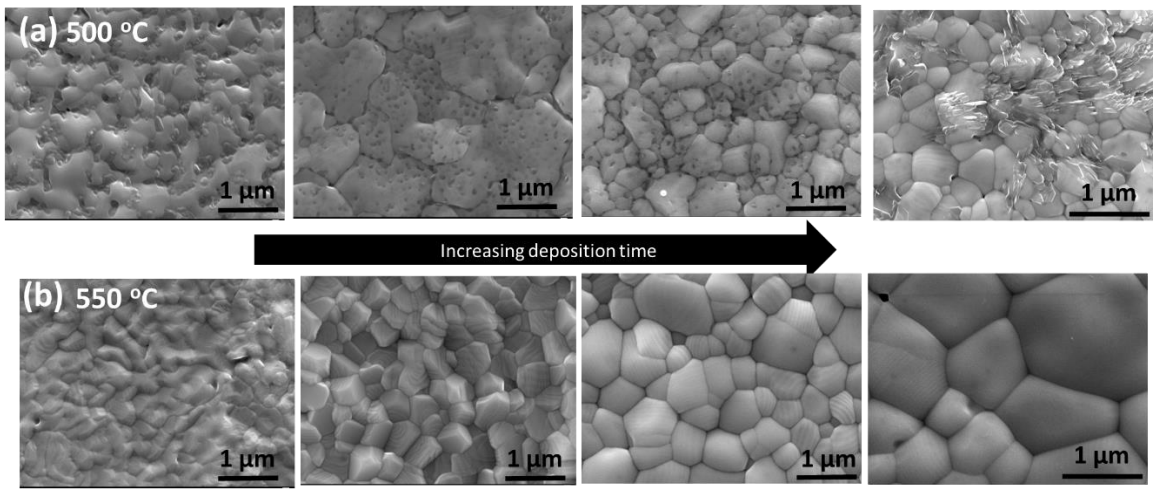

Figure 5.7: SEM images of BVO films on FTO as a function of increasing thickness of 250, 400, 500, 800 nm (left to right). Top panel (a) films grown at 500 °C, and bottom panel (b) grown at 550 °C.

Cross section SEM images of 800 nm films (figure 5.8) grown at the two temperatures reveal a compact morphology with no porosity or pin holes. The UV-Vis absorption spectra of the films show similar values of absorbance for a given thickness, which also confirms the equal thickness of the films (figure 5.8). The peaks observed in the absorption spectrum of 800 nm thick films (at 525 nm) can be attributed to the interference occurring in the films and not due to the absorption.

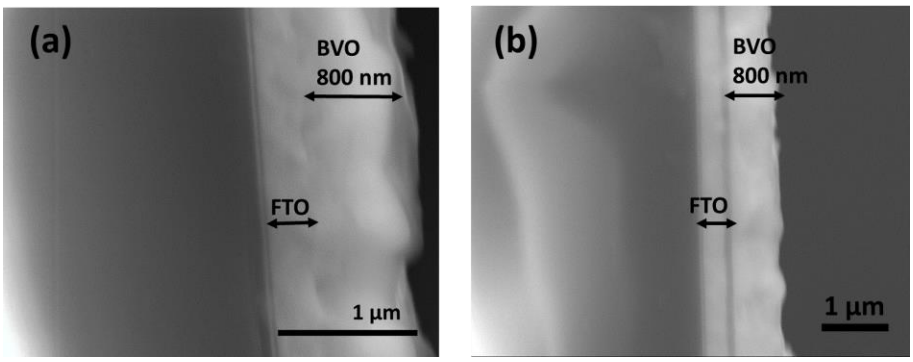

Figure 5.8: Cross section SEM image of 800 nm BVO film on FTO grown at a temperature of (a) 500 °C and (b) 550 °C.

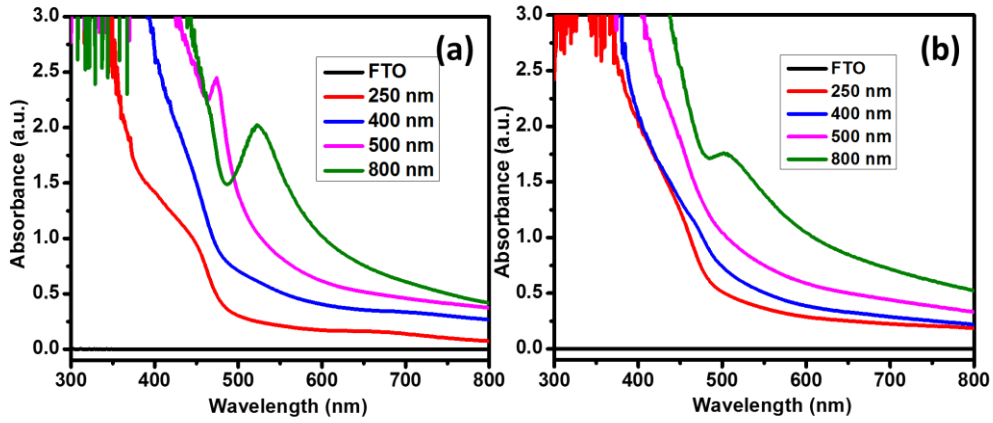

Figure 5.9: Absorption spectrum of different thickness BVO films grown on FTO at (a) 500 ^{o}C, and (b) 550 ^{o}C. Shoulder peaks due to interference effects in the thicker films.

5.5.4 Current-voltage and IPCE characteristics

The PEC water splitting performance of different thickness BVO grown on FTO at 500 ^{o}C and 550 ^{o}C were tested by recording the current-voltage (I-V) characteristics in the dark and under irradiation conditions (figure 5.10). The photo-characteristics were studied only with back side illumination. Considerably poorer photocurrent was observed with front side illumination due to the poor electron mobility in BVO. For films grown at 500 ^{o}C, the photocurrent for a given thickness was always lower as compared to that grown at 550 ^{o}C. For both the growth temperatures, it is seen that the thinnest film (250 nm) gives the highest photocurrent. Moreover, a higher photocurrent was obtained for a film thickness of 250 nm film grown at 550 ^{o}C (2.1 mA/cm^{2}) compared to that of 550 ^{o}C (1.4 mA/cm^{2}) recorded at 0.5 V vs. Ag/AgCl. APCVD grown similar morphology, 200 nm thick BVO films yielded a photocurrent of 0.8 mA/cm^{2} at 0.5 V Vs Ag/AgCl.[26] The higher photocurrent could be attributed to the improved crystallinity of the film grown at higher temperature. Chopped light I-V curves (from -0.7 to 0.2 V vs. Ag/AgCl) were recorded for the 250 nm films grown at 500 and 550 ^{o}C to study the effect of growth temperature on the onset potential values for water oxidation (figure 5.10c). No significant differences were

observed, with both the films exhibiting excellent onset potential value of -0.55 V as compared to other literature reported values of 0.2 - 0.1 V and -0.3V vs Ag/AgCl for films frown by AACVD,[25] PLD[27] and APCVD,[26] respectively. This suggests that the origin of lower photocurrent in 500 ^{o}C grown film is likely due to lower crystallinity and not due to surface defects in the film.

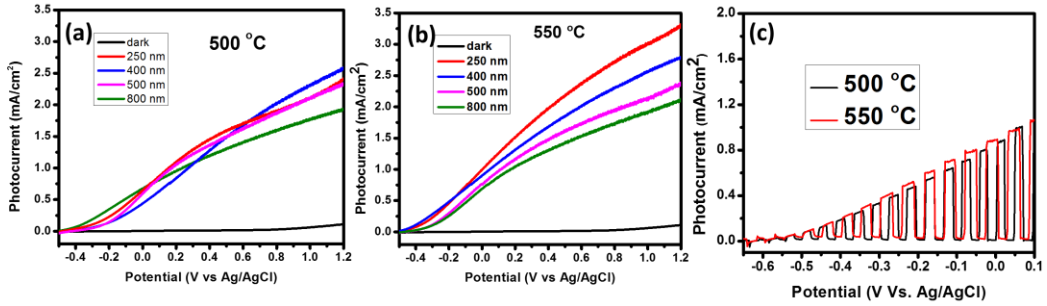

Figure 5.10: I-V characteristics of different thickness BVO films grown on FTO at (a) 500 ^{o}C and (b) 550 ^{o}C. (c) Chopped light characteristics of 250 nm films showing onset potential values of 0.55 vs. Ag/AgCl.

Incident photocurrent conversion efficiency (IPCE) of the 250 nm BVO electrodes were recorded in order to determine the photoactive wavelength range of the electrodes (figure 5.11). The IPCE is observed to follow a similar trend as that of the UV-Vis absorption characteristics of the electrodes. The BVO electrode grown at 550 ^{o}C shows a higher IPCE as compared to that of 500 ^{o}C due to better charge transport efficiency.

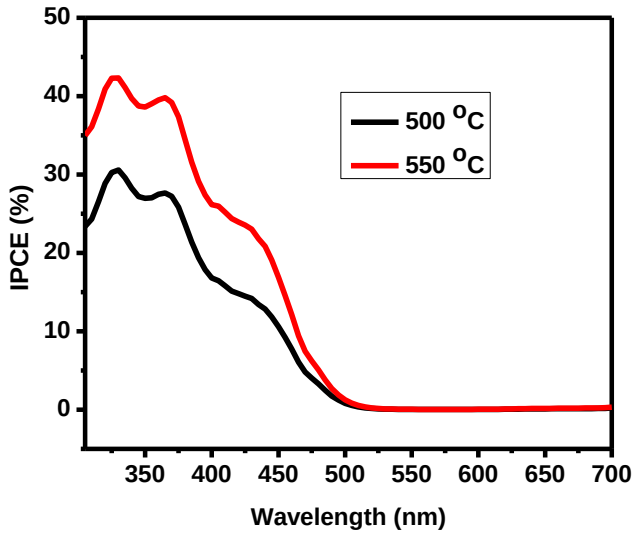

Figure 5.11: IPCE spectrum of BVO electrodes grown at 500 and 550 °C.

5.5.5 Tungsten oxide underlayers to improve electron transport in BVO

To improve the electron transport efficiency of the best performing (250 nm) BVO films, tungsten oxide underlayers were employed. I-V characteristics of the BVO with WO_3 underlayers were recorded (figure 5.12). An increment of ~ 1 mA was observed in the 500 °C film as compared to an increment of 0.5 mA in the 550 °C grown film at 0.5 V vs. Ag/AgCl. This further confirms that the higher growth temperature yields improved crystallinity films that have better electron mobility.

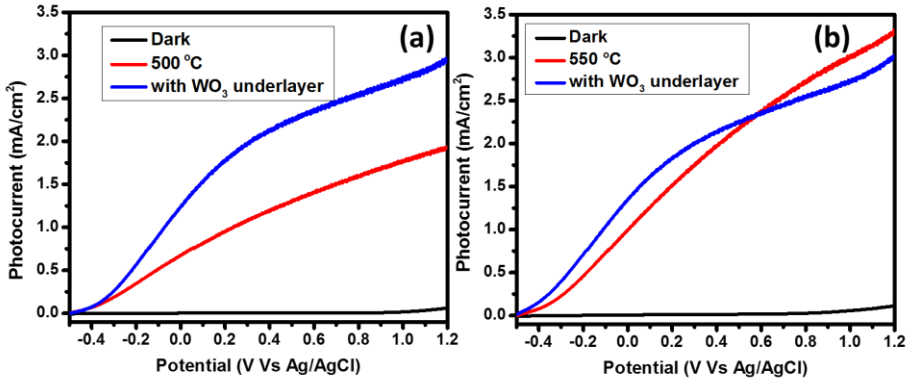

Figure 5.12: I-V characteristics of 250 nm BVO films grown on WO_3 underlayer (a) 500 ^oC and (b) 550 ^oC.

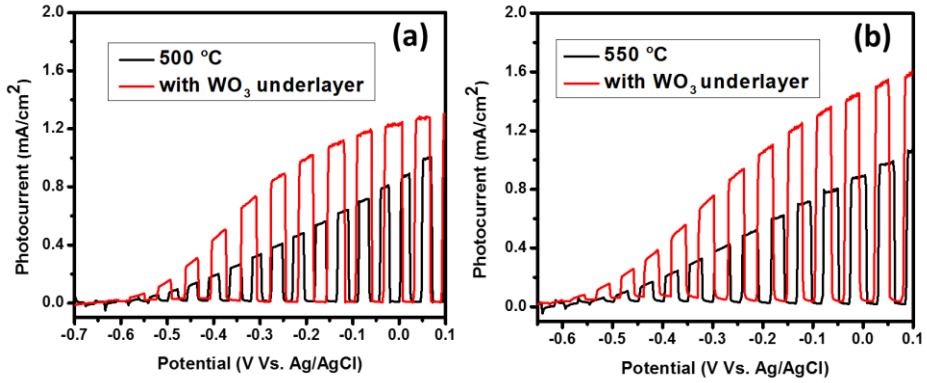

Figure 5.13: Chopped light I-V characteristics of 250 nm BVO films grown with and without WO_3 underlayer (a) 500 ^oC and (b) 550 ^oC.

A chopped light I-V of the BVO films grown on the WO_3 layer indicate no significant changes in the onset potential values of the films (figure 5.13). All the films show an onset potential value of -0.55 V vs Ag/AgCl indicating that WO_3 layer acts as a better electron transport layer for BVO films and does not alter the growth characteristics of the film.

5.6 Conclusions

The DLI-CVD technique has been optimized to fabricate epitaxial thin films on YSZ substrate. The same conditions are used to grow high quality polycrystalline thin films on FTO substrate. X-Ray diffraction, UV-Vis spectroscopy and EDS chemical composition analysis confirm the growth of monoclinic $BiVO_4$ phase for both the film types. The films have a compact dense structure with no porosity. Films as thick as 800 nm can be grown. A thickness and growth temperature dependent photoactivity measurements reveal best performance in films of 250 nm thickness grown on FTO at 550 ^oC. The onset potential values of the films are not affected by the growth temperature due to low density of surface defects in both films. WO_3 interlayers are employed to improve the electron transport in the BVO films, and the observed effect of WO_3 is higher in 500 ^oC film as compared to 550 ^oC grown film. Overall, it can be concluded that the DLI-CVD method is an efficient technique to deposit binary metal oxides like $BiVO_4$ with reduced surface defects, which yield better onset potential values. There is potential for further improvement of the efficiency of the films by doping, employing co-catalysts and also exploring alternative efficient electron transport layers and such works are under progress in our laboratory.

5.7 References

(1) Kudo, A.; Omori, K.; Kato, H. A Novel Aqueous Process for Preparation of Crystal Form-Controlled and Highly Crystalline $BiVO_4$ Powder from Layered Vanadates at Room Temperature and its Photocatalytic and Photophysical Properties. *J. Am. Chem. Soc.* **1999**, *121*, 11459-11467.

(2) Huang, Z.; Pan, L.; Zou, J.; Zhang, X.; Wang, L. Nanostructured Bismuth Vanadate-Based Materials for Solar-Energy-Driven Water Oxidation: A Review on Recent Progress. *Nanoscale* **2014**, *6*, 14044-14063.

(3) Kudo, A. Development of Photocatalyst Materials for Water Splitting with the Aim at Photon Energy Conversion. *J. Ceram. Soc. Jpn.* **2001**, *109*.

(4) Kim, J. H.; Lee, J. S. $BiVO_4$- Based Heterostructured Photocatalysts for Solar Water Splitting: A Review. *Energy and Environment Focus* **2014**, *3*, 339-353.

(5) Park, Y.; McDonald, K. J.; Choi, K.; Progress in Bismuth Vanadate Photoanodes for use in Solar Water Oxidation. *Chem. Soc. Rev.* **2013**, *42*, 2321-2337.

(6) Zhao, Z.; Li, Z.; Zou, Z. Electronic Structure and Optical Properties of Monoclinic Clinobisvanite BiVO4. *Phys. Chem. Chem. Phys.* **2011**, *13*, 4746-4753.

(7) Walsh, A.; Yan, Y.; Huda, M. N.; Al-Jassim, M.; Wei, S. Band Edge Electronic Structure of $BiVO_4$: Elucidating the Role of the Bi s and V D Orbitals. *Chem. Mater.* **2009**, *21*, 547-551.

(8) Rettie, A. J. E.; Lee, H. C.; Marshall, L. G.; Lin, J. -.; Capan, C.; Lindemuth, J.; McCloy, J. S.; Zhou, J.; Bard, A. J.; Mullins, C. B. Combined Charge Carrier Transport and Photoelectrochemical Characterization of $BiVO_4$ Single Crystals: Intrinsic Behavior of a Complex Metal Oxide. *J. Am. Chem. Soc.* **2013**, *135*, 11389-11396.

(9) Pattengale, B.; Ludwig, J.; Huang, J. Atomic Insight into the W-Doping Effect on Carrier Dynamics and Photoelectrochemical Properties of $BiVO_4$ Photoanodes. *J. Phys. Chem. C* **2016**, *120*, 1421-1427.

(10) Parmar, K. P. S.; Kang, H. J.; Bist, A.; Dua, P.; Jang, J. S.; Lee, J. S. Photocatalytic and Photoelectrochemical Water Oxidation Over Metal-Doped Monoclinic $BiVO_4$ Photoanodes. *ChemSusChem* **2012**, *5*, 1926-1934.

(11) Park, H. S.; Kweon, K. E.; Ye, H.; Paek, E.; Hwang, G. S.; Bard, A. J. Factors in the Metal Doping of $BiVO_4$ for Improved Photoelectrocatalytic Activity as Studied by Scanning Electrochemical Microscopy and First-Principles Density-Functional Calculation. *J. Phys. Chem. C* **2011**, *115*, 17870-17879.

(12) Jo, W. J.; Jang, J.; Kong, K.; Kang, H. J.; Kim, J. Y.; Jun, H.; Parmar, K. P. S.; Lee, J. S. Phosphate Doping into Monoclinic $BiVO_4$ for Enhanced Photoelectrochemical Water Oxidation Activity. *Angewandte Chemie International Edition* **2012**, *51*, 3147-3151.

(13) Yang, J.; Wang, D.; Zhou, X.; Li, C. A Theoretical Study on the Mechanism of Photocatalytic Oxygen Evolution on BiVO4 in Aqueous Solution. *Chem. -Eur. J.* **2013**, *19*, 1320-1326.

(14) Xi, G.; Ye, J. Synthesis of Bismuth Vanadate Nanoplates with Exposed {001} Facets and Enhanced Visible-Light Photocatalytic Properties. *Chem. Commun.* **2010**, *46*, 1893-1895.

(15) Wang, D.; Jiang, H.; Zong, X.; Xu, Q.; Ma, Y.; Li, G.; Li, C. Crystal Facet Dependence of Water Oxidation on $BiVO_4$ Sheets Under Visible Light Irradiation. *Chem. -Eur. J.* **2011**, *17*, 1275-1282.

(16) Kim, T.; Choi, K. -. Nanoporous $BiVO_4$ Photoanodes with Dual-Layer Oxygen Evolution Catalysts for Solar Water Splitting. *Science* **2014**, *343*, 990-994.

(17) Fu, Y.; Sun, X.; Wanga, X. $BiVO_4$-Graphene Catalyst and its High Photocatalytic Performance Under Visible Light Irradiation. *Mater. Chem. Phys.* **2011**, *131*, 325-330.

(18) Liu, B.; Li, Z.; Xu, S.; Ren, X.; Han, D.; Lu, D. Facile in Situ Hydrothermal Synthesis of $BiVO_4$/MWCNT Nanocomposites as High Performance Visible-Light Driven Photocatalysts. *J Phys Chem Solids* **2014**, *75*, 977-983.

(19) Ng, Y. H.; Iwase, A.; Kudo, A.; Amal, R. Reducing Graphene Oxide on a Visible-Light $BiVO_4$ Photocatalyst for an Enhanced Photoelectrochemical Water Splitting. *J. Phys. Chem. Lett.* **2010**, *1*, 2607-2612.

(20) Sun, Y.; Qu, B.; Liu, Q.; Gao, S.; Yan, Z.; Yan, W.; Pan, B.; Wei, S.; Xie, Y. Highly Efficient Visible-Light-Driven Photocatalytic Activities in Synthetic Ordered Monoclinic $BiVO_4$ Quantum Tubes-Graphene Nanocomposites. *Nanoscale* **2012**, *4*, 3761-3767.

(21) Abdi, F. F.; Dabirian, A.; Dam, B.; Van De Krol, R. Plasmonic Enhancement of the Optical Absorption and Catalytic Efficiency of $BiVO_4$ Photoanodes Decorated with $Ag@SiO_2$ Core-Shell Nanoparticles. *Phys. Chem. Chem. Phys.* **2014**, *16*, 15272-15277.

(22) Hong, S. J.; Lee, S.; Jang, J. S.; Lee, J. S. Heterojunction $BiVO_4/WO_3$ Electrodes for Enhanced Photoactivity of Water Oxidation. *Energy Environ. Sci.* **2011**, *4*, 1781-1787.

(23) He, Z.; Shi, Y.; Gao, C.; Wen, L.; Chen, J.; Song, S. BiOCl/ $BiVO_4$ P-N Heterojunction with Enhanced Photocatalytic Activity Under Visible-Light Irradiation. *J. Phys. Chem. C* **2014**, *118*, 389-398.

(24) Zhou, M.; Wu, H. B.; Bao, J.; Liang, L.; Lou, X. W.; Xie, Y. Ordered Macroporous $BiVO_4$ Architectures with Controllable Dual Porosity for Efficient Solar Water Splitting. *Angew. Chem. Int. Ed.* **2013**, *52*, 8579-8583.

(25) Brack, P.; Sagu, J. S.; Peiris, T. A. N.; McInnes, A.; Senili, M.; Wijayantha, K. G. U.; Marken, F.; Selli, E. Aerosol-Assisted CVD of Bismuth Vanadate Thin Films and their Photoelectrochemical Properties. *Chem Vapor Deposition* **2015**, *21*, 41-45.

(26) Alarcón-Lladó, E.; Chen, L.; Hettick, M.; Mashouf, N.; Lin, Y.; Javey, A.; Ager, J. W. $BiVO_4$ Thin Film Photoanodes Grown by Chemical Vapor Deposition. *Phys. Chem. Chem. Phys.* **2014**, *16*, 1651-1657.

(27) Rettie, A. J. E.; Mozaffari, S.; McDaniel, M. D.; Pearson, K. N.; Ekerdt, J. G.; Markert, J. T.; Mullins, C. B. Pulsed Laser Deposition of Epitaxial and Polycrystalline Bismuth Vanadate Thin Films. *J. Phys. Chem. C* **2014**, *118*, 26543-26550.

(28) Archana, P. S.; Pachauri, N.; Shan, Z.; Pan, S.; Gupta, A. Plasmonic Enhancement of Photoactivity by Gold Nanoparticles Embedded in Hematite Films. *J. Phys. Chem. C* **2015**, *119*, 15506-15516.

CHAPTER 6

CONCLUSIONS AND FUTURE WORK

6.1 Summary

A general overview of photocatalytic water splitting on semiconductor oxides has been provided and the major hurdles in realizing a practical photoelectrolysis cell can be pinned down to several material specific drawbacks such as: (i) low absorption, (ii) inefficient carrier transport, (iii) sluggish surface reaction kinetics, and (iv) poor charge separation efficiency. To overcome these issues, material modifications such as forming composites, multilayer structures, adsorption of high efficiency oxygen evolution co-catalysts, forming defect-free high surface area nanomaterials have been considered. In the current study high quality and single-phase semiconductor films have been synthesized by direct liquid injection chemical vapor deposition (DLI-CVD) process and their photocatalytic activity for water oxidation reaction is studied. Efforts to further improve the photoactivity are described.

Chapter 3 describes the synthesis of hematite films by DLI-CVD on different interlayer oxides (ZnO, TiO_2, Nb_2O_5, NiO and SiO_2) layers deposited on FTO and it is observed that the nature of the interlayer oxide affects the photoelectrochemical water oxidation performance of the hematite. The interlayer oxides have a substantial influence on the grain growth characteristics of the hematite that affects the onset potential value for water oxidation potential. These effects are predominantly due to the diffusion of ions from interlayer ion into the hematite layer during the growth process. Ion diffusion cause doping of the hematite film to increase its carrier density.

Moreover, the dopants are observed to affect grain growth and film morphology that affect the carrier transfer across the semiconductor-electrolyte interface, thus hindering the overall water splitting efficiency. Based on our experimental results it is shown that TiO_2 and Nb_2O_5 prove to be ideal electron transport layers without inducing defects in the hematite film. Zinc oxide increases the career density in the film but the overall efficiency of the film is compromised due to charge accumulation. The morphology and thickness of the TiO_2 layer also affects the performance of the hematite. A thin 50 nm TiO_2 layer results in the highest photocurrent. As the thickness and porosity of the underlying TiO_2 is increased the photocurrent in the hematite film is reduced due to increase in the resistance and higher porosity that induces surface defects. Thus the overall photocurrent and onset potential in the hematite film are improved by identifying and employing an ideal interlayer material.

A major drawback pertaining to hematite is its poor absorption coefficient and low hole diffusion length (< 4 nm), which limits the electrode thickness to < 100 nm. To overcome this, Au nanoparticles are embedded in the hematite film to enhance its absorption. It is observed that plasmonic Au NPs embedded in hematite films increases the absorbance in the hematite film by plasmonic light concentration and scattering effects of Au surface plasmon resonance. A thickness-dependent study indicates that the effect of Au nanoparticles is predominant in 107 nm films than in 630 nm films due to greater interaction of light with the Au nanoparticles. Mott-Schottky plots and electrochemical impedance spectroscopy studies indicate an enhancement in charge carrier density and a lower value for charge transfer resistance of thinner hematite films by incorporation of Au NPs. In addition, the embedded configuration has the advantage of higher stability and longer cyclability as they are not exposed to the electrolyte solution.[1]

Chapter 5 describes the synthesis of bismuth vanadate ($BiVO_4$ or BVO) by the DLI-CVD system. BVO is chosen as a material of interest due to its high absorption coefficient and high hole diffusion length of 70 nm. Its major drawback being the low electron diffusion length. The DLI-CVD technique is optimized to fabricate epitaxial and polycrystalline thin films on YSZ and FTO substrates, respectively. X-Ray diffraction, UV-Vis and EDS chemical composition analysis confirm the growth of monoclinic $BiVO_4$ phase for both the film types. The films exhibit a compact and dense structure with no porosity, and 800 nm thick films have been grown. Thickness and growth temperature dependent photoactivity measurements reveal optimum performance in thin films of 250 nm grown at 550 ^oC. The onset potential values of the films do not show an effect on the growth temperature due to low surface defects in both films. A WO_3 interlayer has been employed to improve the poor electron transport in the BVO films, and the effect of the interlayer is higher in the 500 ^oC grown film as compared to that grown at 550 ^oC. Thus, it can be said that the DLI-CVD method is an efficient technique to deposit binary metal oxides like $BiVO_4$ with low surface defect states, which yield improved onset potential values.

6.2 Impact of the study

The DLI-CVD grown oxide films show high crystallinity that results in low surface defect states, thus increasing the charge transfer efficiency and lower onset potential values. Figure 6.1 shows the performance of DLI-CVD deposited hematite films as compared to some of the best reported photocurrent values obtained in films grown by aerosol-assisted CVD method.[2] Our DLI-CVD films have potential for further improvement in the photoactivity by doping and by incorporating co-catalysts on the surface.

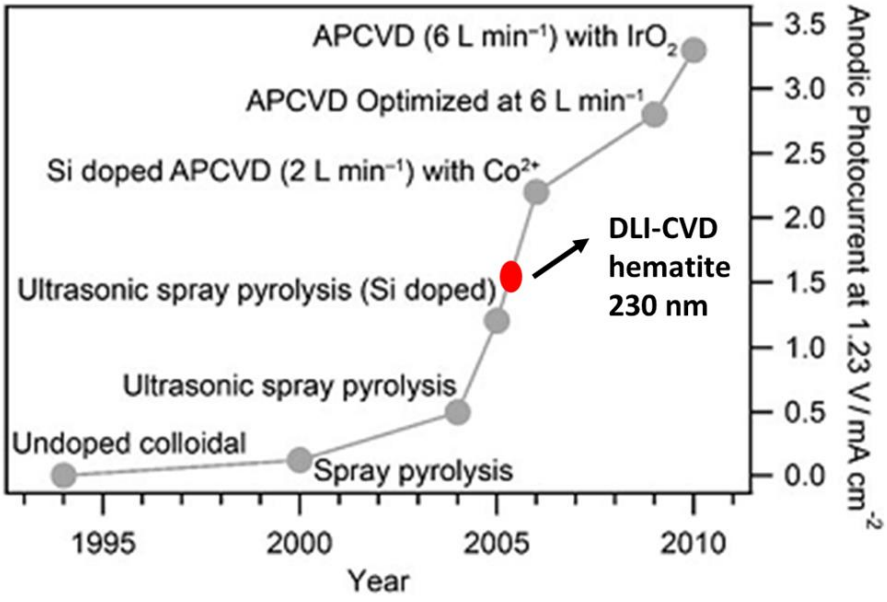

Figure 6.1: Performance of DLI-CVD grown hematite films as compared to some of the best reported hematite films. (Figure reproduced from ref. 2, Copyright 2011 WILEY-VCH Verlag GmbH & Co. KGaA, Weinheim).

Despite being expensive, DLI - CVD is a scalable method and can be used to coat large area films for practical applications. We have also demonstrated that the method can be readily optimized to phase-pure binary metal oxides with the desired stoichiometry. As opposed to other film deposition methods such as pulsed laser deposition, aerosol assisted CVD and atmospheric pressure CVD, the DLI-CVD technique provides precise control to obtain low surface roughness films with tunable growth rate by changing the precursor concentration. The method can yield films as thick as 800 nm for 90 mins. By embedding Au nanoparticles we have been able to effectively increase the absorption of hematite films implying that optically thick yet physically thin electrodes can be fabricated. This concept can be extended to design other materials for high efficiency solar cells.

6.3 Future Work

The films grown have a potential to improve the efficiency by doping and employing co-catalysts. Modification by doping is known to enhance the career concentration and improve the absorption by shifting band edges. Theoretical calculations indicate that Ni^{2+} incorporated in α-Fe_2O_3(0001) surface stabilizes surface-bound OH^- as compared to that on pure α-Fe_2O_3(0001) surface, thus enhancing the photoactivity of hematite.[3] Similarly, Mn^{2+} ion doping in hematite has been predicted to enhance the water splitting activity by creating more local low-barrier pathways. Mn^{2+}-O also has a value of bond length comparable to Fe^{3+}-O, thus creating low defects in the doped film.[4] Adhering oxygen evolution catalysts, such as FeOOH, NiOOH and Co-phosphate (Co-Pi), are known to improve water splitting activity by providing an alternative low energy pathway for charge transfer. Such experiments are in progress in our group.

The DLI-CVD method can be used for growth of thin conformal coating of oxides on different morphology substrates, such as vertically aligned nanowires, to overcome the drawback the poor electron transport. For e.g, a thin coating of BVO on vertically aligned TiO_2 nanowires on FTO substrates can likely help overcome the poor electron transport of BVO.[5] Similarly to increase surface area, hierarchically porous materials can be used as templates to synthesize high quality porous materials with high surface area.

The CVD process, as mentioned earlier is an industrially scalable process and hence can produce large area films. On a laboratory scale, photoactivities of an electrode are recorded by an irradiating a small working area of (< 1 cm^2).The effect of working area on the photocatalytic efficiency in the oxide films are yet to be explored. Effect of increasing working area will provide insight on the charge transport efficiency of the films and help in designing efficient electrode structures for practical devices.[6]

We have explored the water splitting photoactivity on Fe_2O_3 surface. Hematite is also a well-known catalyst for the I_2/I_3^- redox reaction with an activity similar to that of Pt metal.[7] CVD grown high quality materials are to be tested for such redox reactions. The high quality surface of these films can be investigated as a regeneration catalyst for other similar redox reactions.

6.4 References

(1) Archana, P. S.; Pachauri, N.; Shan, Z.; Pan, S.; Gupta, A. Plasmonic Enhancement of Photoactivity by Gold Nanoparticles Embedded in Hematite Films. *J. Phys. Chem. C* **2015**, *119*, 15506-15516.

(2) Sivula, K.; Le Formal, F.; Grätzel, M. Solar Water Splitting: Progress using Hematite (α-Fe_2O_3) Photoelectrodes. *ChemSusChem* **2011**, *4*, 432-449.

(3) Zhao, P.; Koel, B. E. Water Oxidation Catalysis: Effects of Nickel Incorporation on the Structural and Chemical Properties of the α-Fe_2O_3(0001) Surface. *ACS Appl. Mater. Interfaces* **2014**, *6*, 22289-22296.

(4) Liao, P.; Carter, E. A. Hole Transport in Pure and Doped Hematite. *J. Appl. Phys.* **2012**, *112*.

(5) Resasco, J.; Zhang, H.; Kornienko, N.; Becknell, N.; Lee, H.; Guo, J.; Briseno, A. L.; Yang, P. $TiO_2/BiVO_4$ Nanowire Heterostructure Photoanodes Based on Type II Band Alignment. *ACS Cent. Sci.* **2016**, *2*, 80-88.

(6) Fakharuddin, A.; Archana, P. S.; Kalidin, Z.; Yusoff, M. M.; Jose, R. Standardization of Photoelectrode Area of Dye-Sensitized Solar Cells. *RSC Adv.* **2013**, *3*, 2683-2689.

(7) Hou, Y.; Wang, D.; Yang, X. H.; Fang, W. Q.; Zhang, B.; Wang, H. F.; Lu, G. Z.; Hu, P.; Zhao, H. J.; Yang, H. G. Rational Screening Low-Cost Counter Electrodes for Dye-Sensitized Solar Cells. *Nat. Commun.* **2013**, *4*, 1-8.